Induction heating for catalytic dehydrogenation of liquid organic hydrogen carriers

DA Ford

orcid.org/ 0009-0009-9444-7850

Dissertation accepted in fulfilment of the requirements for the degree *Master of Science in Chemical Engineering* at the North-West University

Supervisor:	Dr PM Modisha
Co-supervisor:	Prof HM Krieg
Co-supervisor:	Prof DG Bessarabov

Graduation: October 2025

Declaration

I, Danae Ford, declare that the dissertation entitled 'Inductive Heating for the Catalytic Dehydrogenation of Liquid Organic Hydrogen Carriers' submitted in fulfilment of the requirements of the degree, Master of Science in Engineering Sciences with Chemical Engineering, is my own work, which has not been submitted to any other institution. All sources used in this study have been acknowledged and referenced accordingly.

Acknowledgements

I would like to begin by expressing my sincerest gratitude to Prof. Phillimon Modisha, without whom I would not have been here now—presenting my MSc dissertation. No words will suffice to thank you enough. You have been incredibly patient with me—with every setback, every delay, and every crisis. You remained supportive and patient for more than two and a half years. You led me along this academic journey, and never once gave up—even when I myself wanted to give up. I realise it could not have been easy, and there were times when it would have been frustrating, even exhausting. But you continued to show up, always assisting, always offering advice, and supporting me when I needed it most. I will never forget your generosity, your continuous kindness, and your faith in me, even when I could not even see the light at the end of the tunnel myself. Truly–thank you.

I would also like to thank Prof. Dmitri Bessarabov. I am grateful for the privilege of having been part of such a wonderful organisation as HySA Infrastructure. Your support not only gave me the opportunity to complete this study but also gave me a real glimpse into the practical applications of everything that I have studied over the years. Being part of this environment has helped shape my thinking and opened the door to the career that I am now pursuing.

To family and friends, thanks for bearing with me through this Master's degree journey, despite knowing it would be accompanied with endless rants over my research (and litres of Red Bull). You have served as my support system, my therapists (whether you signed up for it or not) and my greatest cheerleaders when I questioned all my life choices. I appreciate you all.

Lastly, I would like to express my gratitude to Prof. Henning Krieg. Not only did you bridge the gap between my Honours and Master degrees, but you were the one who initiated this further academic journey. Without your advice and recommendation to HySA, I would probably still be wandering aimlessly, lost in the world of "what's next". Thank you for setting me on this path.

I would also like to acknowledge that this research was conducted as part of Work Package 2 of the UnLOHCked Consortium, supported by funding from the Clean Hydrogen Partnership, Belgium, under Grant Agreement No. 10111196.

Publications

Publications related to this study:

D. Ford, G. Kruger, R. Garidzirai, P. Modisha, H. Krieg, and D. Bessarabov, "Feasibility of inductive heating for the dehydrogenation of liquid organic hydrogen carriers," International Journal of Hydrogen Energy, vol. 77, pp. 520-525, 2024.

Abstract

Hydrogen storage using liquid organic hydrogen carriers (LOHCs) is a promising solution due to their high hydrogen storage density, safe handling under ambient conditions and compatibility with existing crude oil infrastructure. However, large-scale implementation is limited by the high energy demands and uneven temperature profiles of the endothermic dehydrogenation reaction. Current heating approaches—electrical heaters and hydrogen burners—suffer from heat losses, reducing the overall energy efficiency. Electromagnetic inductive heating offers a compelling alternative; it delivers rapid, volumetric heating by generating heat directly within inductively active materials and transferring it efficiently to the catalyst and surrounding fluid.

This study explores inductive heating for LOHC dehydrogenation using perhydro-benzyltoluene (H12-BT) as a model compound and Pt/γ-Al_2O_3 catalysts synthesised via wet impregnation (0.3–8 wt.% Pt). Catalyst loading was confirmed using Inductively coupled plasma–optical emission spectroscopy (ICP-OES), and characterisation was performed using Brunauer–Emmett–Teller (BET), Carbon monoxide (CO) pulse chemisorption, scanning electron microscopy coupled with energy dispersive X-ray spectroscopy (SEM-EDS), Transmission electron microscopy (TEM), X-ray powder diffraction (XRD) and Hydrogen temperature programmed reduction (H_2-TPR). Four catalyst configurations were tested in an inductively heated reactor: (1) uncoated stainless steel (SS) pellets, (2) a mixture of SS and Pt/γ-Al_2O_3 pellets, (3) Pt/γ-Al_2O_3 coated SS pellets, and (4) a mixture of catalyst pellets and SS. The Pt/γ-Al_2O_3 coated SS pellets with 0.11 mol% Pt gave the highest performance: 0.35 $gH_2/gPt/min$ productivity and 97.82% H12-BT conversion.

Inductive and conventional electrical heating were compared using 5 wt.% Pt/Al_2O_3 coated SS pellets. Although electrical heating reached a higher maximum hydrogen flow rate (62.56 mL/min) and cumulative H_2 volume (2.03 L), inductive heating delivered a more stable profile (max flow rate: 27.78 mL/min, 1.65 L cumulative H_2), showing better thermal regulation. Among the catalyst loadings, 5 wt.% Pt gave optimal performance. Higher loadings (8 wt.%) led to decreased metal dispersion, larger particle sizes and pore blockage due to agglomeration. The influences of polymer binders, Polyvinyl alcohol (PVA) and

Polyvinylpyrrolidone (PVP), and coating thickness on catalyst performance were also assessed. Binder molecular weight and concentration influenced coating uniformity, adhesion, and diffusion. PVP (MW 55,000) at 0.5 wt.% offered the best results (0.26 $gH_2/gPt/min$ productivity, 65.39% conversion, 1.64 L H_2).

Coating thickness effects were explored using eggshell Pt/γ-Al_2O_3 coatings on SS pellets. A thickness of 81 µm (5 wt.% Pt) maximised H_2 yield and minimised by-products, outperforming both the thinner (62 µm) and thicker (>100 µm) coatings. Gas chromatography–mass spectrometry (GC-MS) confirmed the dehydrogenation pathway via partially hydrogenated BT (H6-BT) to benzyltoluene (HBT). Using GC-MS with single quadrupole detection (GC-SQ-MS) and advanced gas analysis, no by-products were detected at conversions >90%. Catalyst stability over four cycles showed signs of deactivation: productivity declined from 0.302 to 0.120 $gH_2/gPt/min$ and Degree of dehydrogenation (DOD) from 27% to 3%. Despite this, by-product formation declined, indicating reduced catalytic activity-limited side reactions. Kinetic analysis showed that the 82 µm coating gave the highest reaction rate constant and turnover frequency value (28.12 min^{-1}), suggesting an optimal balance between surface area and mass transfer.

Thorough characterization confirmed the synthesis and dehydrogenation efficacy of Pt/γ-Al_2O_3. Results from ICP-OES revealed that Pt loadings exceeded the intended levels, ranging from +1.67% to +17%. This suggests a minor overloading that could enhance the active sites, while also posing a risk for particle agglomeration, potentially affecting catalyst performance. SEM-EDS showed a transition from well-dispersed nanoparticles (NP's) at 0.3 wt.% Pt to aggregated clusters at 8 wt.%. BET analysis indicated a reduction in surface area from 186.8 m^2/g to 169.3 m^2/g, while TEM demonstrated NP growth from 1.11nm to 4.53 nm pre-reaction, increasing to 2.69nm and 6.91 nm post-reaction. XRD revealed sharper Pt peaks and enhanced crystallinity with increasing loadings, and CO pulse chemisorption indicated a decline in dispersion from 65.64% to 35.34%. Post-reaction HR-TEM indicated a contraction in d-spacing from 0.23 to 0.20 nm. TGA exhibited initial weight loss at ~200 °C (moisture removal) and primary decomposition between 300–450 °C, with PVP (MW 55,000) showing the most significant mass loss, while higher molecular weight binders exhibited slower degradation, suggesting enhanced thermal stability.

These results demonstrate that inductive heating, combined with optimised Pt/γ-Al_2O_3 coatings, offers a controlled, efficient, and scalable method for H12-BT dehydrogenation—outperforming conventional approaches.

Keywords: Inductive heating, catalytic dehydrogenation, hydrogen production, catalyst coating, H12-BT

Table of Contents

List of Figures

List of Tables

List of Abbreviations

^{1}H NMR	Nuclear proton magnetic resonance
ATM	Standard atmosphere (101.325 pascals)
BET	Brunauer–Emmett–Teller
BT	Benzyltoluene
CAPRI	*in situ* catalytic upgrading process
CHP	Combined heat and power system
CO	Carbon monoxide
CSP	Concentrated solar power
DBT	Dibenzyltoluene
D_m	metal dispersion
DOD	Degree of dehydrogenation
DOH	Degree of hydrogenation
DPM	diphenylmethane
E_a	activation energy
EGA	Evolved Gas analysis
FC	Fuel cell
fcc	face-centred-cubic
GC	Gas chromatography
GC-MS	Gas chromatography–mass spectrometry
GC-MS-SQ	GC-MS with single quadrupole detection
H12-BT	Perhydro-benzyltoluene
H12-DBT	Partially hydrogenated dibenzyltoluene
H12-NEC	perhydro-N-ethylcarbazole
H18-DBT	Perhydro-dibenzyltoluene
H_2-TPR	Hydrogen temperature programmed reduction
H6-BT	Partially hydrogenated benzyltoluene
HR-TEM	High-resolution transmission electron microscopy
HySA	Hydrogen South Africa
ICDD	International Centre for Diffraction Data
ICP - OES	Inductively coupled plasma–optical emission spectroscopy

k	Rate constant
LH_2	Liquefied hydrogen
LOHC	Liquid organic hydrogen carrier
m	Mean particle size
MCH	methylcyclohexane
NEC	N-ethylcarbazole
NP	Nanoparticle
$n_{Pt}/n_{H12\text{-}BT}$	Molar ratio of platinum (Pt) to H12-benzyltoluene (H12-BT)
P	Average power
PEM	Proton exchange membrane
PEMFC	Proton exchange membrane fuel cell
PGMs	platinum group metals
PtO_2	platinum oxide
PVA	Polyvinyl alcohol
PVP	Polyvinylpyrrolidone
r	Initial rate of reaction
RI	Refractive index
S_{BET}	Specific surface area
SEM	Scanning electron microscopy
SEM-EDS	Scanning electron microscopy coupled with energy dispersive X-ray spectroscopy
SOFC	Solid oxide fuel cell
STP	Standard temperature and pressure (0 °C, 1 atm)
TCD	Thermal conductivity detector
TEM	Transmission electron microscopy
TGA	Thermogravimetric analysis
THAI	toe-to-heel air injection
TOF	Turnover frequency
VH12-BT	Volume H12-benzyltoluene
$X_{H12\text{-}BT}$	Selectivity for H12-BT
$X_{H6\text{-}BT}$	Selectivity for H6-BT

XRD	X-ray powder diffraction
μ	log-normal mean standard deviation

1. CHAPTER 1: INTRODUCTION

1.1 Background

Global climate change is becoming an increasing concern as greenhouse gas emissions rise, fossil fuel reserves become depleted and the demand for power increases (Asiaban *et al.*, 2021). Renewable energy sources are gaining increasing attention for minimising greenhouse gas emissions and combating climate change (Granovskii *et al.*, 2007). The main renewable energy sources, namely wind and solar, are intermittent by nature, leading to inconsistent power supply (Asiaban *et al.*, 2021). Consequently, a viable energy storage system is required to mitigate the power fluctuations (Asiaban *et al.*, 2021). In the pursuit of establishing a sustainable and green energy system, hydrogen presents as a promising clean energy carrier with applications in various Fuel Cell (FC) technologies—from stationary power generation to mobile uses such as in transportation—aligning with global efforts to contribute to the reduction of greenhouse gas emissions (Hassan *et al.*, 2024).

Hydrogen produced using renewable and sustainable sources plays a pivotal role in enabling the decarbonisation of various industries—this includes hard-to-abate sectors that include, but are not limited to, manufacturing, power generation and mobility (Franco & Rocca, 2024). The mobility sector includes hydrogen-powered vehicles or mining trucks (Roy & Pramanik, 2024; Staffell *et al.*, 2019). Hydrogen is used as a reducing agent in steel production as a replacement for carbon-intensive coal (Roy & Pramanik, 2024). Hydrogen FCs allow rapid power generation for backup and grid scale (Hwang *et al.*, 2023). Hydrogen can also be used in ammonia synthesis in the petrochemical industry (e.g., hydrotreating and hydrocracking processes for refining) (Reddy *et al.*, 2023).

Although hydrogen is considered a promising alternative to fossil fuels, significant challenges that hinder its wider adoption include the efficiency, and costs associated with its storage and distribution (Hassan *et al.*, 2023). Conventional hydrogen storage methods, such as compressed gas storage and liquefaction, face challenges related to safety concerns, boil-off losses, storage capacity limitations, logistical inefficiencies and high costs (Aakko-Saksa *et al.*, 2018). Compressed hydrogen requires costly high-pressure storage tanks, while liquefied hydrogen must be kept at –273 °C, which presents logistical inefficiencies (Dauletbay, 2024). The low volumetric energy density of hydrogen poses a challenge to the storage of large quantities, as is required to achieve a significant amount of energy (Tashie-Lewis & Nnabuife, 2021). Therefore, addressing this issue is essential to advance the deployment of hydrogen-based technologies.

Liquid organic hydrogen carriers (LOHCs) have the potential to serve as a medium for the large-scale storage and the distribution of green hydrogen. Unlike traditional storage technologies, LOHC molecules, specifically those based on benzyltoluene (BT), offer numerous advantages: zero self-discharge, non-flammability, reversible storage and distribution, cost-effectiveness and a considerable hydrogen storage density (6.2 wt.%: 56 kg-H_2/m^3-LOHC) (Lin & Bagnato, 2024; Modisha & Bessarabov, 2023; Preuster, Papp*, et al.*, 2017). LOHC systems enable only hydrogen to be charged or discharged during the dehydrogenation reaction, while the carrier molecule remains recyclable (Rao & Yoon, 2020). Notably, the LOHC H18-DBT) has diesel-like properties, a low melting point and high boiling point, non-flammability and, furthermore, is compatible with existing fuel infrastructure (Lin & Bagnato, 2024; Müller *et al.*, 2016). However, drawbacks include the high viscosity at low temperatures, leading to potential pumping issues (Aakko-Saksa *et al.*, 2018; Hassan *et al.*, 2023). An alternative LOHC, BT exhibits chemical characteristics to those of DBT but with lower viscosity, thus facilitating the easier handling of the carrier at lower temperatures (Dauletbay, 2024).

One of the challenges associated with the dehydrogenation of LOHCs is efficient heat transfer, which is required to facilitate the reaction. Research by Rüde *et al.* demonstrated the feasibility of multiple hydrogen charging and discharging cycles with no signs of degradation of catalyst or LOHC molecules under mild conditions (commercial 0.3 wt.% Pt/Al_2O_3, 290 °C, 30 bar for hydrogenation and 1–1.6 bar for dehydrogenation) (Rüde *et al.*, 2022).

Conventional heating methods for the dehydrogenation reaction, such as electrical heating, while convenient, do have disadvantages, such as slow heating and cooling rates, non-uniform temperature distribution and low energy efficiency (Wang *et al.*, 2019). When using electrical heating methods, approximately 20% of the total energy required for dehydrogenation is lost to preheating and heat loss to the surroundings, resulting in a low energy efficiency (Müller *et al.*, 2019). In contrast, electromagnetic inductive heating presents a more efficient alternative—it offers direct and targeted heat delivery, faster heating and cooling rates, and increased energy efficiency (Lin & Bagnato, 2024). Inductive heating, using radio frequency inductive, minimises heat loss to the environment; thus, consistent reaction temperatures are maintained. This method demonstrates superior efficiency compared to conventional heating methods as it directly transfers heat to the catalyst pellets and surrounding fluid, eliminating temperature gradients (Schörner *et al.*, 2024). Through improved heat distribution, lower energy consumption and faster charge/discharge cycles, inductive heating has the potential to improve the practicality and efficiency of LOHC systems.

Despite the challenges that electrical heating presents, it currently remains the dominant source of heat in the dehydrogenation of LOHCs because it is convenient (Wang *et al.*, 2019). To date,

most of the heat supplied to the endothermic reaction originates from electrical heating mantles and jacketed heat transfer fluids (Fikrt *et al.*, 2017; Modisha*, et al.*, 2019; Preuster*, et al.*, 2017). Use of alternate heat sources, such as gas burners, waste heat from the hydrogenation reaction, FCs, gas turbines, and other industries, have been reported in the literature (Bollmann, Schmidt*, et al.*, 2023; Dennis *et al.*, 2021; Fikrt *et al.*, 2017; Haupt & Müller, 2017; Jorschick *et al.*, 2017; Krieger *et al.*, 2016b; Preuster *et al.*, 2018). A bio-methane gas burner with porous media provided a uniform temperature distribution and resulted in high productivity in the dehydrogenation of H18-DBT (Bollmann, Mitländer*, et al.*, 2023). When waste heat is used, the efficiency of the LOHC system is improved. For example, Krieger *et al.* supplied the H18-DBT LOHC system with waste heat from a cement plant coupled with a wind park (Krieger *et al.*, 2016a). This LOHC system provided 76% of the electricity demand—saving on electricity costs—and offered increased efficiency (16%–28.5%). Further examples of LOHC/heat sources are given in Table 1.1, along with an efficiency comparison of existing integrations of the LOHC system H18-DBT.

Table 1.1 compares the efficiency of several systems that integrate H18-DBT, along with their applications. A proton exchange membrane fuel cell (PEMFC) is able to operate with hydrogen release from the dehydrogenation of H18-DBT (4.5 h, 6.6 kW) (Geiling *et al.,* 2021). Preuster *et al.* established the feasibility of solid oxide fuel cell (SOFC) operation on LOHC-based hydrogen to create an efficient model for heat integration between the endothermic dehydrogenation stage and the exothermic FC operation (Preuster *et al.,* 2018). Thermic fluid heating or direct heating of the dehydrogenation reactor using a concentrated solar power (CSP) plant eliminates the need for additional hydrogen production and reduces the inventory of LOHC required for specific applications (Rao *et al.,* 2023). Integration of combined heat and power (CHP) used in residential buildings with LOHC systems reduces primary energy demand by 16% and improves the self-sufficiency and self-consumption rate (Haupt & Müller, 2017). A steady-state model has been developed to demonstrate the adaptability of a H_2-fired gas turbine (7.7 MW) and H18-DBT LOHC system for seasonal and short-term energy production and demand variations (Dennis et al., 2021).

Table 1.1 Existing integrations of the H18-DBT LOHC system and their efficiencies.

System integration	Application	Efficiency, %
LOHC/PEMFC	Transportation	36–43.8 (Fikrt *et al.*, 2017; Sievi *et al.*, 2019)
LOHC/SOFC	Grid-independent power supply	45 (Preuster *et al.*, 2018)
LOHC/CSP	Solar-driven heating	23,1 (Krieger *et al.*, 2016b)
LOHC/CHP	Thermal energy supply in residential buildings	30 (Haupt & Müller, 2017)
LOHC/H_2 gas-fired turbine	Grid stability	22 (Dennis *et al.*, 2021)

However, inductive heating has not yet been fully explored. Hart *et al.* compared the effects of conventional heating and inductive heating of the dehydrogenation of tetralin (Hart *et al.*, 2020a), using steel pellets as a substrate. They established that inductive heating improved the activity because of the effective heat transfer offered by the SS pellets (catalyst) to the bulk fluid. However, when electrical heating was applied, the heat transfer process from the source to the catalyst was compromised.

In contrast, electromagnetic inductive heating presents a more efficient direct and targeted heat delivery, faster heating and cooling rates, and increased energy efficiency (Kuhwald *et al.*, 2022; Wang *et al.*, 2019). Inductive heating, using radio frequency inductive, minimises heat loss to the environment, thus consistent reaction temperatures are maintained (Wang et al., 2019).

1.2 Research Motivation

The motivation for this study is based on the increasing requirement for sustainable hydrogen storage technologies and the goal of maximising the benefits of LOHC technology in addressing global energy challenges. LOHCs, particularly BT based systems, have shown promise in large-scale storage and the distribution of green hydrogen. The research is driven by the goal of advancing our understanding of LOHCs, with specific focus on BT as an efficient carrier for hydrogen storage. LOHCs exhibit favourable characteristics, including relatively low operating temperatures for hydrogen release, good thermal stability, and high volumetric hydrogen capacity. The utilisation of electromagnetic inductive heating

addresses limitations associated with conventional heating methods for endothermic dehydrogenation reactions of LOHCs—it may offer faster heating rates, while directing the heat from the core of the inductively active materials to the catalyst and the surrounding fluid. Current challenges in Pt catalysts supported on γ-Al_2O_3 such as metal particle agglomeration and limited metal dispersion negatively impacts catalytic activity and stability. These catalyst-related limitations hinder the efficiency and durability of the dehydrogenation process, highlighting the need to better understand and optimise Pt loading on γ-Al_2O_3 to enhance overall LOHC performance.

1.3 Methodology

This study describes an investigation into the effect of inductive heating in a catalyst system, utilising Pt/γ-Al_2O_3 catalysts coated on SS pellets, for the dehydrogenation of H12-BT, for efficient heat transfer and distribution. The endothermic dehydrogenation of H12-BT has a high heat demand, which requires efficient heat transfer methods. Electromagnetic inductive heating allows heat to flow from the SS pellets directly to the catalyst and then the surrounding fluid, whereas conventional electrical heating heats the liquid and then the catalyst (Hart et al., 2020). Inductive heating allows for faster heating rates and more uniform heating, while also minimising heat loss to the surroundings (Hart *et al.*, 2020a).

The use of SS pellets as an eggshell catalyst allows high heat generation as a result of their high electrical conductivity in inductive heating (Wang *et al*., 2019). Another advantage of SS pellets is the uniform distribution of heat (Idakiev *et al.*, 2015). An inductive -heated batch reactor will be used to evaluate the catalyst performance for the dehydrogenation of H12-BT, under various reaction conditions.

The following techniques are useful here for characterisation of the catalysts in this study.

- Inductively coupled plasma–optical emission spectroscopy (ICP-OES) is used to confirm the metal loading.
- Brunauer–Emmett–Teller (BET) analysis is used to measure the catalyst surface area, pore volume and diameter.
- Carbon monoxide (CO) pulse chemisorption and temperature programmed reduction (H_2-TPR) provide information on metal dispersion, surface area, particle size and reduction behaviours of metal oxides.
- Scanning electron microscopy coupled with energy dispersive X-ray spectroscopy (SEM-EDS) is used

to analyse the morphology and composition of the synthesised catalysts.

- High-resolution transmission electron microscopy (HR-TEM) is used to evaluate the nanoparticle (NP) size distribution.
- X-ray diffraction (XRD) is used to observe/determine the phase composition and crystalline structure of the catalysts.
- Thermogravimetric analysis TGA) is used to evaluate the catalyst composition and thermal stability by tracking weight changes as a function of temperature.
- Gas chromatography–mass spectrometry (GC-MS) is useful in validating the dehydrogenation reaction and monitoring any changes in the liquid carrier molecules.

Utilisation of all these practical analytical/characterisation methods is valuable in ensuring that the catalysts are suitably synthesised and validated—with their properties then later correlated to their performances in the dehydrogenation of H12-BT.

1.4 Research Problem

High energy demand and uneven temperature distribution due to the endothermic nature of the H12-BT dehydrogenation reaction is a major drawback. Currently, for convenience, electrical heating and the use of porous hydrogen burners are the standard heating methods employed in dehydrogenation reactions. However, during the dehydrogenation reaction, they lead to heat loss and a reduction in energy efficiency—to 24% and 34%, respectively. Furthermore, slow heating limits end-user applications that require fast hydrogen release.

Electromagnetic inductive heating is an efficient method that is able to target the heat concern—it is expected to improve the heat transfer. Inductive heating offers faster heating and cooling rates because the heat flows directly from the SS pellets within a reactor to the catalyst pellets and surrounding fluid, allowing for uniform heating. While heat loss and reduced energy efficiency due to conventional heating methods are well-documented challenges in LOHC dehydrogenation, a critical problem remains in catalyst performance, where reported materials—including Pt supported on γ-Al_2O_3—often suffer from metal particle agglomeration and limited metal dispersion, limiting catalytic activity and stability and thus hindering efficient hydrogen release.

In view of the gaps in knowledge identified, this study will investigate the effect of inductive versus electrical heating on catalytic activity in the dehydrogenation of H12-BT, for the recovery of hydrogen.

1.5 Aim and Objectives

The overall aim of this study is to determine the feasibility of utilising inductive heating for the dehydrogenation of H12-BT using Pt/γ-Al_2O_3 coated SS pellets as inductively active catalyst material.

To achieve this aim, the following specific objectives/tasks were envisaged.

1. Synthesise Pt/γ-Al_2O_3 catalysts with different metal loadings (0.3 wt.%, 1 wt.%, 3 wt.%, 5 wt.% and 8 Pt wt.%), using the wet impregnation method.
2. Prepare inductively active catalyst materials of varying shell thickness of Pt/γ-Al_2O_3 on SS pellets, using a dip coating method, and also determine the effect of added polymer binders
3. Conduct the dehydrogenation of H12-BT using a batch reactor system, then evaluate the catalyst performance in terms of productivity, selectivity, and conversion.
4. Investigate the effect of catalyst shell thickness on mass transfer limitations during the dehydrogenation of H12-BT.
5. Determine the catalyst activity for the release of hydrogen from LOHCs, utilising various characterisation techniques, e.g., ICP, TPR, CO pulse chemisorption, H_2-TPR, SEM-EDS, BET, TEM, XRD and TGA.
6. Examine dehydrogenation of H12-BT performance while comparing electrical heating and inductive heating

1.6 Significance of the Study

The significance of this study lies in addressing current inefficiencies relating to heating methods employed for the catalytic dehydrogenation of H12-BT. This research explores the use of electromagnetic inductive heating as a scalable solution for the safe and efficient release of hydrogen. The advantages of inductive heating—faster heating and cooling rates, and a targeted heat delivery—reduces energy consumption (compared to conventional heating methods). Faster heating rates unlock the use of LOHC technology for applications where immediate hydrogen release is required, including power generation on demand using FCs, for rapid refuelling and chemical processing (ammonia production).

The results of this study should also promote the beneficiation of platinum group metals (PGMs), used here as catalysts, in addition to increasing efficiency. More local use of PGMs is being actively encouraged by South Africa, which possesses about 80% of the worlds PGM reserves.

Overall, this research aligns with the goals of the EU's unLOCHked project as well Hydrogen South Africa (HySA)—optimising energy usage in hydrogen production—whilst also specifically demonstrating the feasibility of inductive heating.

1.7 Layout of Document

This document is divided into five chapters, with a final reference list. Catalytic dehydrogenation using H12-BT and the feasibility of inductive heating are investigated and discussed in the following chapters.

Chapter 1: Introduction

This chapter provides a background to LOHC technology, with emphasis on H12-BT. as a hydrogen carrier, and highlights important research issues such as the requirement for effective dehydrogenation processes and the role that heating methods play in eventual catalyst performance. Following on from this background, existing gaps in current knowledge are identified and a problem statement is presented. This is followed by the research motivation for and the significance of this study. The overall aim and specific objectives/tasks are outlined.

Chapter 2: Literature Review

The literature review includes only peer-reviewed journals as sources, with emphasis of the literature study on popular catalysts and their functionality. The viability of BT as an LOHC system is specifically highlighted, and its dehydrogenation efficiency is assessed under various heating circumstances. The effect of inductive and conventional heating on the dehydrogenation reaction and on catalytic activity is addressed. Gaps in the literature are noted, with particularly reference to the optimisation of inductive heating for LOHC dehydrogenation. The (favourable) role of the inclusion of SS pellets in LOHC catalysts (Pt/γ-Al_2O_3-based catalysts), in terms of enhancing heat distribution and catalytic performance during inductive heating, is explored.

Chapter 3: Materials and Methods

Experimental details pertaining to the materials used and methods/procedures followed are described. The methods used for determining catalyst performance under various heating conditions are described in the methodology. An experimental design for an inductive heating batch reactor is included. This reactor was used to evaluate how inductive heating influences BT dehydrogenation. The efficiency of dehydrogenation under inductive and conventional heating modes was compared

through experiments that assess the stability of the catalyst, energy consumption and the hydrogen release rates. To determine structural and thermal properties of the synthesised catalysts, the experimental procedures followed involved catalyst synthesis, and characterisation using analytical methods such as ICP, TPR, CO pulse chemisorption, H_2-TPR, SEM-EDS, BET, TEM, XRD and TGA.

Chapter 4: Results and Discussion

Experimental results and results of analyses, as pertaining to catalyst performance, heating efficiency and hydrogen evolution are presented. Various catalyst configurations and heating modes were compared to determine the effect of inductive heating on the dehydrogenation efficiency. Results from the various characterisation methods offered insight into the structure stability and performance of catalysts. The coating thickness, temperature and catalyst loading were also examined. A comparison of results from conventional and inductive heating revealed variations in the stability and efficiency of energy consumption. The dehydrogenation process and hydrogen purity were verified by product analysis.

Chapter 5: Conclusion

In this final chapter, conclusions are drawn to the overall aim and the specific objectives of the study. Particular attention is paid to how the heating techniques improve the efficiency of dehydrogenation. Then, to address the research problem, a summary of the main findings is given to highlight how the heating method and catalyst design influence LOHC technology. This is followed by suggestions for further research, such as possible improvements in inductive heating and improved catalysts for better LOHC performance.

2. Chapter 2: Literature Review

This chapter discusses the available literature on conventional hydrogen storage methods and, specifically, explores the potential of LOHC as an emerging technology for hydrogen storage. Literature gaps are identified in the catalytic dehydrogenation reaction for the dehydrogenation of BT-based molecules, as are commonly used is LOHC systems. Different heating methods are explored for catalytic dehydrogenation, with focus on the comparison of inductive heating and conventional electrical heating methods. Key analytical techniques applicable to this study are discussed, highlighting their role in the assessment of the physiochemical properties of the catalyst as well as the analysis of the LOHC reaction mixtures.

2.1 Hydrogen Storage Methods

The two most common renewable energy sources, wind and solar energy, are sustainable alternatives to fossil fuels (Teichmann, Arlt*, et al.*, 2012). However, both have significant disadvantages to consider: e.g., solar energy relies on sunlight availability, making it intermittent and unreliable (Borges, 2012). In addition, large-scale solar power plants require substantial land areas for installation, complicating renewable energy infrastructure (Borges, 2012). Similarly, wind energy faces intermittency issues due to unpredictable wind speeds (Asiaban *et al.*, 2021), and a feasible energy storage system is needed to balance fluctuations (Geburtig *et al.*, 2016).

Hydrogen gas has emerged as a promising clean energy carrier for various FC applications due to its high energy density (120.0 MJ/kg) compared to commonly used fuels such as gasoline (Durbin & Malardier-Jugroot, 2013). Developing efficient and cost-effective storage methods is crucial to advancing renewable energy through the more widespread adoption of hydrogen FC and related technologies (Lin & Bagnato, 2024). Hydrogen offers a greenhouse gas emission-free option—positioning the 'hydrogen economy' as a viable alternative to carbon-based fuels (Lin & Bagnato, 2024).

To develop a hydrogen economy, cost effective infrastructure is required for hydrogen storage and delivery (Kim *et al.*, 2014). Hydrogen gas is both buoyant and small, making storage challenging. Extensive research is being carried out to develop a hydrogen storage technique that is compact, safe, cost-effective and energy efficient (Kim *et al.*, 2014). There are various hydrogen storage methods that have been investigated, each with their own volumetric and gravimetric hydrogen storage capacity, intrinsic advantages, and disadvantages. Hydrogen storage methods include physical storage, material- and chemical-based storage. Physical storage methods include the use of compressed

hydrogen, liquefied hydrogen, and cryo-compressed hydrogen, with the former method being the most commercially available technology. Material-based hydrogen storage includes the use of metal hydrides, complex hydrides and porous materials are compact solutions, however, offers major drawbacks. Material-based hydrogen storage methods such as the use of metal and complex hydrides, while offering high hydrogen densities, suffer from slow kinetics, high temperature and pressure, as well as material degradation over life cycles. Complex hydrides (7.4 wt.%) have the similar challenges: slow reaction rates and high costs (Langmi *et al.*, 2014). Chemical storage methods offer potential—through reversible or irreversible chemical reactions, to extract the hydrogen. Table 2.1 presents a comparison of hydrogen storage properties of various hydrogen storage methods.

Table 2.1 Comparison of hydrogen density, hydrogen energy density and hydrogen capacity for various hydrogen storage methods (Rivard *et al.*, 2019; Usman, 2022).

Hydrogen storage method	**Volumetric hydrogen density (g/L)**	**Volumetric energy density (MJ/L H_2)**	**Hydrogen capacity (wt.%)**	**Pressure (bar)**	**Remarks**
Compressed H_2 (Rivard *et al.*, 2019)	17.4–40.8	1.4–4.9	1–4.2	200–700	Current industry standard
Liquefied H_2 (Preuster, Alekseev*, et al.*, 2017)	51–70.79	6.4–8.5	7.5	12.8	Boil-off drawback
Cryo-compressed H_2 (Moradi & Groth, 2019)	50–80	4.0	10	50–700	Boil-off drawback
Metal hydrides (Langmi *et al.*, 2014)	90–110	13.2	7.6	1–100	Thermal management system needed
Complex hydrides (Langmi *et al.*, 2014) ($NaAlH_4$)	80	9.6	7.5	105	High pressure thermal management system needed
LOHCs (Gianotti *et al.*, 2018), (Niermann *et al.*, 2019)	47–62	7.0	4.4–7.3	Standard atmosphere (atm)	Highly endo/exothermic process High energy demand Catalyst development required

Another major challenge facing the hydrogen economy is that gaseous hydrogen exhibits the lowest energy density per unit volume (0.0108 MJ/L). Furthermore, it poses a substantial risk of violent explosions upon contact with air (Durbin & Malardier-Jugroot, 2013). Considering the limited capacity for fuel storage within a vehicle and the necessity for reinforced fuel tanks to avert explosion hazards in the event of a collision, there arises a pressing need for an efficient, secure, cost-effective and compact solution for hydrogen storage (Durbin & Malardier-Jugroot, 2013).

2.1.1 Compressed hydrogen

Compressed hydrogen is the current industry standard, boasting its simplicity for the release of hydrogen (Usman, 2022). Compressed hydrogen is energy intensive in nature. However, due to the high pressure, large-volume tanks are required; further drawbacks include added weight and costs, and space utilisation (Züttel, 2004). Special coatings are required for compressed hydrogen containers to prevent diffusion and embrittlement (Lin & Bagnato, 2024). Elevated pressure levels associated with this method of storage increase the risk of explosion. Additionally, compressed hydrogen storage offers a relatively low storage capacity for hydrogen (1–4.2 wt.%, 200–700 bar, –40 to 65 °C) and low hydrogen density (0.083 kg/m^3), thereby constraining its overall efficiency (Lin & Bagnato, 2024), (Andersson & Grönkvist, 2019).

2.1.2 Liquefied hydrogen

Liquefied hydrogen, offering hydrogen density higher than that of compressed hydrogen and resulting in an increased volumetric energy density, also exhibits high rates of hydrogen release. Liquefied hydrogen is able to be implemented in large-scale storage. However, the storage of liquefied hydrogen requires extremely low temperatures (7.5 wt.%, 12.8 bar, –253 °C) as the boiling point of hydrogen is –240 °C at ambient pressure (Rivard *et al.*, 2019). Further drawbacks of using liquefied hydrogen are the associated high storage costs at such low temperatures and the liquefaction process is energy intensive (Barthélémy *et al.*, 2017). The boil-off phenomenon hinders its widespread adoption as there is a loss of hydrogen due to energy input from the surroundings that vaporises 1.5%–3% per day (Schlapbach & Züttel, 2001), (Zhang *et al.*, 2016). Thus, excessive and expensive insulation is required to prevent boil-off. Liquefied hydrogen is also unsuitable for mobility applications due to the extreme storage conditions and the boil-off losses (Usman, 2022). As a result, liquefied hydrogen is not economical, especially for long-term storage and long-distance transport.

2.1.3 Cryo-compressed hydrogen

Cryo-compressed hydrogen (10 wt.%, 50–70 bar, –253 to 163 °C) is the one of the most widespread hydrogen storage methods. It involves the use of liquid hydrogen under pressure, compressed

hydrogen gas that has been cooled, and systems wherein liquid hydrogen and its vapour coexist in a two-phase state (Durbin & Malardier-Jugroot, 2013). From an efficiency perspective, cryo-compression can be seen as more advantageous than relying solely on liquid storage because it helps to minimise the issue of boil-off (Rivard *et al.*, 2019). Nevertheless, boil-off remains a significant drawback, largely restricting the implementation of this hydrogen storage method. Cryo-compressed hydrogen at optimal conditions of 350 bar at –253 °C is, nonetheless, a suitable hydrogen storage method because it offers higher hydrogen densities and reduced boil-off losses compared to liquefied hydrogen (Usman, 2022). However, double-walled vessels must be used at extremely low temperatures for storage and an increased energy input is required, thus making this a more expensive storage method (Abdalla *et al.*, 2018). A high pressure is also required for hydrogen storage, and there is a high demand for cooling energy and cooling equipment to prevent the hydrogen from vaporising (Barthélémy *et al.*, 2017).

2.1.4 Metal hydrides

The use of metal hydrides is another well-studied hydrogen storage method that offers a high hydrogen storage capacity (7.7 wt.%) (Usman, 2022). Metal hydrides have the ability to absorb and release hydrogen reversibly, allowing controlled storage and release of hydrogen as required (Barthélémy *et al.*, 2017). The storage of hydrogen is stable at ambient conditions, which simplifies the storage and handling (Zhang *et al.*, 2016). A disadvantage of metal hydrides, however, is that they have low absorption and desorption kinetics, which limits the overall efficiency of such a system (Züttel, 2004). Several metal hydrides require high temperatures and pressures for desorption and absorption, which then increases the energy input requirements of the system (Adametz *et al.*, 2016). Hydrogen storage in metal hydrides has a limited life cycle because repeated absorption and desorption of hydrogen leads to degradation of the metal hydrides over time, thus affecting their long-term performance and economic viability (Sakintuna *et al.*, 2007). The more widespread adoption of metal hydrides as a commercial hydrogen storage method is typically hindered by the associated high costs and the availability (Rivard *et al.*, 2019). Overall, despite the fact that metal hydrides offer promising properties for hydrogen storage, based on their high capacity and inherent safety, issues with their slow kinetics, temperature/pressure requirements, constrained life cycle and costs need to be addressed prior to their wider practical implementation in various applications.

The use of complex hydrides is a well-studied storage method and for their potential in reversible hydrogen storage (Züttel, 2003). Among these materials, $NaAlH_4$ stands out as the most widely used complex hydride due to its ease of mass production and high hydrogen storage capacity of 7.4 wt.% (Usman, 2022). However, despite this impressive storage capacity, only 5.6 wt.% of hydrogen can be

released from $NaAlH_4$, highlighting its slow hydrogen release kinetics (Usman, 2022). Full dehydrogenation of $NaAlH_4$ cannot be achieved due to thermodynamic and kinetic limitations, and high temperatures and pressures are required. Consequently, slow desorption and absorption kinetics leads to extended charging and discharging times (Rivard *et al.*, 2019). Although complex metal hydrides are capable of storing hydrogen under ambient conditions without rapid decomposition, the repetitive process of absorption and desorption does lead to material degradation over multiple cycles (Srinivasan & Demirocak, 2017). The ongoing research aims to enhance the kinetics and stability of complex hydrides for more practical hydrogen storage applications.

Thus, to date, the challenge of storing and transporting hydrogen on a large scale has not yet been fully resolved. A promising approach for efficient long-distance transport and high-density hydrogen storage involves the use of LOHCs. Such LOHCs have emerged as highly favourable storage media for large-scale stationary hydrogen storage, primarily due to their advantageous characteristics, including cost effectiveness and compatibility with existing fuel transport infrastructure (Aakko-Saksa *et al.*, 2018). This compatibility reduces the need for extensive infrastructure modifications and simplifies the incorporation of LOHC-based hydrogen storage systems—effectively reducing greenhouse gas emissions (Southall & Lukashuk, 2022). The price of hydrogen generated from natural gas varies, based on the region: $0.9 p/kg, $2.2 p/g and $3.2 p/kg for the US, EU and Japan, respectively (Körner *et al.*, 2015). Wind and solar generated hydrogen retails for $7 to $11 p/kg and $10 to $30 p/kg (2015 figures) Large-scale hydrogen production from biomass gasification costs $1.5–$3.50 p/kg (Aakko-Saksa *et al.*, 2018)

2.1.5 LOHCs

LOHCs offer the long-term storage of excess renewable energy in the form of hydrogen, as there is no self-discharge (Lin & Bagnato, 2024). LOHCs have a higher hydrogen storage capacity than compressed hydrogen, coupled with a low safety risk (Chu *et al.*, 2023; Gianotti *et al.*, 2018; Rivard *et al.*, 2019).

Properties of the most suitable LOHC molecules should including the following: non-toxic, low melting point, high boiling point, high storage capacity (>56 kg/m^3, >6 wt.%), reversibility, high durability and low binding enthalpy (30–50 kJ/mol H_2) (Lin & Bagnato, 2024). LOHCs exhibit reduced flammability and toxicity compared to alternative hydrogen storage methods, thus significantly enhancing their safety profile during handling and transportation (Modisha & Bessarabov, 2020). Using LOHCs as an alternative storage system addresses barriers in the large-scale deployment of renewable energy as they efficiently store substantial hydrogen content over the long term without self-discharge (Modisha & Bessarabov, 2020). With high reversible hydrogen storage capacities, ranging between 1.7 and 7.3 wt.%, LOHCs maintain a liquid state under ambient conditions, ensuring ease of implementation for

storage and transport (Zhu & Xu, 2015).

In terms of energy density, LOHCs take advantage of the limitations of compressed or liquefied hydrogen storage techniques. This enables efficient storage and release of large quantities of hydrogen, facilitating compact storage systems that are practical. For long-term storage, LOHCs demonstrate remarkable stability, allowing extended storage periods without significant hydrogen loss (Modisha, Ouma*, et al.*, 2019). Their molecular durability supports multiple hydrogenation and dehydrogenation cycles, ensuring sustained performance over time (Modisha, Ouma*, et al.*, 2019). A key benefit here is that only hydrogen is consumed or released during reaction, allowing multiple charging and discharging cycles (Dornheim *et al.*, 2022). LOHCs offer inherent safety advantages by enabling the storage of hydrogen under ambient conditions, alleviating the risks associated with compressed or cryogenic storage (Andersson & Grönkvist, 2019). Another advantage is that LOHCs are both non-flammable and non-explosive, reinforcing their safety credentials.

Scalability is another key advantage of LOHC technology—it meets a wide range of storage requirements, from residential energy systems to expansive industrial installations (Teichmann, Stark*, et al.*, 2012). This scalability facilitates the widespread adoption of LOHC-based hydrogen storage across various sectors, contributing to broader energy transition goals.

However, key challenges associated with LOHCs remain—including the development of efficient catalysts, optimisation of reaction kinetics and a reduction of costs. Ongoing research is focused on enhancing catalyst stability, selectivity, and recyclability. Besides this, the exploration of new LOHC materials with improved performance is ongoing.

2.2 LOHC Systems

LOHC systems comprise a pair of liquid organic molecules—one hydrogen-lean compound and one hydrogen-rich compound—that reversibly convert via catalytic hydrogenation and dehydrogenation (Dürr *et al.*, 2021). Hydrogenation is an exothermic reaction that occurs at pressure >20 bar and temperature <150 °C, facilitated by a catalyst, most commonly Pt/γ-Al_2O_3 at this temperature.

After transportation and storage, the hydrogen is 'unloaded' from the LOHCs through catalytic dehydrogenation, allowing the stored energy to be recovered. Dehydrogenation is an endothermic reaction that occurs under low pressure (<5 bar) in a temperature range 270–350 °C. This process involves applying heat and using a dehydrogenation catalyst, which induces the reverse reaction, returning the LOHC to its original state while releasing high-purity hydrogen (Müller *et al.*, 2015). Figure 2.1 provides a schematic of the hydrogenation and dehydrogenation cycles for LOHC storage.

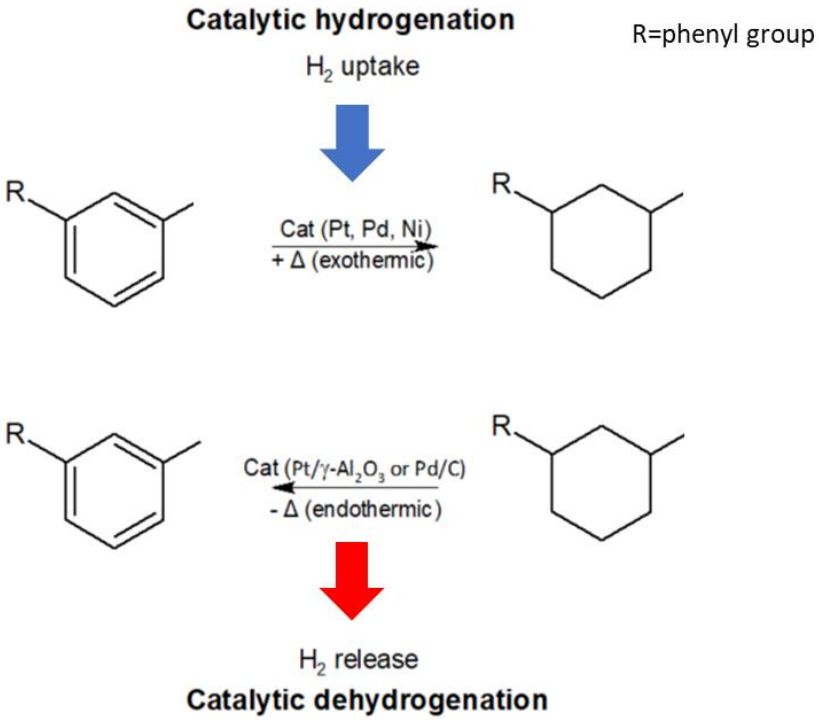

Figure 2.1. Schematic representation of hydrogenation/dehydrogenation of LOHC molecules (adapted from (Geißelbrecht *et al.*, 2020)).

The use of various LOHC systems has been suggested, each with varying hydrogen storage capacities, and advantages and disadvantages. Initially, benzene and its corresponding hydrogenated pair cyclohexane (hydrogen storage capacity 7.2%) was explored as a potential LOHC system (Chu et al., 2023). Although benzene/cyclohexane dehydrogenation can proceed under relatively mild conditions, the carcinogenic and volatile nature of benzene makes it undesirable for practical use (Markiewicz et al., 2015). Additionally, the practical implementation of cyclohexane as a LOHC encounters obstacles stemming from the requirement for elevated operational temperatures and the need for a stable catalyst capable of preventing coking during the dehydrogenation process (Abdalla et al., 2018).

Figure 2.2 shows the relationship between dehydrogenation enthalpy (kJ/mol) and the hydrogen storage capacity of common LOHC pairs. The red line shows that the ideal enthalpy range for hydrogenation/dehydrogenation is 40–70 kJ/mol H_2 (Harb *et al.*, 2023), (Von Wild *et al.*, 2010). This allows low-temperature conversion whilst keeping both H_2-rich and H_2-lean molecules liquid at STP (Preuster, Papp*, et al.*, 2017). The red lines show the constraints for the minimum H_2 content as well as the maximum dehydrogenation enthalpy, where a lower ΔH_2 minimises the energy required for dehydrogenation. This figure shows that BT aligns closely with the optimal range for desirable H_2 wt.% and dehydrogenation enthalpy.

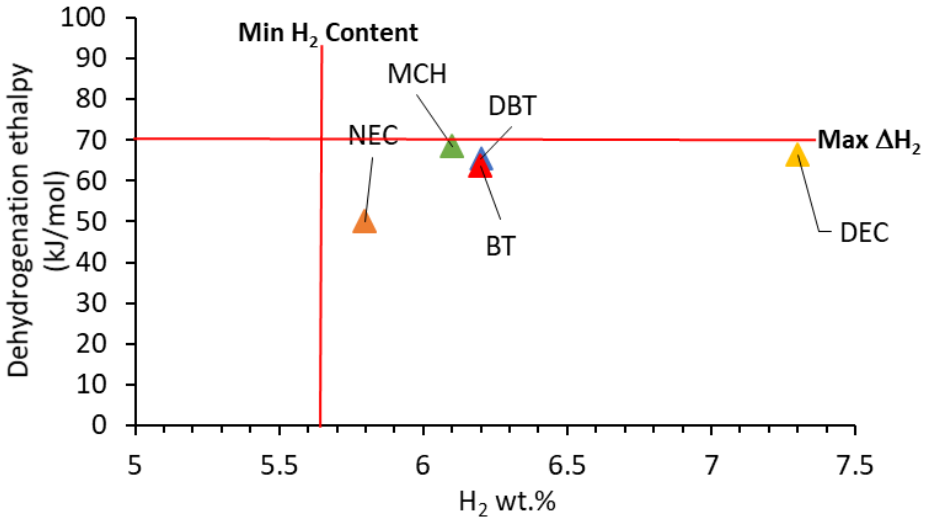

Figure 2.2. Hydrogen storage density versus dehydrogenation enthalpies of LOHC pairs (adapted from (Sage *et al.*, 2024). (BT: benzyltoluene; DBT: dibenzyltoluene; DEC: perhydro-N-ethylcarbazole (H12-NEC); MCH: methylcyclohexane; NEC: N-ethylcarbazole)

2.2.1 Decalin–naphthalene

Naphthalene and its corresponding hydrogenated equivalent, decalin, were investigated as a LOHC pair, as the latter has a high hydrogen storage capacity of 7.3% (Ninomiya *et al.*, 2006). Although it offers a high hydrogen storage capacity, naphthalene has a melting point of 80 °C, which means that it is a solid at room temperature (Rao & Yoon, 2020). This therefore affects transport and restricts the practical application of this LOHC pair. The dehydrogenation reaction for this LOHC pair also has a high heat demand (66.3 kJ/mol H_2) and is irreversible (Rao & Yoon, 2020). Catalyst selection and optimisation plays an important role in managing some of the issues associated with decalin/naphthalene dehydrogenation (Rao & Yoon, 2020). Hodoshima *et al*., however, developed a new Pt-Re/C catalyst, which was shown to improve decalin dehydrogenation (Rao & Yoon, 2020). The usual reaction temperature of 440 °C was reduced to a temperature in the range 210–280 °C for both batch wise and continuous-type reactors (Ninomiya *et al.*, 2006).

A carbon support has many advantages, including a high surface area and porosity, and surface functional groups that support catalytic dehydrogenation by providing more active sites and providing better mass transfer (Volynkin *et al.*, 2015). However, disadvantages of carbon as a support material, compared to the more common supports (silica/alumina), include its instability in oxidative environments, coke formation in low-density and high-temperature oxidative processes, which

complicates the handling of such supports (Volynkin *et al.*, 2015).

2.2.2 MCH–toluene

Another thoroughly investigated LOHC system, methylcyclohexane (MCH) and the dehydrogenated counterpart, toluene, was introduced because of the bulk availability of toluene. This system has a hydrogen storage capacity of 6.2% and is suitable for long-distance transportation due to its liquid state (Preuster, Papp*, et al.*, 2017). However, toluene is a volatile and flammable molecule, which prevents the practical application of this pair (Preuster, Papp*, et al.*, 2017). The continued utilisation of MCH as a LOHC system, however, is due to its established reliability as a demonstrated technology with a competitive hydrogen storage capacity of 6.2 wt.%. Additionally, research within Friedrich-Alexander-Universität Erlangen-Nürnberg (FAU), has focused on the optimisation of catalytic processes for MCH dehydrogenation with promising results pertaining to activity, selectivity and stability (Preuster, Papp*, et al.*, 2017). The high dehydrogenation temperature (<300 °C) and the high hydrogen pressure, nonetheless, present disadvantages for this LOHC system (Lin & Bagnato, 2024). Previous studies carried out by Sinfelt explored Pt-based catalysts for the dehydrogenation of MCH; however, issues with deactivation, coke formation and side product formation arose (Sinfelt, 1977, 2000). In 2018, Yan *et al*. introduced a new catalyst, Pt-Sn on a Mg-Al metal oxide support, which showed enhanced MCH dehydrogenation activity, high anti-coking ability and good stability (Yan *et al.*, 2018). However, a disadvantage here was that an additional separation step is required, due to the low boiling point of the LOHC system (100 °C), in order to purify the H_2 gas released (Alconada & Barrio).

Bimetallic catalysts such as Pt-Mn and Pt-Sn, together with catalytic supports such as Al_2O_3 and SiO_2, play a significant role in improving catalytic performance (Al-ShaikhAli *et al.*, 2015). Studies on different Sn contents revealed better performance with PtSn-5/Mg-Al-350; it exhibited better catalytic activity and high MCH conversion (Al-ShaikhAli *et al.*, 2015). Unfortunately, MCH dehydrogenation has a high heat demand (–68.3 kJ/ mol H_2) and extreme conditions are required for dehydrogenation (Schildhauer *et al.*, 2001).

There are two further issues with the MCH/toluene LOHC system. First, the system has a low boiling point (100 °C), which affects the reversibility (Geburtig *et al.*, 2016). Second, although the shipping and storage of LOHCs can be done under ambient conditions using existing systems for hydrocarbons, the toluene–MCH (as well as other most efficient carriers) has high capital costs (Rao & Yoon, 2020).

2.2.3 N-ethylcarbazole/ Dodecahydro-N-ethylcarbazole

The N-ethylcarbazole (NEC)/ Dodecahydro-N-ethylcarbazole (H12-NEC) LOHC system was investigated

to reduce the heat of dehydrogenation and allow the reaction to be carried out under milder conditions, while also offering a hydrogen storage capacity of 5.8% (Aakko-Saksa *et al.*, 2018). The dehydrogenation kinetics of NEC/H12-NEC are good when the most common catalyst for this system (Pd or Pt) is used. A disadvantage of this system is that while the melting point for NEC (67 °C) is lower than that of the ethylcarbazole it is solid when fully dehydrogenated, preventing the use of this as a LOHC system (Markiewicz *et al.*, 2015). A solution to this would be to heat the tank to its melting temperature of 67 °C or to limit the DOD to 90% to ensure that the mixture is a liquid. However, this reduces hydrogen storage capacity to 5.2% (Markiewicz *et al.*, 2015).

H12-NEC, a liquid at room temperature, has a hydrogen storage capacity of 5.8 wt.% and a volumetric capacity of 54 g L^{-1}, with a boiling point <200 °C; therefore, it is a potential candidate for liquid-phase hydrogen storage applications (Zhu & Xu, 2015). The most common catalyst used with this LOHC pair is Pd-supported catalysts, extensively studied by Sotoodeh *et al.* They showed that the dehydrogenation reaction is structure sensitive, and the dehydrogenation rate is slower than when compared to the dehydrogenation of H12-NEC (Sotoodeh *et al.*, 2012).

2.2.4 Dibenzyltoluene – Perhydro-dibenzyltoluene

Currently, the most favourable LOHC is the heat transfer oil, H-DBT—also known as Marlotherm SH®—due to its excellent hydrogen storage characteristics of 6.2% (Müller *et al.*, 2016). H0-DBT has a melting point in the range –39 °C to –34 °C, a boiling point of 390 °C, and a dehydrogenation temperature range of 280–360 °C (Brückner *et al.*, 2014). This high dehydrogenation temperature hinders its practical application, however.

2.2.5 BT–H12-BT

BT offers a promising LOHC system, with chemical characteristics similar to those of DBT, including a melting point of –30 °C, a boiling point of 280 °C and a gravimetric hydrogen content of 6.2 wt.%. BT can be safely used under boiling conditions at atmospheric pressure, whereas DBT undergoes thermal decomposition when heated to a boiling temperature of 370 °C (Geißelbrecht *et al.*, 2020).

Each LOHC system has distinct limitations that impact its practical implementation. The benzene/cyclohexane LOHC system has carcinogenic concerns and requires high operating temperatures, while the decalin/naphthalene LOHC system is limited by the solid-state naphthalene at ambient temperature and the high dehydrogenation enthalpy, making transportation difficult. Although well investigated, the MCH/toluene system also has drawbacks, such as a high dehydrogenation temperature, flammability, and the requirement for an additional separation processes due to the low boiling point. The NEC/H12-NEC LOHC system is limited by its solid-state

dehydrogenated phase, which necessitates heating or partial dehydrogenation, reducing the hydrogen capacity. Despite its favourable LOHC properties, DBT requires high dehydrogenation temperatures, limiting its effectiveness. Finally, while BT is a potential option with a lower boiling point and faster hydrogen release, it has to be further optimised for large-scale applications.

2.3 By-product Formation During Dehydrogenation of BT

2.3.1 Mechanism of by-product formation

In the dehydrogenation of H12-BT to the final product HBT, the only significant intermediate is H6-BT. This indicates that the HBT/H12-BT system is less complex in comparison to the H0-DBT/H18-DBT system as there are fewer intermediate products formed (Leinweber & Müller, 2018). (Dao *et al.*, 2024). Previous research has indicated that fluorene species are produced through an oxidative cyclisation of HBT, occurring during the process of H_2 release. According to Kerscher et al., the formation of by-products, mainly methylflourene (m-fluorene), occurs in the LOHC systems (Kerscher *et al.*, 2023) through repeated dehydrogenation cycles. This occurs at high temperatures, where the concentration of m-fluorene increases with an increasing number of LOHC cycles (Kerscher *et al.*, 2023). A proposed reaction for the formation of m-fluorene is shown in Figure 2.3.

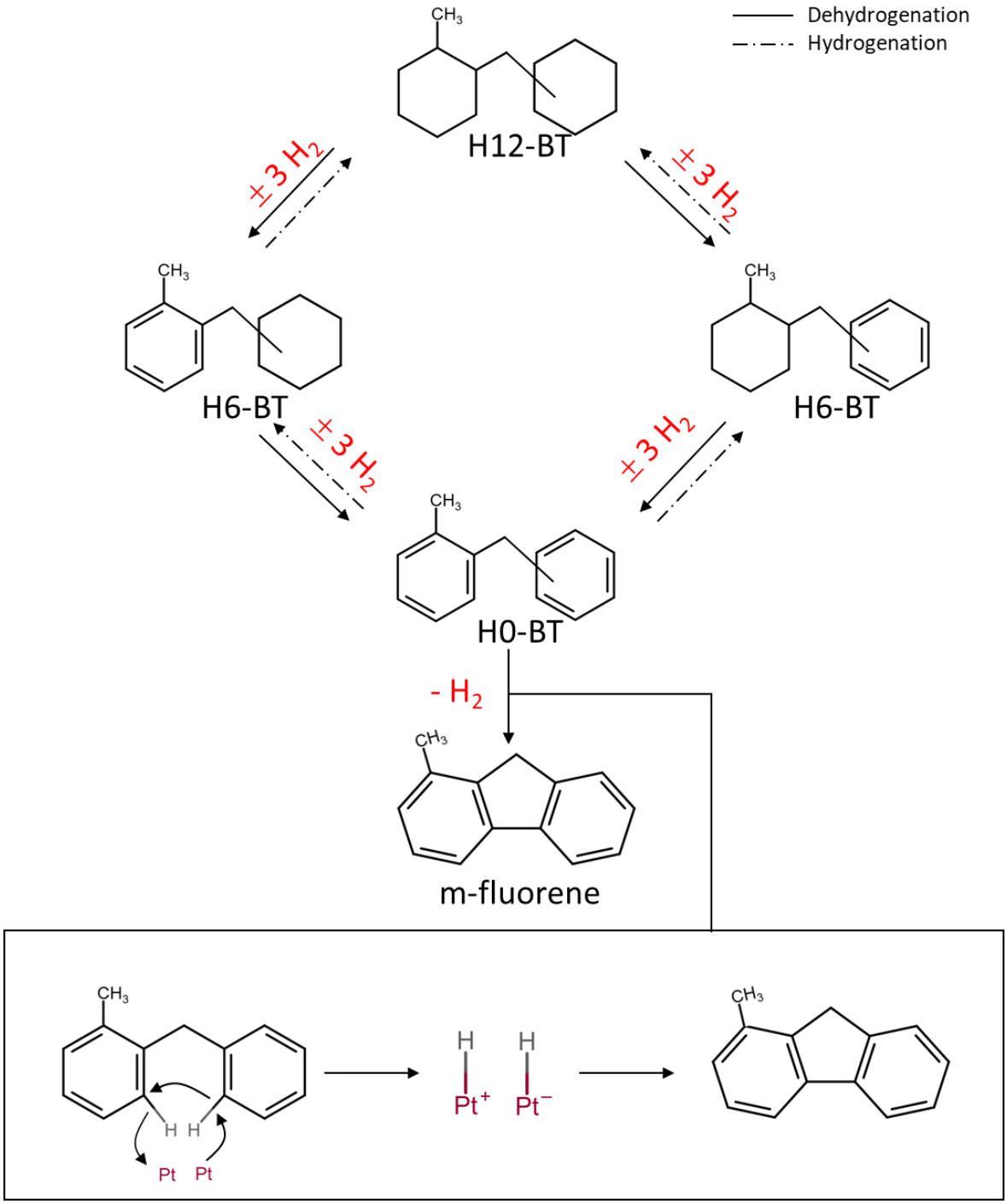

Figure 2.3. Reaction scheme illustrating the dehydrogenation of H12-BT (H12-BT), highlighting the formation of intermediates H6-BT and the final product, benzyl toluene (HBT) here. The scheme also depicts the proposed dehydrogenative cyclisation route leading to the formation of methylfluorene (m-fluorene) during the dehydrogenation of H12-BT. (Adapted from (Alconada & Barrio, 2024).

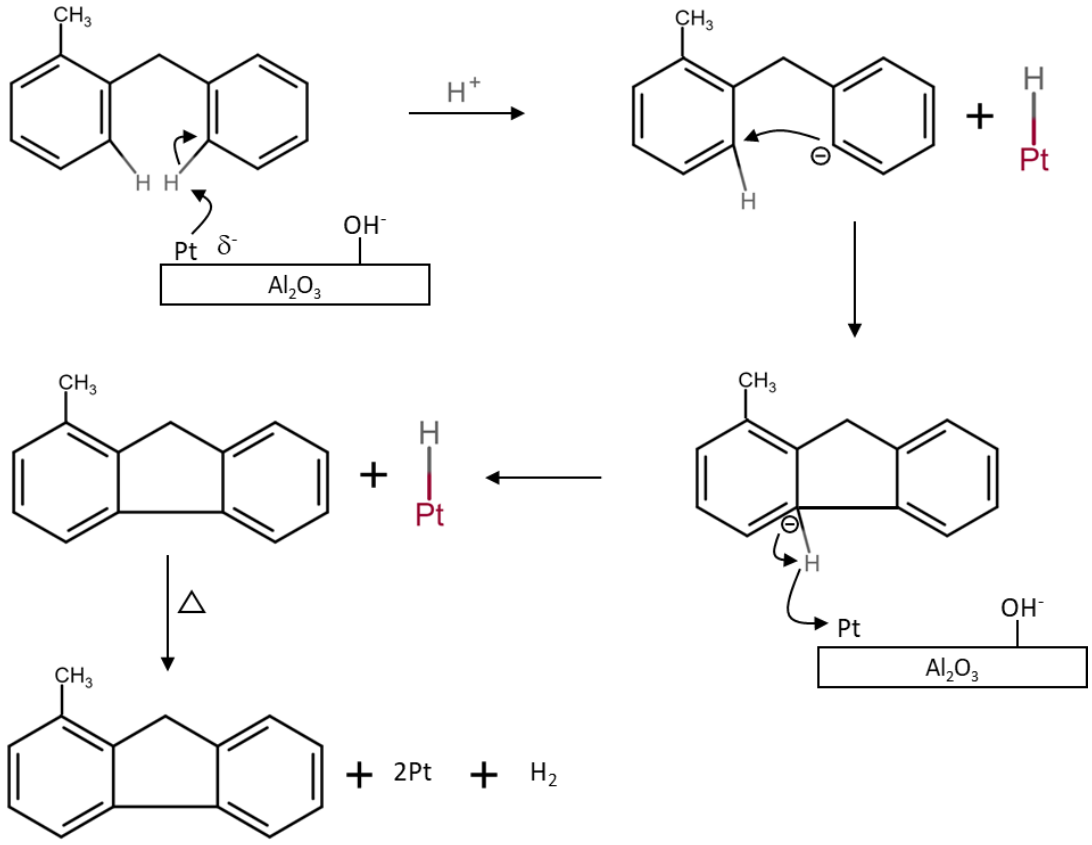

Figure 2.4. Reaction scheme of the proposed nucleophilic attack during by-product formation.

Previous research has established the formation of m-fluorene as a by-product from the dehydrogenation of cyclohexane (Rüde *et al.*, 2022). The proposed mechanism for this production involves the initial activation of hydrogen bound to the electron-deficient carbon–carbon bond, followed by the release of a hydrogen molecule (H_2) from the HBT, resulting in the formation of m-fluorene (Alconada & Barrio, 2024). It was suggested that the formation of by-products is significantly influenced by the concentration of HBT here over time and that increased activity leads to a higher yield of m-fluorene after a reaction time of 4 h (Alconada & Barrio).

2.3.2 Influence of reaction conditions on by-product yield

Studies have shown that the optimal temperature for the H18-DBT dehydrogenation is at 290 °C (Ali *et al.*, 2022), while a high H_2 production was observed for H12-DBT at 270 °C (Brückner *et al.*, 2014). The kinetics of the dehydrogenation reaction have been extensively researched for the following catalysts: 1 wt.% Pt/Al_2O_3, 1 wt. % Pd/Al_2O_3 and 1:1 wt.% $P\text{-}Pd/Al_2O_3$. The best results were seen when a 1 wt. % Pt/Al_2O_3 catalyst was used—82% DOD was observed (Modisha, Gqogqa*, et al.*, 2019). The optimal Pt metal loading on $Pt/\gamma\text{-}Al_2O_3$ catalysts (1%–5%) was determined and a 5% $Pt/\gamma\text{-}Al_2O_3$ found

to be the most active catalyst—90.2% stored hydrogen was obtained after 7 h. It was evident that as the catalyst dosage increased, the reaction rate and hydrogen yield increased (Ali *et al.*, 2022).

Table 2.2 Properties of the H0-DBT/H18-DBT and HBT/H12-BT system (Brückner *et al.*, 2014), (Müller *et al.*, 2015), (Modisha *et al.*, 2018).

Parameter	**H0-DBT**	**H18-DBT**	**HBT**	**H12-BT**
Molar mass (g/mol)	272.39	290.54	182.27	194.36
Density, kg/m^3 @ 20 °C	1044	913	996	876
Viscosity, mPa.s @ 20 °C	49	389	3.94	6.97
Δ dehydrogenation enthalpy (kJ/mol H_2)	–65.4	65.4	–65.4	65.4
Gravimetric capacity, wt. %	-	6.2	-	6.2
Boiling point, °C	-	364.95	-	270
Volumetric capacity, kg/L m^3	-	56.4	-	57

The effective release of hydrogen from H18-DBT and H12-BT required a high temperature, where the molecule the size of the H12-BT has a thermodynamic disadvantage compared to H12-BT, as the diffusivity of H12-DBT in the porous catalyst is slow (Jorschick *et al.*, 2020). To decrease the reaction energy barrier of the dehydrogenation reaction, research into a lower dehydrogenation temperature and obtain more hydrogen energy with less heat consumption have been focused mainly on the catalyst (Shuang *et al.*, 2020), (Brigljević *et al.*, 2020). A catalyst that facilitates the high efficiency of H12-BT dehydrogenation is Pt/γ-Al_2O_3 (Alconada & Barrio, 2024).

2.4 Catalysts and Preparation Methods

2.4.1 Common catalysts and support materials

The well-known catalysts used for organic compound hydrogenation and dehydrogenation in industry include, but are not limited to, Pt, Pd, Ru, Ni and Cu (Modisha, Gqogqa*, et al.*, 2019). These metal catalysts are loaded onto porous supports such as SiO_2, V_2O_5, TiO_2 and Al_2O_3 (Shukla *et al.*, 2010). Al_2O_3 is the most commonly used support material here due to its large surface area and low rather cost (Oh *et al.*, 2019). Unfortunately, the precious metals catalysts are costly and therefore, to achieve

economic competitiveness of LOHCs, extremely active dehydrogenation catalysts must be developed (Lee *et al.*, 2021). To develop catalysts for improved dehydrogenation, it is necessary to have large porous surface areas that have a good distribution of the active material (Jeyaraj *et al.*, 2019). The catalytic activity and dehydrogenation temperature can be reduced by synthesising Pt/γ-Al_2O_3 catalysts with more active sites and an appropriate structure of Pt NPs (Shi *et al.*, 2020).

2.4.2 Role of Pt/γ-Al_2O_3 in LOHC systems

Pt/γ-Al_2O_3 serves as a heterogeneous catalyst in LOHC systems, playing a crucial role in facilitating dehydrogenation reactions. Heterogeneous catalysts such as Pt/Al_2O_3 are particularly suitable for potential LOHC systems due to their thermal stability, recyclability, and ease of separation from the LOHCs. Furthermore, heterogeneous catalysts are responsive to both continuous flow and batch dehydrogenation processes, facilitating scale-up for industrial hydrogenation and dehydrogenation operations (Cho *et al.*, 2021). However, issues such as high cost, possible catalyst deactivation and sintering at high temperatures demand further optimisation (Union, 2021). Doping with secondary metals (such as Mg or Zn) can improve catalytic performance and long-term stability for LOHC applications (Garidzirai *et al.*, 2021).

Theoretically, the use of LOHCs can be infinite in the absence of side reactions; however, the catalyst used for the dehydrogenation of H18-DBT is susceptible to side reactions, deactivation and low catalytic performance (Modisha, Gqogqa*, et al.*, 2019). Modisha and Bessarabov have identified by-products present during the tenth cycle of dehydrogenation when using the LOHC DBT with a 1 wt.% Pt/γ-Al_2O_3 catalyst (Modisha & Bessarabov, 2020). Methane gas was obtained in the gas phase after dehydrogenation, and the following liquid phase by-products were obtained: from the most to the least, HBT, toluene, C13–C15, xylene and benzene (Modisha & Bessarabov, 2020).

2.4.3 Wet impregnation

A standard and common technique for depositing metal precursors onto a solid support is wet impregnation—it is used to prepare catalysts. The wet impregnation method is the most widely used here due to ease of use and cost effectiveness (Munnik *et al.*, 2015). Wet impregnation uses excess precursor solution compared to the support's pore volume, resulting in a thin slurry (Mehrabadi *et al.*, 2017). The solution is then evaporated out and undergoes calcination, followed by reduction above 300 °C (Mehrabadi *et al.*, 2017). See Figure 2.5. Lee et al. compared catalysts that were prepared under both conventional (precipitation and impregnation) and advanced (polyol and ion exchange) (Lee *et al.*, 2015). The catalysts were prepared under the similar experimental conditions and tested using a batch dehydrogenation reactor, under reflux. The catalysts were characterised using TEM, XRD and

CO chemisorption. Both the advanced methods (polyol and ion exchange) showed a high dispersion of Pt particles, which resulted in increased hydrogen productivity (Lee *et al.*, 2015). As the Pt distribution increases, there is a larger surface area available for the reaction to proceed. Both the advanced methods are seen to yield a more efficient Pt catalyst for this specific reaction. The hydrogen evolution rate increases as follows: impregnation > precipitation > polyol > ion exchange (Lee *et al.*, 2015).

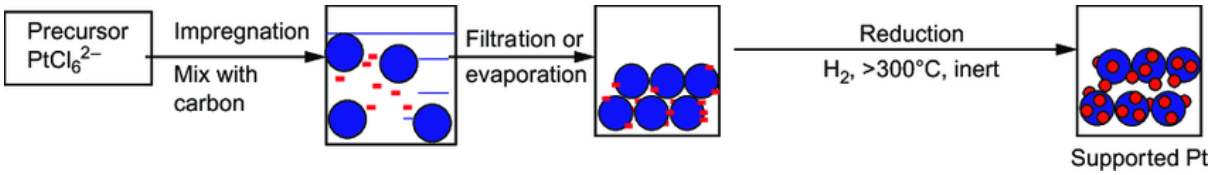

Figure 2.5. Schematic diagram of the wet impregnation method used to synthesise Pt on Al_2O_3 support. Modified from (Mehrabadi *et al.*, 2017).

2.4.4 Preparation of the catalyst slurry

Peters *et al.* coated metal spheres using a spray coating technique and ion-exchange impregnation, as follows. A wash coat was created using Puralox powder and HNO_3 to create a 1:2 binder-filler solution (20 wt.% binder). The spray was applied to the metal spheres, dried, and then calcined at 550 °C for 6 h. Pt deposition was achieved through ion-exchange impregnation using hexachloroplatinic acid. The catalysts were calcined at 330 °C for 6 h and reduced before reacting with hydrogen at 300 °C for 2 h (Peters *et al.*, 2015).

Another method for coating the eggshell catalysts involves dip-coating with a prepared catalyst. A γ-Al_2O_3 slurry was created by dispersing commercial γ-Al_2O_3 powder in boehmite sol to form a coating slurry with a solids content of 35%. After stirring for 10 h, the dispersions were suitable for deposition. Pre-treated samples were dipped into the coating slurry, dried and then calcined at 500 °C for 2 h (Zhao *et al.*, 2003).

Yet a further dip-coating method involves creating a slurry by combing alumina powder and a PVA solution (2 wt.%) as a binder. The coating was performed manually (in a beaker), with drying overnight at 60 °C. The samples were then heated to 1150 °C at 3 °C/min.

2.4.5 Comparison of commercial catalysts

Brückner *et al.* screened commercial catalysts for the dehydrogenation of H18-DBT under similar conditions and found that Pt on C or AlO_x is more active compared to Pd on the same supports (Brückner *et al.*, 2014). A 0.5 wt.% Pt/γ-Al_2O_3 (0.5 wt.%) resulted in 10.4 L of H_2 being produced with a 51% DOH (Brückner *et al.*, 2014). It was further shown that increasing the loading of Pt on the supports

increases the dehydrogenation performance, resulting in greater hydrogen volumes with increased loadings.

The development of new catalysts is required in efforts to accelerate dehydrogenation and hydrogenation. To this end, the development of such catalysis should allow for mild reaction conditions by reducing the activation energy (E_a) and controlling the kinetics (Cho et al., 2021). Jiang et al. reported that the most effective catalysts for the dehydrogenation of H12-NEC are ranked as follows: Pt, Pd, Rh, Au and Ru. However, the cost of these precious metals significantly impacts overall expenses, both financially and environmentally (Jiang *et al.*, 2019).

2.4.6 Future developments in catalyst design

The catalysts employed in LOHC dehydrogenation play a critical role in determining the reaction kinetics, selectivity, and by-product formation. Although significant progress has been made in catalyst development, challenges do remain—in terms of by-product formation, catalyst activity and stability, and selectivity. Many catalysts employed in LOHC dehydrogenation tend to afford undesirable by-products, which not only reduce the overall hydrogen yield but also require additional refining steps, thus further increasing the operational costs. The efficiency and longevity of catalysts during repeated dehydrogenation cycles are crucial for industrial applications. Catalysts must maintain high activity and stability to ensure continuous and reliable hydrogen production (Choi *et al.*, 2024). Furthermore, achieving high selectivity towards the desired hydrogen release pathway is essential to minimise the formation of undesired by-products.

2.5 Heating Methods in Catalytic Dehydrogenation Processes

2.5.1 Electrical heating: Efficiency limitations

Due to the high reaction temperature that is required for the release of hydrogen through the dehydrogenation of LOHC molecules, DBT/BT, an energy-efficient heating method is required. Various methods can be used to provide continuous heat for the endothermic dehydrogenation reaction. Electrical heating is convenient and allows the direct transfer of heat to the reaction (Müller, 2019). However, it presents major disadvantages, e.g., slow heating and cooling rates, non-uniform temperature distribution and low energy efficiency (Wang *et al.*, 2019).

Muller *et al.* reported that when using electric heating to provide heat to the dehydrogenation unit, 32.9 ± 23.4 kJ mol^{-1} H_2 of electric energy is provided (Müller *et al.*, 2019). This leads to an efficiency of 13.6 ± 9.7% hydrogen released from the bound LOHC. The reason for the low efficiency of hydrogen energy is a direct result of the inefficient heat provided by electric heating. Another disadvantage of

using electrical heating during dehydrogenation reactions is that approximately 20% of the total energy required for dehydrogenation is lost to pre-heating the reactor and heat loss to the surroundings. Teichmann *et al.* have shown that electrical heating is the least efficient method that can be used for heating in the dehydrogenation process, and, despite its convenience, it is unsuitable for energy applications (Teichmann, Stark*, et al.*, 2012).

2.5.2 Utilisation of a hydrogen burner as an alternative heating method

An alternative heating method to the abovementioned rather unsuitable electrical heating can be used—a hydrogen burner is utilised to supply heat to the reactor (Teichmann, Arlt*, et al.*, 2012). A hydrogen burner (a well-established technique) functions by harnessing a portion of the hydrogen generated during the reaction to furnish the requisite heat. This is achieved by burning a portion of the hydrogen produced during the reaction to provide such heat, while the rest of the hydrogen goes to the PEMFC (Modisha, Ouma*, et al.*, 2019). Although employing a hydrogen burner presents an improvement in energy efficiency, achieving a 34% efficiency compared to the 24% seen with electric heating, it is nonetheless noteworthy that both heating methods can adversely impact the efficiency of the dehydrogenation reaction itself (Teichmann, Stark*, et al.*, 2012). The deployment of either of these heating techniques results in a substantial reduction in the efficiency of the dehydrogenation process, underlining the complexity of optimising both energy consumption and the reaction's effectiveness within this framework (Teichmann, Stark*, et al.*, 2012).

Current conventional electrical heating methods for LOHC dehydrogenation are energy-intensive, leading to increased operational costs and adverse environmental impacts. Moreover, prolonged exposure to high temperatures can cause thermal degradation of the LOHC molecules and the catalyst, reducing the overall efficiency and lifetime of the dehydrogenation process. Therefore, an alternative and more efficient heating method is sought to address these challenges.

2.5.3 Inductive heating as an efficient alternative heating method

Electromagnetic inductive heating is an alternative heating method that can improve on the limits of both electrical heating and hydrogen burners (Abu-Laban *et al.*, 2017). Inductive heating is a non-contact heating method that works by using electromagnetic inductive , which induces electric currents within conductive materials, such as SS or iron pellets, causing them to heat up (Abu-Laban *et al.*, 2017). This results in a catalyst bed that functions as a heat generator rather than a typical heat sink as seen with conventional heating methods (Abu-Laban *et al.*, 2017).

Hart *et al*. drew a comparison between the conventional heating method and inductive heating (Hart *et al.*, 2020a). When inductive heating is used to heat the reactor, heat flows directly from the

inductively active material to the surrounding fluid and catalyst pellets. This results in efficiency since heat is generated from the load and there is no heat loss to the environment. When electrical heating is used to heat the reactor, the heat flows from the reactor to the surrounding fluid and then to the catalyst, leading to a temperature gradient of 5 °C between them. The difference in temperature has a significant effect on tetralin conversion, resulting in slower kinetics.

2.5.4 Advantages of inductive heating

In the context of LOHC dehydrogenation, inductive heating offers numerous advantages over conventional electrical heating. By targeting specific areas, inductive heating minimises heat loss to the surroundings and maintains a consistent temperature throughout the reactor (Wang *et al.*, 2019). This efficiency enhancement has the potential to reduce energy consumption and reduce operational expenses (Hart *et al.*, 2020a). Moreover, the localised heating capability of inductive heating safeguards the LOHC and catalyst from extreme temperatures, mitigating thermal degradation, and bolstering the stability and longevity of the dehydrogenation system (Wang *et al.*, 2019). As a result, inductive heating achieves rapid heating rates, uniform temperatures, and allows the catalyst to reach high temperatures without requiring reactor preheating, which is a critical advantage to optimise large-scale hydrogen production and streamlining industrial processes.

2.5.5 Mechanisms of inductive heating

To delve deeper into the benefits of inductive heating, it is essential to understand the underlying mechanisms that make it a superior heating method for LOHC dehydrogenation. Inductive heating operates on the basis of the principles of electromagnetic inductive . When an alternating current is passed through a conductive coil, it generates an alternating magnetic field around the coil (Gergely & Hochenauer, 2023). When a conductive material, e.g. metal, is placed within this magnetic field, eddy currents are induced within the material due to its electrical conductivity (Gergely & Hochenauer, 2023). These eddy currents generate efficient and localised heating within the material. Inductive heating excels in transferring heat directly to the LOHC molecules without relying on heat conduction through solid walls, which is the case in conventional electrical heating methods (Idakiev *et al.*, 2015).

In conventional methods, the reactor walls may absorb a significant amount of energy, leading to heat loss and reduced efficiency. In contrast, inductive heating directly energises the LOHC molecules, resulting in minimal energy wastage (Wang *et al.*, 2019). When the alternating current is turned off, the magnetic field dissipates quickly, resulting in immediate cooling of the LOHC material. This on–off control allows for precise temperature management, promoting energy conservation, and reducing the overall energy consumption during the dehydrogenation process. Inductive heating enables

precise and localised heating of the LOHC material (Wang *et al.*, 2019).

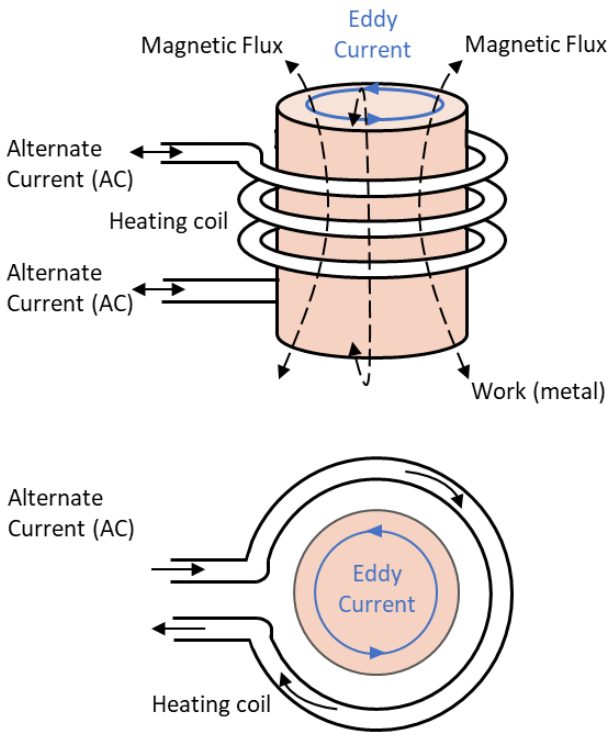

Figure 2.6. Schematic diagram of the principle of inductive heating (adapted from Technologies).

The magnetic field is focused on the region of interest, ensuring uniform heating throughout the material. This uniformity prevents hotspots and temperature variations that could lead to thermal degradation or undesirable reactions. As a result, the risk of catalyst deactivation and side product formation is minimised, leading to improved efficiency and product quality (Huang *et al.*, 2023). The rapid and uniform heating provided by inductive heating translates into shorter dehydrogenation times compared to conventional electrical heating methods. Faster reaction rates allow for increased throughput in industrial applications, reducing overall production time and increasing productivity (Schörner *et al.*, 2024). Furthermore, shorter dehydrogenation times help to mitigate potential catalyst deactivation issues, as the catalyst is exposed to high temperatures for shorter periods, thereby improving its stability and longevity. Advancements in heating methods, reaction efficiency and catalyst longevity will contribute to making LOHC-based hydrogen storage and transportation systems more sustainable, cost-effective and practical for large-scale implementation (Wang *et al.*, 2019).

2.5.6 Inductive heating in industrial applications

Hart et al. investigated the use of inductive heating in the toe-to-heel air injection (THAI) process

combined with catalytic upgrading for oil production; they found that inductive heating improved the catalytic activity and reaction rate, although coke formation increased (Hart *et al.*, 2020a). The integration of inductive heating into the *in situ* catalytic upgrading process (CAPRI) zone of the THAI process will be beneficial to heavy oil upgrading, as most cracking reactions are endothermic, and would enhance hydrogen gas liberation to promote *in situ* hydroconversion.

2.6 Inductively Active SS Spheres: Properties and Applications

2.6.1 Advantages of eggshell catalysts

According to Peters *et al.,* eggshell catalysts possess a distinctive structure that confers multiple advantages compared to traditional catalysts (Peters *et al.*, 2015). These benefits encompass a larger surface area, an even dispersion of active sites and reduced diffusion resistance (Peters *et al.*, 2015). These characteristics collectively facilitate efficient mass transfer of reactants and products —a key factor in fine-tuning the dehydrogenation process for optimal results (Peters *et al.*, 2015). In pursuit of enhancing hydrogen productivity, researchers have undertaken the preparation of eggshell catalysts featuring precisely defined active layer thicknesses, aiming to leverage their effectiveness (Peters *et al.*, 2015).

2.6.2 Inductive heating using metal spheres

Using metal spheres for inductive heating in dehydrogenation processes offers several distinct advantages, making them a compelling choice for enhancing thermal efficiency during dehydrogenation (Peters *et al.*, 2015). These metal spheres, often constructed from materials such as iron or steel, exhibit exceptional heat-generating capabilities due to their high electrical conductivity and swift heat generation when exposed to an alternating magnetic field (Wang *et al.*, 2019). A key advantage of employing metal spheres lies in the uniform distribution of heat that they facilitate during the inductive heating process (Wang *et al.*, 2019). Their spherical shape allows the even dispersion of heat throughout the material being heated, ensuring consistent and meticulously controlled temperature profilesIdakiev *et al.*, 2015)(Idakiev *et al.*, 2015)(Idakiev *et al.*, 2015)(Idakiev *et al.*, 2015)(Idakiev *et al.*, 2015)(Idakiev *et al.*, 2015)(Idakiev *et al.*, 2015). This uniform heating characteristic mitigates the potential for localised hotspots or thermal gradients that could lead to unintended reactions or degradation of the reactants (Idakiev *et al.*, 2015).

Metal spheres also excel in terms of energy transfer efficiency during inductive heating. Their innate conductivity allows for rapid absorption and dissipation of heat, thereby contributing to accelerated and effective heating rates (Hart *et al.*, 2020b). This efficiency is of particular significance in

dehydrogenation processes, where swiftly attaining the desired reaction temperature can significantly enhance reaction kinetics and overall process efficacyHart *et al.*, 2020b)(Hart *et al.*, 2020b)(Hart *et al.*, 2020b)(Hart *et al.*, 2020b)(Hart *et al.*, 2020b)(Hart *et al.*, 2020b). Furthermore, the utilisation of metal spheres as heat sources introduces a versatile approach to dehydrogenation. Tailoring their size and composition to match specific process requirements permits a high degree of flexibility in designing and optimising the inductive heating arrangement to suit various reaction scales and reactant materials.

The use of spherical metal pellets allows for uniform heat distribution and rapid heat transfer, and the nature of the eggshell offers advantages such as increased surface area, uniform dispersion of active sites and reduced diffusion resistance (Peters *et al.*, 2015; Wang *et al.*, 2019). The Curie temperature of SS is in the range 720–750 °C. SS is preferred due to its combination of strong mechanical properties, corrosion resistance, excellent heat resistance, low cost and ready availability (Ara, 1989).

2.6.3 Material selection for inductive heating

Recently, Schörner *et al.* investigated the use of inductive heating as a direct heating method for the dehydrogenation of H18-DBT through the use of Pt-based catalyst materials. This research introduced three types of Pt-alumina catalysts, including Pt-alumina on SS beads, Pt-alumina prepared on a flat FeCrAl plate, and an α-alumina core with a γ-alumina shell, including spray-dried Pt impregnated FeO NP accumulation (Schörner *et al.*, 2024). This research found that inductively heated catalysts maintained higher surface temperatures, resulting in optimised heat management and reduced heat losses, thus enhancing energy efficiency and process control. Stability tests showed no degradation of the catalysts, indicating long-term operational viability.

Recent studies show that eggshell catalysts offer advantages such as an increased surface area, even dispersion of active sites, and reduced diffusion resistance, thus facilitating efficient mass transfer of reactants and products. The use of a metal sphere as an inductively active material allows rapid heat generation and uniform heat distribution. Inductive heating has been found to improve catalytic activity and the reaction rate in the THAI process for oil production. Schörner et al. investigated using inductive heating for the dehydrogenation of H18-DBT using Pt-based catalyst materials and reported fast heating rates and dynamic hydrogen release without the drawback of by-product formation in H18-DBT.

2.7 Catalyst Characterisation

2.7.1. Inductively coupled plasma–optical emission spectroscopy

ICP-OES serves a dual role: confirming catalyst loading against target levels and providing elemental composition data. ICP-OES is used to determine the Pt concentrations in the catalysts.

2.7.2. Brunauer–Emmett–Teller

BET is the most widely used method to determine surface area measurements. The BET equation can calculate the specific surface area of solid materials based on gas adsorption measurements. Nitrogen is the most widely used absorbate for surface probing by BET methods. Therefore, nitrogen adsorption isotherms are conducted at the boiling point of nitrogen (77K) (Zou *et al.*, 2021). The BET surface area is calculated according to equation 1.1 (Tarleton, 2014).

Herein, V represents the volume of absorbed molecules and V_m is the volume of nitrogen absorbed at STP. The constant c_{BET} correlates with the adsorbate–absorbent interaction strength within the initial adsorbed layer and gives the heat of adsorption. The greater the value of c_{BET}, the stronger the interaction between the adsorbate–absorbent. The x is the relative pressure P/P_0, where P is the pressure at time t and P_0 is the saturation pressure of the absorbate.

$$\frac{x}{V(1-x)} = \frac{1}{V_m \cdot c_{BET}} + \frac{x \cdot (c_{BET}-1)}{V_m \cdot c_{BET}} \quad \ldots(1.1)$$

BET analysis imposes a minimum pore size criterion of 1.7 nm—it typically focuses on characterising the porosity and surface area of materials with micropores (pore size <2 nm) and mesopores (pore sizes 2–50 nm) (Centeno & Stoeckli, 2010; Wu *et al.*, 2020).

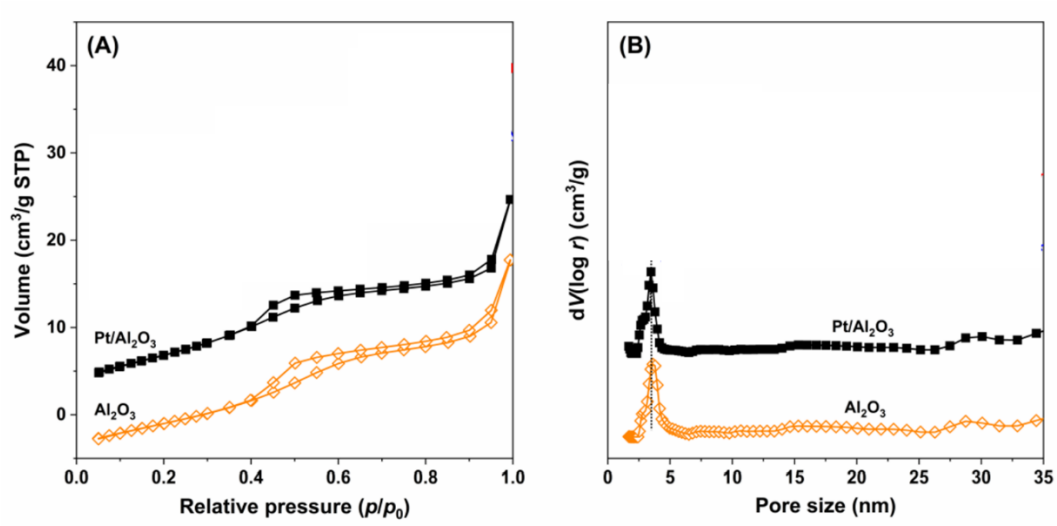

Figure 2.7. Typical N_2 adsorption–desorption isotherms (A) and pore size distribution (B) for mesoporous Al_2O_3 and Pt/γ-Al_2O_3 (Matsagar *et al.*, 2021).

The specific surface area, pore volume, average pore size and pore diameter distributions of Al_2O_3 samples were characterised by nitrogen adsorption and desorption at the liquid nitrogen temperature of 77 K. Results showed Al_2O_3 with a specific surface area (S_{BET}) of 301 m^2/g and 5 wt.% Pt/γ-Al_2O_3 with a S_{BET} of 230–267 m^2/g (Bhogeswararao & Srinivas, 2015; Mostafa *et al.*, 2019). Conventional forms of γ-Al_2O_3 have a pore volume 0.20–0.80 cm^3/g as a result of the synthesis method (Dabbagh *et al.*, 2011). The BET surface area of γ-Al_2O_3 is in the range 185–250 m^2/g (Dabbagh *et al.*, 2011; Zhang *et al.*, 2002). A mean pore diameter of γ- Al_2O_3 is 7.8 nm has been reported (Mostafa *et al.*, 2019).

2.7.3. CO pulse chemisorption

CO pulse chemisorption is instrumental in the investigation of the Pt/γ-Al_2O_3 catalyst system, where the metal dispersion (D_m), metal surface area (m^2/g) and particle size of Al_2O_3 can be determined. By using the interactions between adsorbates and the surface, this method accurately measures the active metal areas, thus contributing to understanding and improving catalyst performance.

Pulse measurements are used to quantify adsorption by comparing the peak area differences between unsaturated and saturated states. This process involves continuously introducing a constant of the adsorption gas to the sample until it reaches saturation. D_m is determined using CO_2 by measuring the surface area of the Pt/γ-Al_2O_3 sample from total gas consumption. The chemisorption technique directly measures the number of exposed surface atoms by evaluating the quantity of gas adsorbed selectively onto the metal at monolayer coverage.

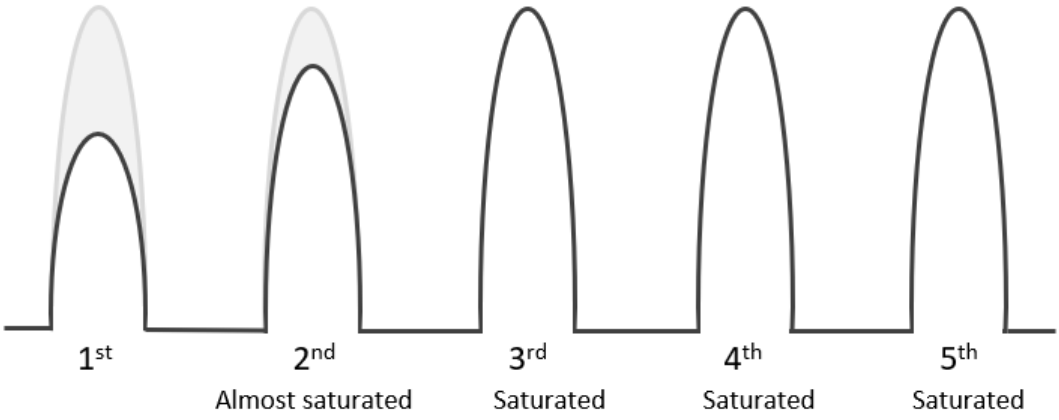

Figure 2.8. TCD waveform during measurement of the sample until saturated, adapted from Belcat II. Adapted from Microtrac.

D_m is quantified as a percentage of surface metal atoms relative to the total metal atoms within the sample. The dispersion is expressed as a ratio between the surface metal atoms and the total number of atoms. This equation is expressed as follows (equation 2.1):

$$Dispersion\ \% = \frac{Number\ of surface\ atoms}{Total\ number\ of\ atoms} \times 100 \qquad \ldots(2.1)$$

For Pt/γ-Al_2O_3, literature reports a 72% D_m at 290K and an average crystallite size of 1.4 nm (Karakaya & Deutschmann, 2012).

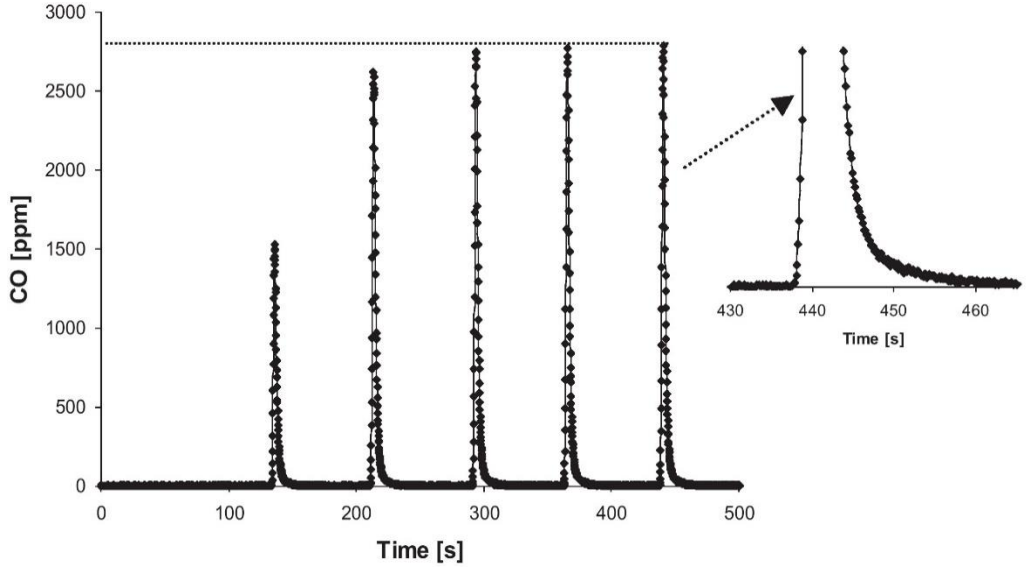

Figure 2.9. CO pulse chemisorption of Pt/γ-Al_2O_3 (Karakaya & Deutschmann, 2012).

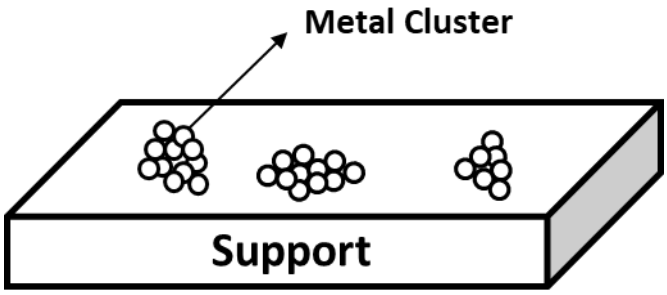

Figure 2.10. Example of metal clusters on a support surface detected by CO pulse chemisorption.

Catalysts that are prepared through the wet impregnation method result in a high concentration of active metals on the surface of the support (Al_2O_3). These active metals on the surface form metal clusters that limit the amount of metal available for the catalytic reaction. CO pulse chemisorption is used to characterise the D_m and active surface metal on the surface of the catalyst support. The method reduces the sample with H_2 to determine the amount of gas molecules adsorbed on the catalyst surface. This is followed by the reduction of the catalyst sample with H_2 at high temperature to ensure that all oxides are converted to their metallic forms. The sample is then purged with inert gas, and absorbate gas is introduced in pulses until the catalyst surface is saturated. The volume of

each pulse and number of pulses required to reach saturation is taken and used to calculate the total amount of chemisorbed gas (Ertl *et al.*, 1997).

2.7.4. Hydrogen temperature programmed reduction

The H_2-TPR is a crucial technique utilised to ascertain the precise conditions facilitating the reduction of Pt, thereby shedding light on the reduction process itself. By subjecting a sample to varying temperatures in a controlled hydrogen atmosphere, H_2-TPR offers valuable insights into the nature of metal–support interactions. Elevated temperatures during reduction indicate the presence of strong metal–support interactions, providing essential information regarding catalyst behaviour and performance.

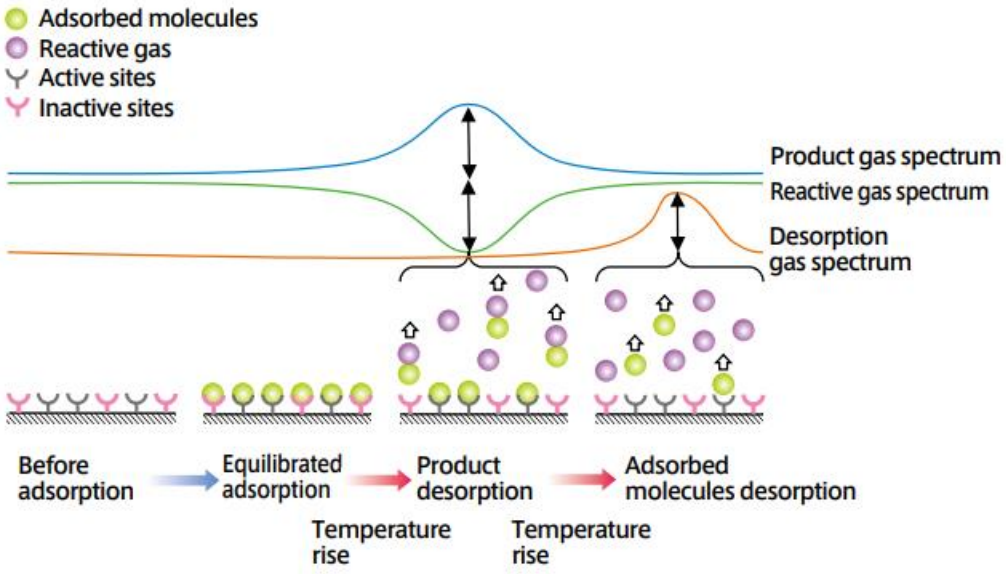

Figure 2.11. H_2-TPR data obtained from BELCAT II.

H_2-TPR is a method to measure oxidation/reduction characteristics and reactivity of adsorbed molecules by increasing the temperature of a solid under reactive gas flow. It allows for understanding reaction components, product distribution, and unreacted substances from their spectra. It makes it possible to measure temperature-dependent catalytic reactions continuously and to consider each stage of multistep reactions separately. TPR involves determining a sample's reduction temperature in a hydrogen atmosphere. It is commonly used in applications such as NOx reduction, CO oxidation, and organic heating processes (Microtrac). The H_2-TPR profile of 5 wt.% Pt/γ-Al_2O_3 in Figure 2.13 show H_2 consumption of 0.232 mmol/g (Bhogeswararao & Srinivas, 2015).

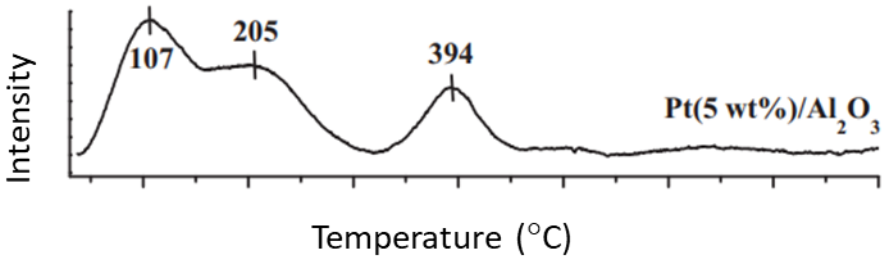

Figure 2.12. H_2-TPR profiles of 5 wt.% Pt/γ-Al_2O_3 (Bhogeswararao & Srinivas, 2015).

2.7.5. Scanning electron microscopy–energy dispersive X-ray spectroscopy (SEM-EDS)

SEM-EDS is a key tool for validating the presence of Pt in reduced catalysts. it also facilitates a comprehensive analysis of the morphology and distribution of catalyst particles adhering to SS substrates. Moreover, SEM-EDS methodology extends its utility in determining the thickness of Pt/γ-Al_2O_3 coatings, thereby contributing to a detailed characterisation of the catalyst structures.

2.7.6. Transmission electron microscopy (TEM)

TEM is also a key tool for analysing Pt NPs, particularly their size distribution and morphology pre- and post-dehydrogenation. TEM enables crystal structure analysis, lattice spacing determination, and determination of statistical metrics such as mean and mode sizes. It also identifies different Pt/γ-Al_2O_3 phases before and after dehydrogenation, which is crucial for understanding catalytic processes. TEM is essential for the comprehensive characterisation and optimisation of Pt NP catalysts.

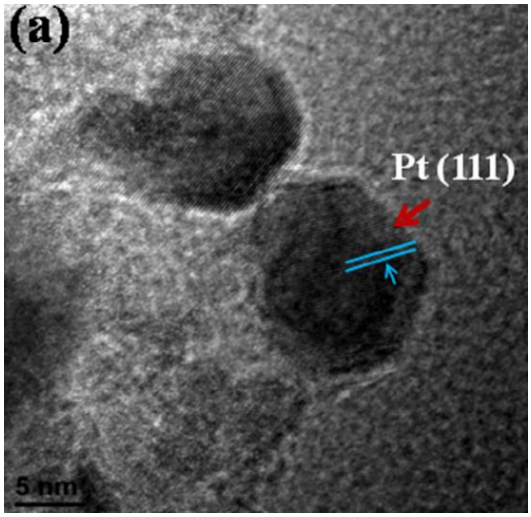

Figure 2.13. Typical HR-TEM image of 5 wt.% Pt/γ-Al_2O_3 (Bhogeswararao & Srinivas, 2015).

Metal dispersion values for 5 wt.% Pt/γ-Al_2O_3 catalysts, determined from mean particle sizes (m), have been reported: m = 4.8 nm, with metal dispersion of 8.1% for Pt (5 wt.%)/Al_2O_3 (7.4%) (Bhogeswararao & Srinivas, 2015).

2.7.7. Thermogravimetric analysis

The use of a TGA is paramount in characterising Pt/γ-Al_2O_3 catalysts—it enables the determination of both their composition and thermal stability. Through TGA analysis, the thermal decomposition behaviour of the catalyst can be elucidated, providing critical insights into its structural integrity and potential degradation pathways.

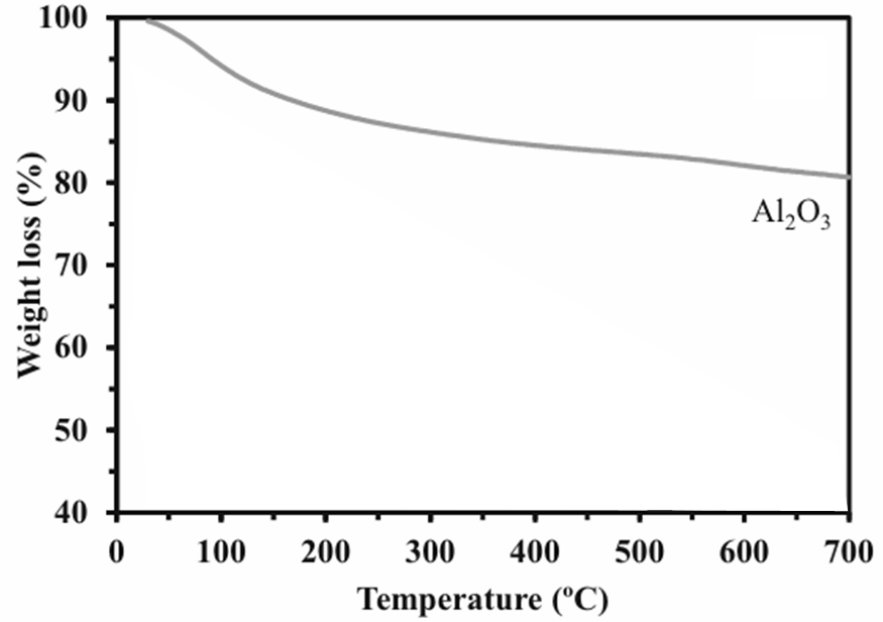

Figure 2.14. Typical TGA profile for mesoporous Al_2O_3 (Mostafa *et al.*, 2019).

2.7.8. X-ray powder diffraction

In the catalyst characterisation of Pt/Al_2O_3, XRD emerges as a crucial technique offering comprehensive insight into the crystalline structure of a catalyst. Through XRD, the shape and size of Pt NPs can be assessed, providing crucial details about the catalyst morphology. Additionally, XRD enables the detection of phase changes, facilitating the observation of reduction or oxidation processes within the catalyst. Moreover, this technique allows for a comprehensive structural analysis, elucidating lattice parameters and giving structural information vital for understanding the catalyst's performance and behaviour. Figure 2.15 shows the XRD patterns of 5 wt.% Pt/γ-Al_2O_3 and Al_2O_3. XRD confirms the structural integrity of the support and effective deposition of Pt NPs. The Al_2O_3, gamma-phase structure, has peaks at (220), (311), (222), (400) and (440), confirming its gamma-phase structure (Bhogeswararao & Srinivas, 2015). Figure 2.15 shows additional peaks appearing with the addition of Pt, indicating the formation of crystalline Pt NPs on the alumina surface. An average crystallite size of 29.5 nm for XRD performed on 5 wt.% Pt/γ-Al_2O_3 was reported

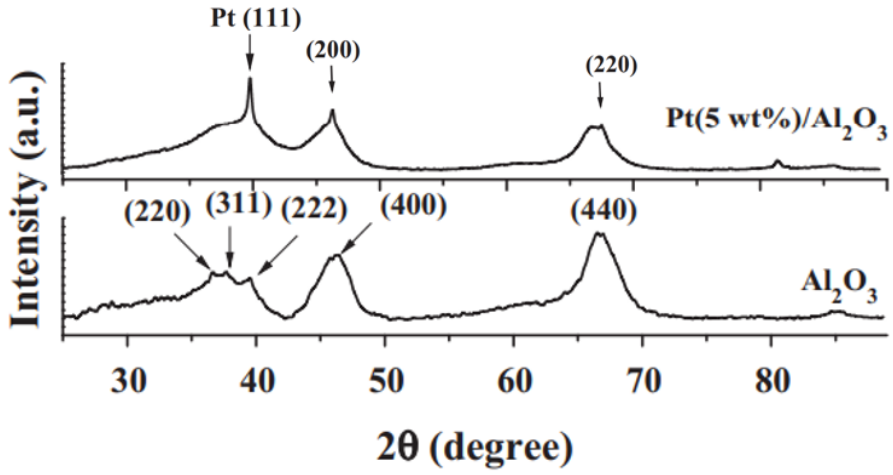

Figure 2.15. XRD patterns of 5 wt.% Pt/γ-Al_2O_3 and Al_2O_3 with the peaks corresponding to both the metal and the support clearly identified (Bhogeswararao & Srinivas, 2015).

2.8 LOHC Analysis

LOHC characterisation provides valuable insight to key parameters throughout the dehydrogenation reaction. GC-MS with single quadrupole detection (GC-MS-SQ) was first proposed by Modisha *et al.* and remains essential for accurately determining conversion rates, reaction selectivity and by-product formation, by separating overlapping intermediates and isomers (Modisha *et al.*, 2018). GC-MS-SQ distinguishes between isomers on the basis of their volatility and mass, which is crucial for accurately determining the degree of hydrogenation (DOH) in mixtures of partially hydrogenated species. It also provides quantitative analysis by using calibration standards, allowing for the reliable quantification of specific isomer fractions (Modisha *et al.*, 2018).

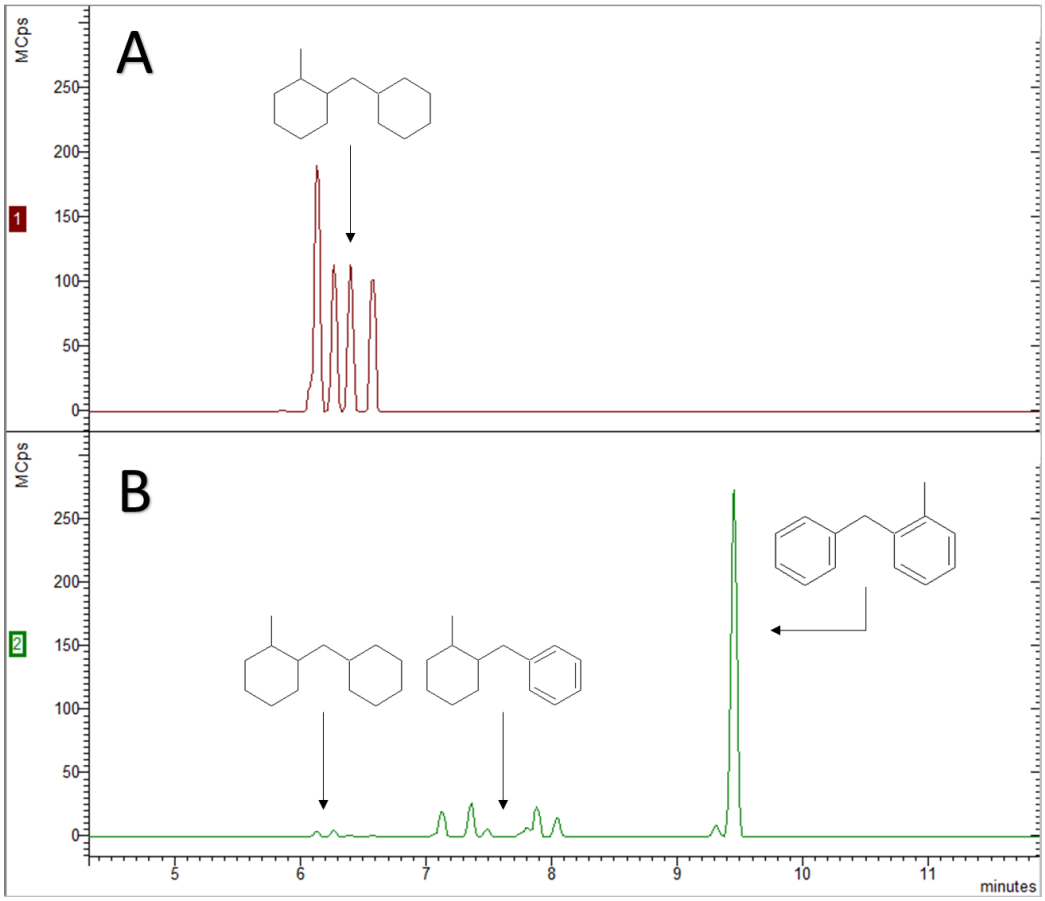

Figure 2.16. GC-SQ-MS chromatogram showing (A) H12-BT before reaction and (B) product distribution after 4 h of the dehydrogenation reaction (Ford *et al.*, 2024).

The DOD is calculated according to

$$\text{DoD}_{\text{Liquid}}(\%) = \frac{VH_2\ released}{VH_2\ max} \times 100 \quad \ldots(2.2)$$

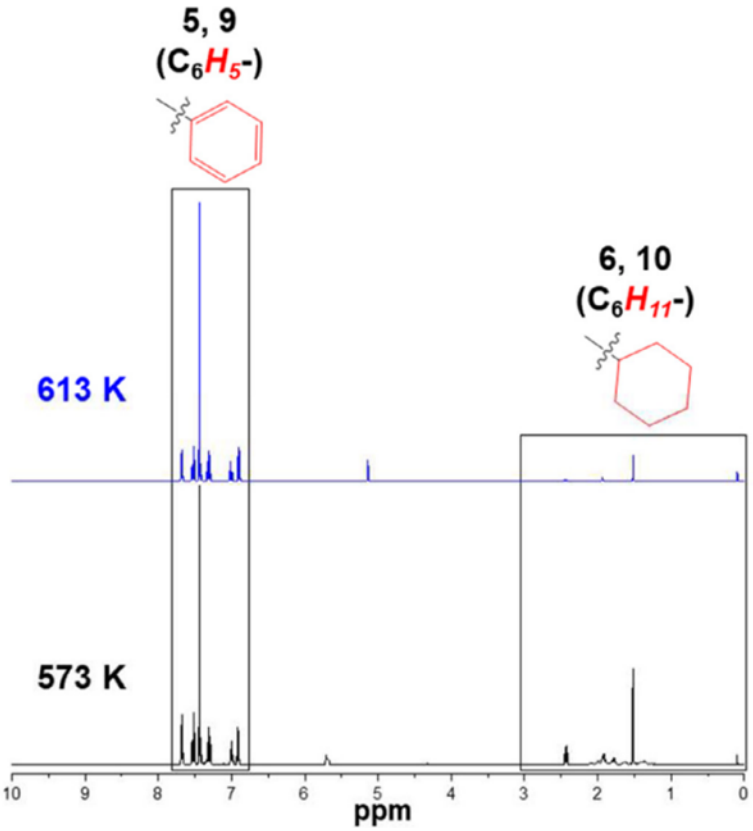

Figure 2.17. ^{1}H NMR spectra ($CDCl_3$) after dehydrogenation of bicylohexyl ether and dicyclohexyl ether (Jang *et al.*, 2020).

Beyond GC-MS, proton nuclear magnetic resonance (^{1}H NMR) spectroscopy is a widely used analytical technique to determine the DOH in organic compounds such as LOHCs. It offers advantages such as high resolution, quantitative analysis, sensitivity to hydrogenation, structural information, non-destructiveness and versatile application across various fields. Jang *et al*. used ^{1}H NMR spectroscopy to analyse hydrogenation/dehydrogenation processes and molecular structural changes in biphenyl and diphenyl ether systems (Figure 2.18) with further confirmation by GC-MS (Jang *et al.*, 2020). A disdvantage to this technique is that ^{1}H NMR is limited to hydrogen atoms, and the presence of multiple overlapping signals can complicate spectra and make it challenging to distinguish between different components. When using this technique, considerations such as solvent interference, sample homogeneity and overlapping signals must be made to ensure accurate results (Jang *et al.*, 2020).

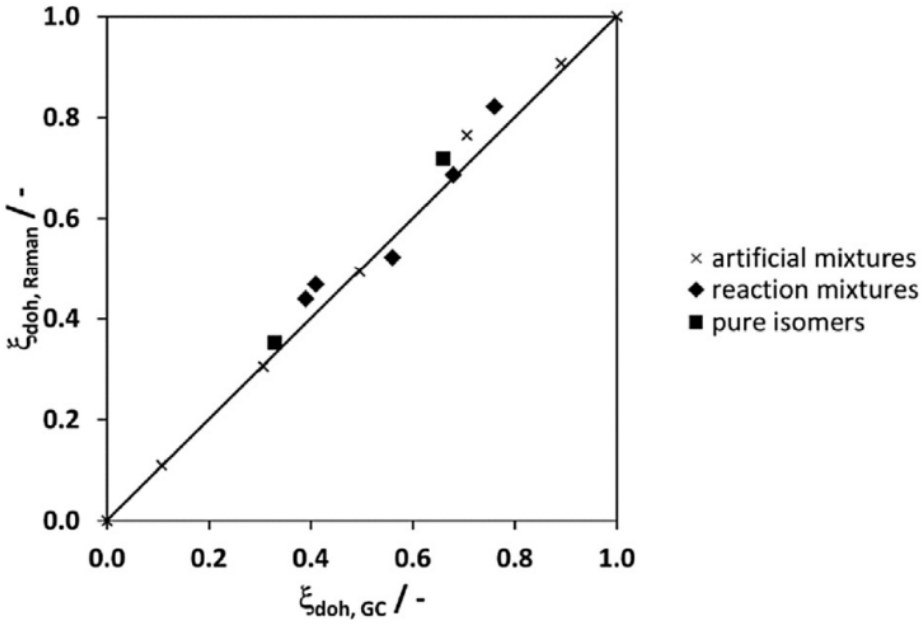

Figure 2.18. DOD, determined using Raman spectroscopy, over the DOH, measured with GC-MS for DBT (Müller *et al.*, 2016).

Yet another technique used to determine the DOD of LOHCs is Raman spectoscopy, which offers high sensitivity, rapid analysis and minimal sample preparation (similar to GC-MS). Both pure and partially hydrogenated isomers for H6-DBT and H12-DBT are able to be measured using these techniques: see Figure 2.19 (Müller *et al.*, 2016). However, it can also cause spectral overlap (due to multiple species), which is difficult to deconvolute and then accurately assess the individual contributions of partially and fully hydrogenated forms. There is also fluorescence interference, which obscures the Raman signal and inhibits data interpretationMüller *et al.*, 2016)(Müller *et al.*, 2016)(Müller *et al.*, 2016)(Müller *et al.*, 2016)(Müller *et al.*, 2016)(Müller *et al.*, 2016)(Müller *et al.*, 2016). While Raman spectroscopy offers a powerful method, it is generally less sensitive to trace compounds, and larger sample sizes or longer acquisition times may be required to achieve similar sensitivity levels to GC-MS (Müller *et al.*, 2016).

The literature gaps observed in catalyst characterisation and BT LOHC anaylsis are identified to be kinetic studies on inductive heating. In this study, investigations will be carried out, using GC-MS, to determine the effect of polymer binders in the catalyst slurry, and this will be supported by in-depth SEM analysis on the physical surface of the catalyst shell. Cycling tests of catalyst-coated SS pellets in dehydrogenation will also be investigated (to date there is limited research reported on this aspect).

2.9 Gaps in the Literature

Research on inductive heating in dehydrogenation processes, particularly in LOHC systems, has shown the potential to reduce heating rates and reduce heat losses to the environment, while allowing fast hydrogen release (Schörner *et al.*, 2024). Studies have also been conducted on inductive heating incorporation to resolve the temperature shortfall achieved by conventional heating during dehydrogenation (Hart *et al.*, 2020a). Higher conversion and hydrogen release can be achieved when inductive heating is used over conventional heating (Hart *et al.*, 2020a). In particular, the use of metal spheres for inductive heating has shown significant promise in reducing heating loss and improving the heating rate for dehydrogenation (Hart *et al.*, 2020a). Limited kinetic studies have been carried out the use of eggshell catalysts in catalytic dehydrogenation (Peters *et al.*, 2015), as well as the binders used in the slurry for catalyst coating (Falamaki *et al.*, 2006).

Both the advantages and disadvantages associated with the inductive heating method, along with the gaps in the existing knowledge base, have been identified. Research on the specific application of inductive heating for the dehydrogenation of H12-BT using Pt/γ-Al_2O_3 coated SS pellets as inductively active catalysts is limited. The present study will therefore examine the role of eggshell catalysts in improving catalytic efficiency during inductive heating, offering advantages such as increased surface area, reduced diffusion resistance and enhanced mass transfer (Peters *et al.*, 2015). Kinetic studies will be performed, using GC-MS, on coating thickness to assess the activation energy and mass transfer limitations associated with eggshell catalysts. Results will be compared to conventional electrical heating in efforts to assess the advantages and disadvantages of the two methods.

Following on from the gaps identified in literature, a further objective will be to determine the effect of catalyst shell thickness on mass transfer limitations during the dehydrogenation of H12-BT by preparing inductively active catalysts of varying shell thickness of Pt/γ-Al_2O_3 on SS pellets using a dip-coating method. The effect of polymer binders on coating uniformity and catalytic performance will also be investigated.

3. Chapter 3: Material and Methods

This chapter provides a description of all materials and methods used in this study, to achieve the objectives outlined in Chapter 1. It includes all chemicals used, the catalyst synthesis procedures, details of characterisation techniques and experimental setups used for evaluation of catalyst performance in the dehydrogenation of H12-BT.

3.1 Materials

The SS pellets (diameter 5 mm) were sourced from Guerrilla (South Africa). Nitric acid (55%) was obtained from Ace Chemicals (Johannesburg, South Africa). Alumina (γ-Al_2O_3) extrudates were acquired from Clariant International Ltd. (USA). Polyvinyl alcohol (PVA), with molecular weights of 22000 and 89000–98000 g/mol, was supplied by VWR Chemicals (Leuven, Belgium) and Sigma-Aldrich (USA), respectively. Polyvinylpyrrolidone (PVP), with molecular weights of 55000 and 360000 g/mol, was supplied by Sigma-Aldrich (USA). H12-BT(99% DOH) was produced in-house using the hydrogenation of BTBT (99% purity; Sasol (Marl, Germany)). A Pt sponge (Implats; Johannesburg, South Africa) was used to synthesise hexachloroplatinic acid ($H_2PtCl_6 \cdot 6H_2O$, ~38% Pt basis). The gases N_2 (99.999%) and H_2 (99.999%) were procured from Afrox (Johannesburg, South Africa) and utilised for catalyst processing. Liquid nitrogen used in the BET analysis procedure was obtained from the Zoology Department at Potchefstroom Campus, NWU (South Africa).

Note that hereafter, for simplicity, the following designations are used for polymer binders: PVA22000, PVA89000–98000; PVP55000, PVP360000.

3.2 Methods

3.2.1 Catalyst preparation

The wet impregnation method was used to synthesise Pt/γ-Al_2O_3 catalysts with Pt metal loadings ranging from 0.3 to 8 wt.%. A Pt precursor solution for each desired metal loading was prepared by dissolving an appropriate amount of hexachloroplatinic acid crystals in Milli-Q water, as shown in Figure 3.1. Equations 3.1 and 3.2 were used to calculate the required masses of $H_2PtCl_6 \cdot 6H_2O$ and γ-Al_2O_3 support for the preparation of Pt/γ-Al_2O_3 with targeted metal loadings (0.3–8 wt.%).

$$\frac{M_{Pt(g)} \times n_{Pt(g)}}{m_{Al_2O_3(g)} + (M_{PtO_2(g)} \times n_{Pt(g)})} = \frac{\text{Pt loading desired(wt.\%)}}{100} \quad \ldots(3.1)$$

$$m_{H_2PtCl_6(g)} = n_{H_2PtCl_6(g)} \times M_{H_2PtCl_6(g)} \quad \ldots(3.2)$$

This equation accounts for the formation of platinum oxide (PtO_2) on the surface of the catalyst during the reduction of Pt/γ-Al_2O_3 samples. The dominant platinum oxide product develops on the surface of the catalyst when the calcination temperature is 300 °C (Hwang & Yeh, 1996).

An example of the calculation to prepare 8 wt.% Pt/γ-Al_2O_3 (25 g) is as follows:

$$\frac{195.08 \times n_{Pt(g)}}{25g + (227.08 \times n_{Pt(g)})} = \frac{8}{100}$$

$$195.08 \times n_{Pt(g)} = 2 + 18.1664 n_{Pt(g)}$$

$$176.9136 \times n_{Pt(g)} = 2$$

$$n_{Pt(g)} = 0.01131 mol$$

$$m_{H_2PtCl_6(g)} = n_{H_2PtCl_6(g)} \times M_{H_2PtCl_6(g)}$$

$$m_{H_2PtCl_6(g)} = 0.01131\ mol \times 517 g$$

$$m_{H_2PtCl_6(g)} = 5.8.4727\ g$$

From the above then, 5.31365 g H_2PtCl_6 was dissolved in 100 mL Milli-Q water with 25 g Al_2O_3, and the solution mixed with the Al_2O_3 pellets then left to settle. The pellets were impregnated, using the following experimental conditions: a Büchi Rotavapor® R-300 with a heating bath set at 60 °C, a vacuum pressure of 50 mbar and a rotating speed of 40 rpm, with continuous stirring for 90 min. The pellets were first dried in air and then dried at 120 °C for 4 h in an Espec oven (model SU-221). After wet impregnation, the Pt/γ-Al_2O_3 pellets were calcined in a tube furnace under constant air flow at 350 °C for 3.5 h (heating rate 5 °C/min. The calcined Pt/γ-Al_2O_3 pellets were then reduced in a tube furnace under a constant gas flow of 10% H_2/N_2 at 400 °C for 4 h (heating rate 5 °C/min). Figure 3.1 shows a schematic of the experimental procedure followed during the preparation of the Pt/γ-Al_2O_3 catalysts.

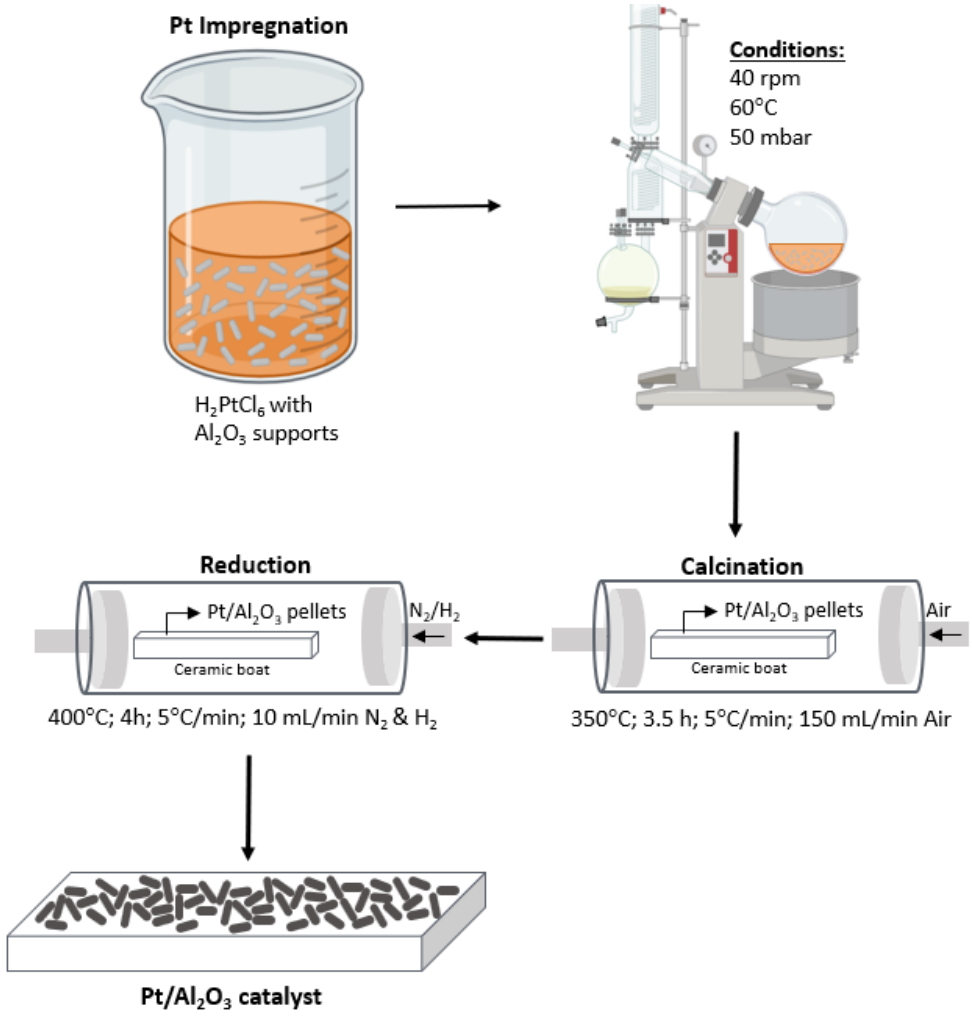

Figure 3.1. Schematic representation demonstrating the preparation of Pt/γ-Al_2O_3 catalyst using the wet impregnation method.

3.2.2 Preparation of catalyst-coated SS pellets using the dip coating method

To prepare the catalyst-coated SS pellets, the spherical SS pellets were etched using 5 M nitric acid solution to improve surface roughness for better adhesion of the catalyst (see Figure 3.3). Binder solutions were prepared by dissolving the PVPs and PVAs (of the different molecular weights mentioned) in Milli-Q water, to achieve the following concentrations: 0.25, 0.5, 0.75 and 1 wt.%. A slurry was prepared by mixing grounded Pt/γ-Al_2O_3 and the binder solution. Pre-treated SS pellets were dip coated in the slurry, followed by drying, until the desired coating was obtained. Figure 3.3 shows the SS pellets: untreated, etched in acid, coated with Pt/γ-Al_2O_3 and coated with Pt/γ-Al_2O_3 after dehydrogenation.

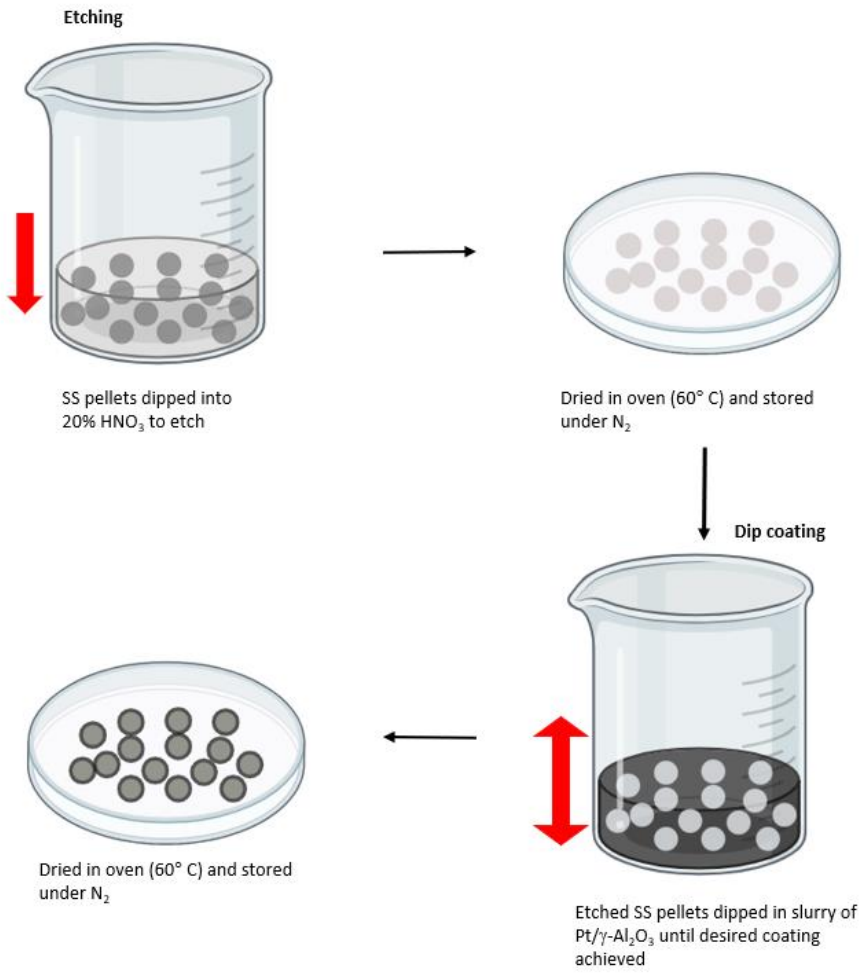

Figure 3.2. Schematic diagram demonstrating the dip-coating method used for preparation of Pt/γ-Al_2O_3 coated SS pellets.

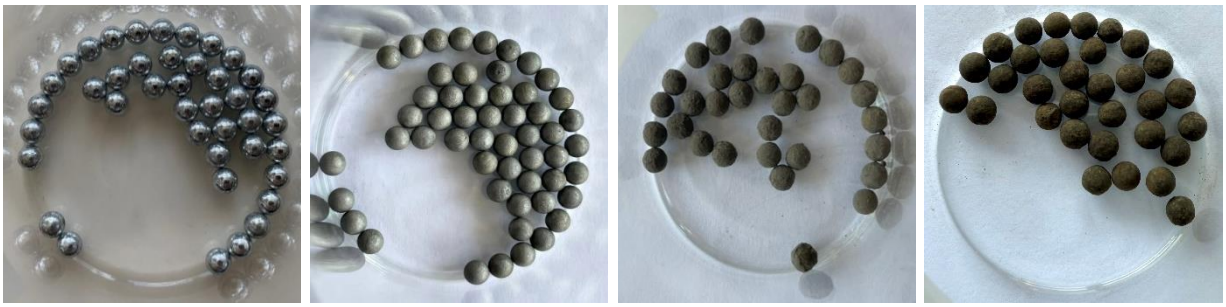

Figure 3.3. Left to right: Untreated SS pellets (4.5 mm), SS pellets etched with 5 M nitric acid, coated with Pt/γ-Al_2O_3, and Pt/γ-Al_2O_3 coated SS pellets after dehydrogenation.

3.3 Catalyst Characterisation

The various analytical techniques used to evaluate the physicochemical properties of the catalysts, including their structural, morphological, and compositional characteristics, are now described.

Specifications of the analytical equipment used to characterise the catalysts used in this study and the experimental details that pertain are included.

3.3.1. Inductively coupled plasma–optical emission spectroscopy

The Pt concentrations in the catalysts were measured using an Agilent 5110 ICP-OES instrument (Agilent, USA) coupled with ICP Expert software. First, Pt/γ-Al_2O_3 (~1 g) was digested under reflux in a 1:10 mixture of H_2O_2: HCl at 80 °C for 6 h. The samples were filtered, and the Pt content was analysed. ICP-OES was used to quantify the platinum loading on the γ-Al_2O_3 support accurately.

3.3.2. Brunauer–Emmett–Teller

The textural properties of the catalyst, including surface area, pore volume and pore diameter, were analysed using a Microtrac Belsorp Mini X instrument (Japan), and data processing was performed through Belmaster software. The sample tube was loaded with ~0.1g of g Pt/γ-Al_2O_3 then purged with N_2 and degassed at 300 °C for 1 h under 1 kPa. N_2 adsorption/desorption isotherms were then measured at 77.35K. BET was done to determine changes in surface area and porosity of the catalysts with varying Pt loadings.

3.3.3. CO pulse chemisorption

CO pulse chemisorption was conducted using a Belcat II catalyst analyser (Microtrac Belcorp, Japan) equipped with a Thermal conductivity detector (TCD) and a H_2O trap. The quartz triple-sample U-tube was loaded with 100 mg γ-Pt/γ-Al_2O_3 catalyst. The pulse injection method included a pretreatment procedure performed in eight steps, involving oxidation and reduction at a target temperature of 400 °C, using He as the carrier gas. Measurement of CO pulse injection was performed at 50 °C (TCD at 120 °C, 10% CO/He); 10 pulse injections were performed, and results of the last three were taken to determine the adsorption equilibrium. BELControl software was used to analyse the data. This technique was used to quantify the number of active platinum sites on the catalyst surface by measuring CO adsorption as well as the metal dispersion and availability of catalytic sites.

3.3.4. Hydrogen temperature-programmed reduction

H_2-TPR was carried out on a Belcat II catalyst analyser equipped with a TCD. The catalyst samples used for TPR studies were calcined as described earlier (Section 3.2.1). The quartz triple-sample U-tube was loaded with 100 mg Pt/γ-Al_2O_3 catalyst (0.3–8 wt.%), taking the γ-Al_2O_3 support as a baseline. Temperature-programmed analysis was conducted using a TCD detector stabilised for 30 min at 120 °C. Samples were pre-treated under a mixture of H_2 and Ar; the temperature ramped to a target of 950 °C at 10 °C/min. The carrier gas was 1:10 H_2: Ar. BELControl software was used to

analyse the data, with plotting in Excel. Analysis of the temperature at which reduction occurs it provides insight into catalyst stability and metal-support interactions.

3.3.5. Scanning electron microscopy–energy dispersive X-ray spectroscopy

SEM analysis was performed using an FEI Quanta FEG 250 field emission gun scanning emission microscope with xT microscope Server and Control software (Thermo Fischer Scientific, Czech Republic). EDS was carried out with Aztec software and an X-Max SDD 20mm² detector (Oxford Instruments Inc., United Kingdoms) for elemental analysis. The Pt/γ-Al_2O_3 catalyst-coated SS pellets were fixed on the sample holder using carbon tape. EDS was used to analyse the uniformity of the Pt/γ-Al_2O_3 coating on the SS pellets, as well as the elemental composition of the surface of the SS pellets.

3.3.6. High-resolution transmission electron microscopy

The particle size distribution was determined using a JEOL-JEM 2100 transmission electron microscope at 200 kV (Thermo Fisher Scientific, USA). Each Pt/γ-Al_2O_3 pellet catalyst was ground and the powder samples then dispersed in ethanol to form a suspension that was sonicated for 30 min at 40 °C. The samples were then dropped onto carbon-coated copper grids and the Pt NPs were analysed. The particle size distribution of the NPs was determined by measuring the diameter of 300 particles, using Image J.

3.3.7. Thermogravimetric analysis

TGA was performed using a TA Instruments Q500 analyser (USA) equipped with an Evolved Gas analysis (EGA) furnace. A sample weighing 15 mg was placed on a platinum pan and heated from room temperature to 1000 °C at a ramp rate of 10 °C/min. During the analysis, nitrogen gas (flow 10 mL/min) was used as the balance gas and air (flow 90 mL/min) as the sample gas. TGA was employed to study the thermal decomposition profiles of the polymeric binders, PVA and PVP, used in catalyst preparation.

3.3.8. X-ray power diffraction

XRD was carried out using a PANalytical X'Pert Pro instrument (UK) to identify and quantify the crystalline phases of the catalysts and support material. The samples were placed in a back-loaded sample holder and mounted on a spinner stage within the instrument. A cobalt X-ray tube generates X-rays that pass through an iron filter before being directed at the sample. A sample-specific diffractogram id generated, then detected by an X'Celerator detector (45 kV and 40 mA). Within the diffractogram, the peak positions indicate the distinct crystalline phases, while their relative

abundance is determined by the peak intensities. X'Pert Highscore Plus software and the International Centre for Diffraction Data (ICDD) PDF 4+ database was used to identity the crystalline phases present in the Pt/γ-Al_2O_3 catalysts and to assess the crystallite size and structural changes resulting from different Pt loadings.

3.4 Dehydrogenation Activity Evaluation

3.4.1 Electrical heating: Dehydrogenation

The conventional dehydrogenation of H12-BT was conducted on a laboratory-scale 100 mL glass batch-type reactor. The experimental setup comprised a three-neck round bottom flask connected to a condenser maintained at 10 °C and equipped with two thermocouples to monitor the bulk reaction temperature. The Pt/γ-Al_2O_3 coated SS pellets were placed inside the reactor with a volume 10 mL of H12-BT (99% DoH) and the system was purged with N_2. The reactants were heated to 260 °C using a heating mantle equipped with a Wiggens PL524 Pro temperature controller (China). The condenser temperature was regulated at 10 °C using a cryostat (Julabo Labortechnik GmbH, Germany). The H_2 flow rate was measured using a Bronkhorst mass flow meter (EL-Flow F11B-500-AGD-22V), max flow rate 500 mL/min, which was logged using Labview software. The experimental setup of a conventional heating batch dehydrogenation is shown in Figure 3.4.

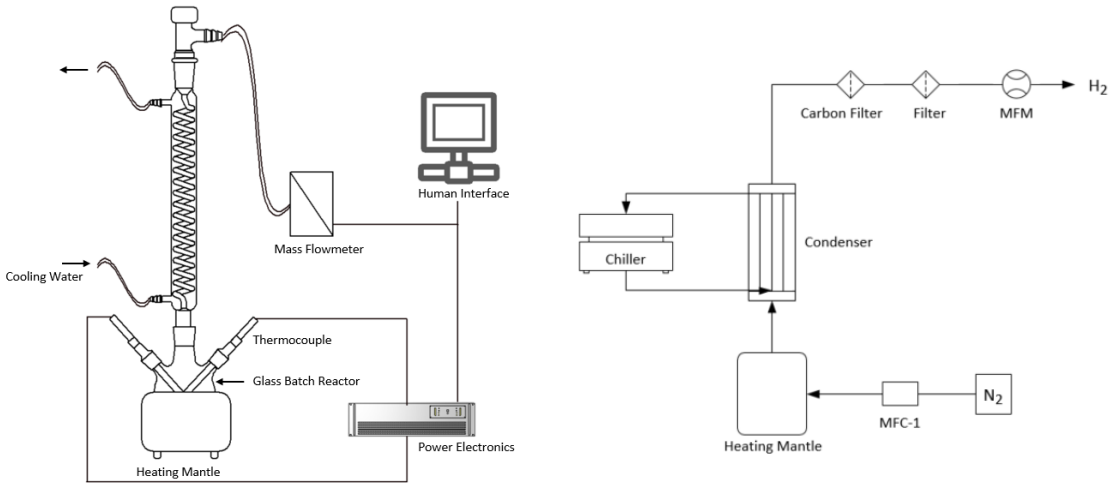

Figure 3.4. Left: Experimental setup of a conventional electrical heated batch-type reactor for the catalytic dehydrogenation. Right: PID of the conventionally heated batch reactor setup.

3.4.2 Inductive heating: Experimental setup

The inductive heating setup for the dehydrogenation of H12-BT includes a chiller, a subsystem panel,

and a human interface, connected to a Raspberry Pi IO Board for parameter adjustment and data recording. A 50 mL glass reactor filled with coated and uncoated SS spheres is placed inside the inductive coil as shown in Figure 3.5. This facilitates heating through eddy currents induced by the AC magnetic field generated by the heating coil. The panel also features a thermocouple for measuring the temperature, a cooling condenser, and a mass flow meter (Bronkhorst EL-FLOW Select F-111B). The back panel of the system includes a 250 W power supply that converts 220 V AC to 12 V DC to power the IO board and an inductive heater.

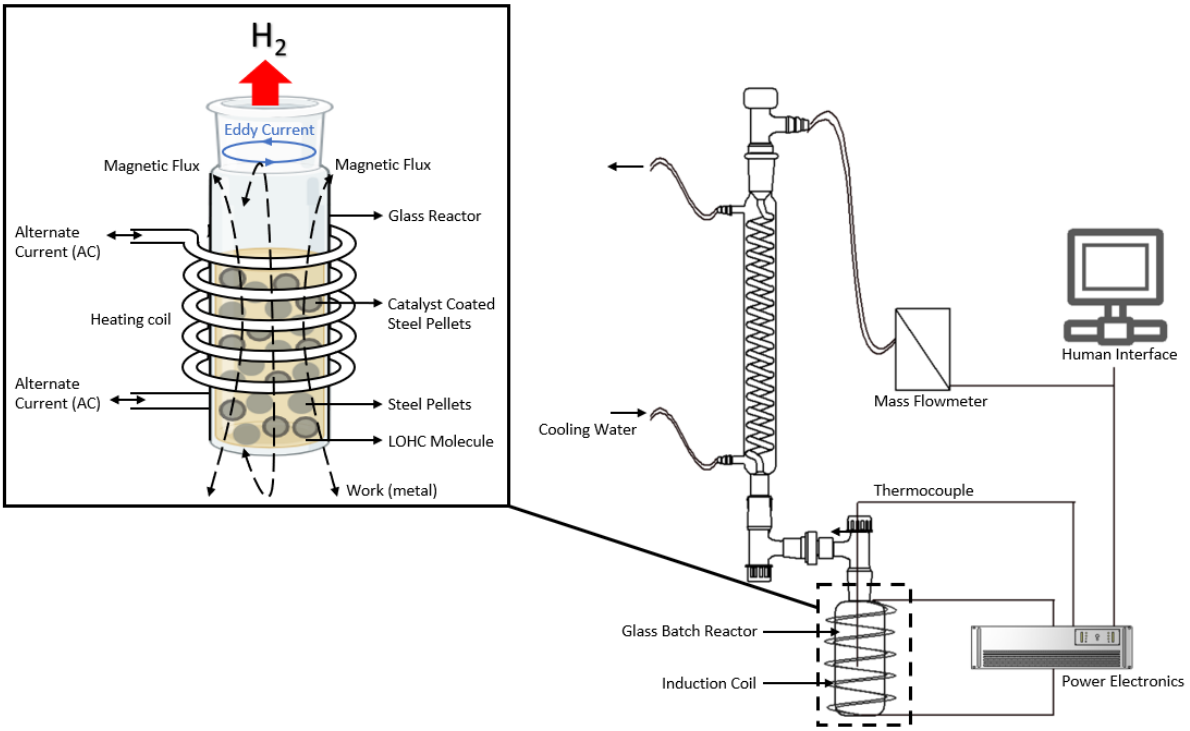

Figure 3.5. Experimental setup of an inductively heated batch-type reactor for the catalytic dehydrogenation of H12-BT.

3.4.3 Inductive heating: Dehydrogenation performance

Each test involved filling the glass batch reactor with 10 mL of H12-BT (99% DoH) and packing it with a mixture of SS and catalyst pellets. A thermocouple was placed in the centre of the reactor, while the hydrogen flow was precisely regulated using a mass flow meter. The experiments explored three reactor packing configurations: pure uncoated SS pellets as a baseline, uncoated SS pellets combined with Pt/γ-Al_2O_3 catalyst pellets, and Pt/γ-Al_2O_3 catalyst-coated SS pellets alongside uncoated SS pellets. See Figure 3.6. Different metal loadings of Pt/γ-Al_2O_3 (0.3, 1, 3, 5, 8 wt.%) were tested to identify the effect of loading in the dehydrogenation of H12-BT when using the inductive heating method. The catalyst performance was investigated using different binders *(*PVA 22 000, PVA 89 000, PVP 55 000

and PVP 360 000). Coatings of various thicknesses on the SS pellets were applied. The performance of these configurations was evaluated across a range of temperatures (225 °C, 235 °C, 245 °C, 255 °C, 260 °C) to identify optimal reaction conditions. Kinetic determinations were also carried out to determine the activation energy for each configuration. Results of *t*hese variations could be useful to elucidate the impact of catalyst composition and coating on the dehydrogenation process during inductive heating.

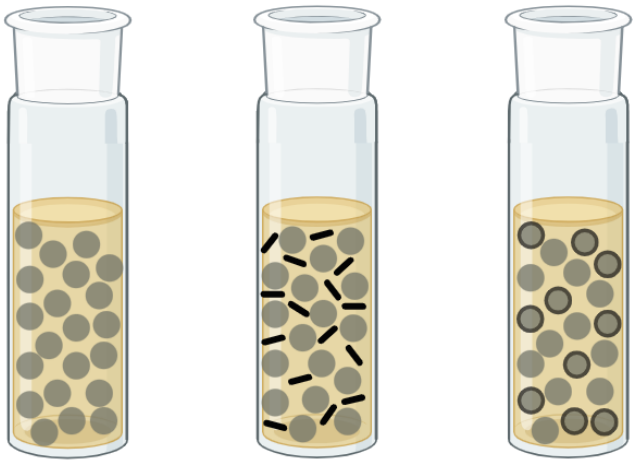

Figure 3.6. Illustration of vials with BT as the LOHC: a) untreated SS pellets, b) untreated SS pellets and Pt/γ-Al_2O_3 catalyst pellets and c) mixture of catalyst-coated SS pellets and untreated SS pellets.

3.5 Liquid and Gas Analysis

LOHC molecules were analysed with GC-MS, using a single quadrupole mass spectrometer (5977C GC-MSD; Agilent, USA). The equipment included a 7693A automatic liquid sampler, a HP-5 ms Ultra Inert column (30 m length, 0.25 mm internal diameter, 0.25 µm film thickness). High-purity helium (99.999%) was used as the carrier gas at a flow rate of 1 mL/min. The reaction mixture was extracted and diluted with hexane at 1:100 wt. ratio; 1 µL aliquots were injected at a split ratio of 1:100. The injector was maintained at 250 °C, while the oven temperature was increased from 50 °C (held for 10 min) to 150 °C (rate 25 °C/min) and then to 300 °C (rate 10 °C/min), then held for 10 min. The transfer line and source were maintained at 280 °C and 230 °C, respectively, with an electron energy of 70 eV.

For the gas phase analysis, determination of H_2 purity was performed using a gas chromatograph (SRI-8610C GC, USA) equipped with a 0.9 m molecular sieve column and a TCD. Gas samples were collected during dehydrogenation experiments using 1 L sampling bags (Restek, USA). The GC instrument was calibrated to quantify gases such as H_2, CO, CO_2 and CH_4. Argon was used as a carrier gas. PeakSimple analysis software was used to analyse the data obtained.

4. Chapter 4: Results and Discussion

4.1 Catalyst Synthesis and Characterisation

Results and discussion pertaining to the synthesis and characterisation of the catalysts used in the inductive heating process for H12-BT dehydrogenation are now described. SS pellets were dip coated after the catalysts were synthesised, using the wet impregnation method: Pt loadings of the catalysts used were 0.3 wt.% to 8 wt.%. Structural and functional properties were determined using various characterization techniques: BET, CO pulse chemisorption, SEM-EDS, TEM, XRD, TGA and H_2-TPR. The catalysts were then applied to the dehydrogenation process and their resulting performances evaluated in terms of hydrogen productivity (hydrogen production), conversion rates and stability.

4.1.1 Inductively coupled plasma–optical emission spectroscopy

The Pt/Al_2O_3 catalysts with targeted loadings of 0.3, 1, 3, 5 and 8 wt.% were synthesised by the wet impregnation method (addressed in Chapter 3). Accurate Pt metal loadings of all $Pt/\gamma\text{-}Al_2O_3$ catalysts. were confirmed using ICP-OES. Despite minor variations, the results demonstrated that the actual Pt loadings closely matched the desired target values. The variations recorded, which demonstrate the precision and repeatability of the catalyst preparation process, were considered acceptable. The catalyst with a target Pt loading of 0.3 wt.% had an actual loading of 0.35 wt.%, whereas the catalyst with a loading of 1 wt.% had a measured loading of 1.17 wt.%. The slight positive deviations imply a marginally higher metal deposition efficiency, which could be caused by Pt retention-affecting factors, such as the impregnation technique precursor concentration or the drying and calcination conditions. Pt NP size affects the performance of the catalyst. Unmodified Pt NPs exhibit maximum hydrogen production at sizes 1.95–2.70 nm, whereas the undesirable high-boiler formation occurs at 1.5 nm (Auer *et al.*, 2020).

With variations in metal loadings ranging from +1.67% to +17%, the ICP-OES results demonstrated that the actual Pt loadings are consistently higher than the desired values (Table 4.1). This positive deviation suggests that Pt is slightly overloaded on the support. Although excessive loading may also result in metal particle agglomeration, which would impair metal dispersion and overall catalytic efficiency, higher metal loadings could affect catalyst performance by possibly increasing the number of active sites available for reaction.

Table 4.1. Metal loading on Pt/Al_2O_3 determined using ICP-OES.

Catalyst	Target Pt (wt.%)	Actual loading (wt.%)	Deviation (%)
Pt/Al_2O_3	0.3	0.35	+16.67
	1	1.17	+17.00
	3	3.05	+1.67
	5	5.36	+7.20
	8	8.64	+8.00

4.1.2 Brunauer–Emmett–Teller

The N_2 adsorption/desorption isotherms (Figure 4.1) and the matching pore size distributions (Figure 4.2) of various $Pt/\gamma\text{-}Al_2O_3$ catalysts (various wt.% values) and the support all displayed Type IV isotherms with H1 hysteresis loops, typical of mesoporous materials (Dabbagh *et al.*, 2011). This supports the existence of a narrow pore size distribution and well-ordered mesoporous structure, as observed in related investigations (Dabbagh *et al.*, 2011).

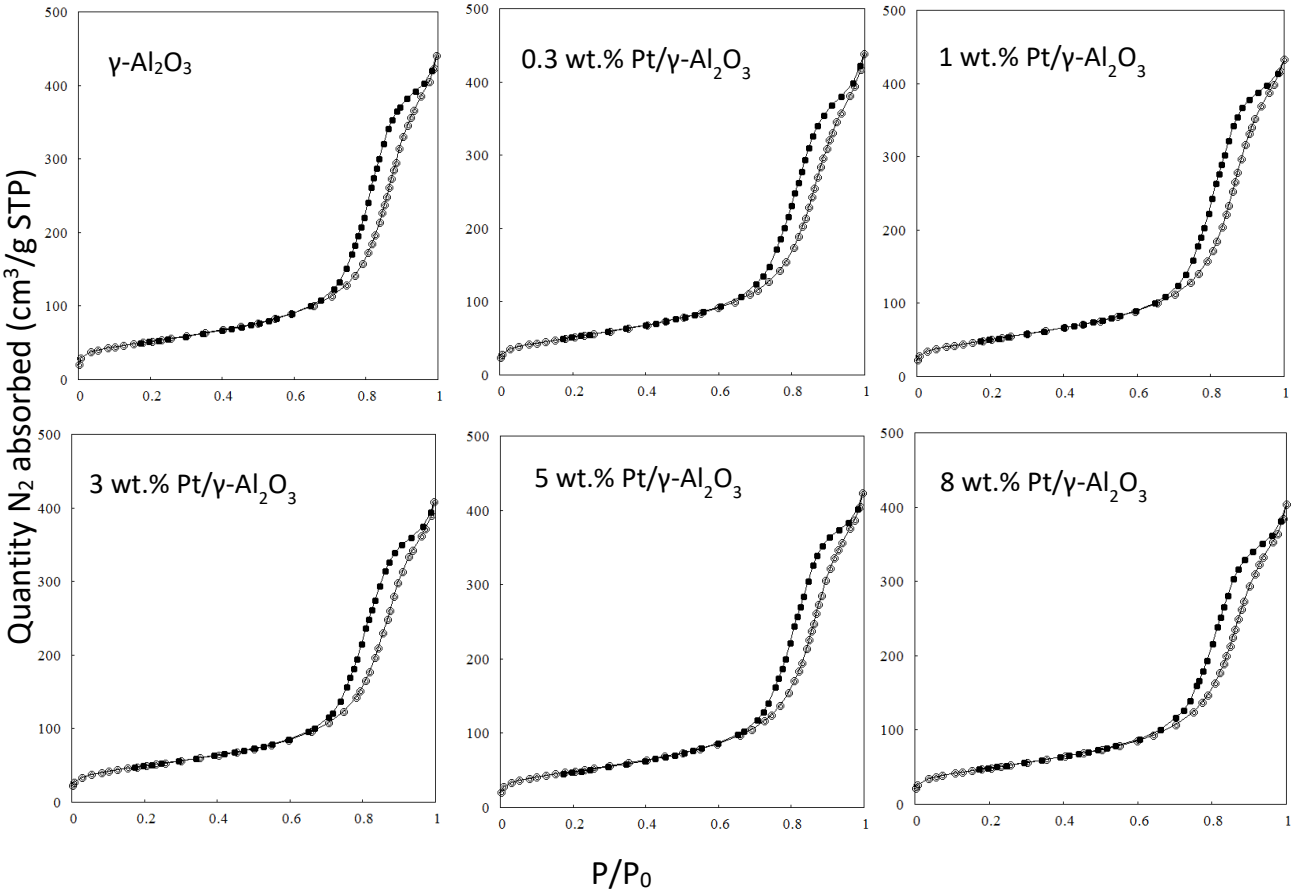

Figure 4.1. N_2 adsorption/desorption isotherms of various Pt/γ-Al_2O_3 catalysts and γ-Al_2O_3 support.

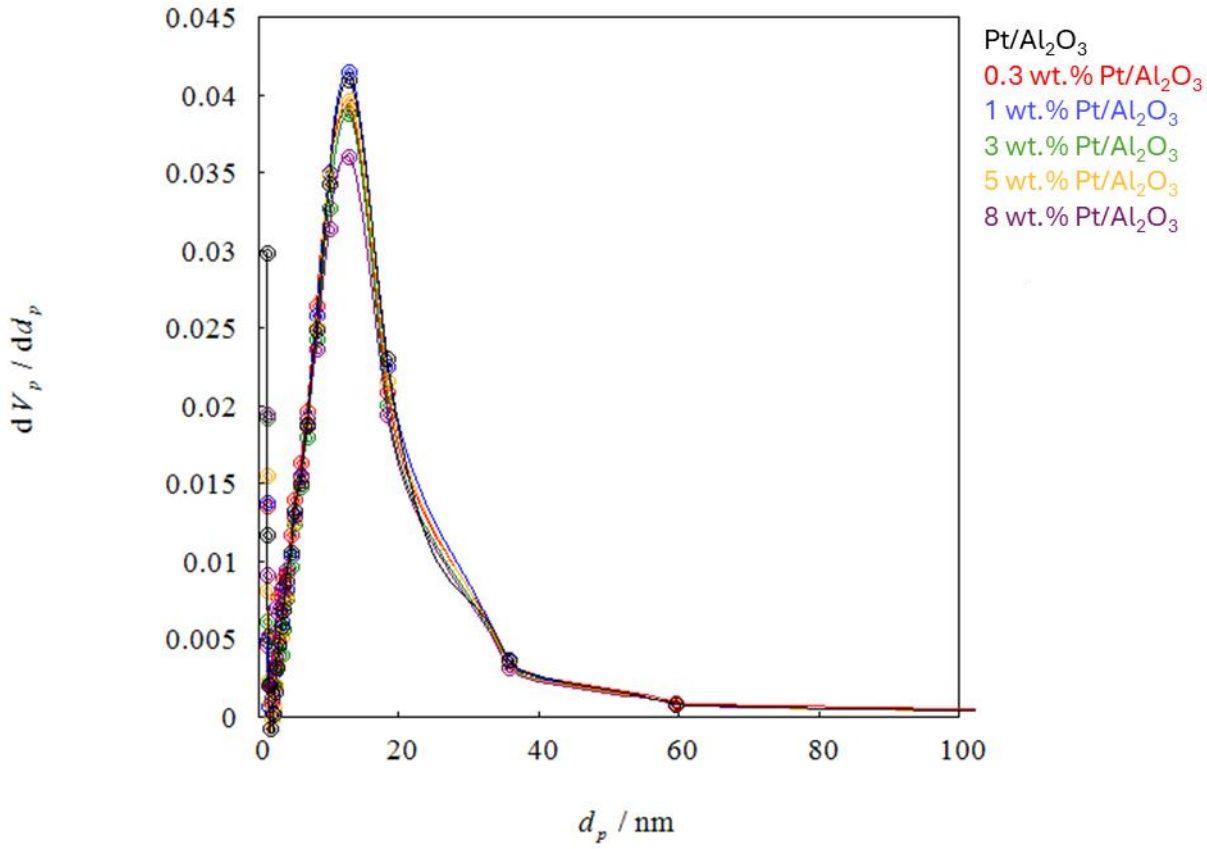

Figure 4.2. Pore size distributions of various Pt/γ-Al_2O_3 catalysts and γ-Al_2O_3 support.

The BET surface area, pore volume and pore size of γ-Al_2O_3 were 182.93 m^2/g, 0.0921 cm^3/g and 12.35 nm, respectively (Table 4.2). At 0.3 wt.%, the BET surface area initially increases slightly, indicating better Pt NP dispersion; however, it decreases as the Pt loading increases. This is due to partial pore blockage and metal particle agglomeration on the γ-Al_2O_3 support; the surface area available for nitrogen adsorption is decreased. This behaviour is in line with the findings of Lee *et al.,* i.e., at low Pt loadings (0.5–1 wt.%) there is high dispersion with no significant aggregation. At medium loadings (2–5 wt.%), the Pt clusters are mostly dispersed; however, there is a slight increase in metal aggregation. At high Pt loading (10 wt.%) there is noticeable aggregation of Pt clusters, where significant portions of Pt are in clusters >10 nm (Lee *et al.*, 2019). There are subtle changes in textural characteristics with increased Pt loading, starting with an increase in BET surface area at 0.3 wt.% and 1 wt.% Pt. However, as the Pt content increases to 3 wt.%, and higher, a progressive reduction in surface area and pore volume is noticeable as a result of Pt cluster-induced pore blockage. The 8 wt.% Pt/γ-Al_2O_3 shows the greatest reduction of catalyst, where the pore volume decreases to 0.0848 cm^3/g and the surface area decreases to 169.33 m^2/g. With only slight variations at ~12 nm, the pore size is comparatively constant in spite of the higher loading.

These results are in agreement with earlier studies showing that elevated Pt loadings may cause metal agglomeration which reduces the active site accessibility (Sabharwal & Secanell, 2022). As the catalyst loading increases, the pore size decreases from 0.3 wt.% (12.677 nm) to 8 wt.% (11.977 nm), which is a 5.52% decrease in pore size. Catalytic performance depends on a well-balanced pore structure because mass transport and diffusion during reactions are improved by an ideal pore size of ~24 nm (Auer *et al.*, 2020).

Table 4.2 Comparison of structural characteristics and particle sizes of Pt/γ-Al_2O_3 at various Pt loadings. N_2 adsorption–desorption measurements were used to determine the BET surface area pore volume and pore diameter. Data from CO chemisorption TEM.

Catalyst (Pt/γ-Al_2O_3)	**BET surface area (m^2/g)**	**Pore volume (cm^3/g)**	**Pore diameter (nm)**	**Metal dispersion % (Dm)**	**Metal surface area (m^2/g)**	**Particle size –CO (nm)**	**Particle size – XRD (nm)**	**Particle size – TEM (nm)**
γ-Al_2O_3	182.93	0.0921	12.350	-	-	-	-	-
0.3 wt.%	186.77	0.0931	12.677	65,64	162,1	1,73	0.706	1.114
1 wt.%	184.40	0.0919	12.632	59,58	147,1	1,90	2.814	3.281
3 wt.%	177.88	0.0887	12.340	50,78	125,4	2,23	1.437	2.582
5 wt.%	176.13	0.0879	12.746	42,09	103,93	2,69	2.971	3.214
8 wt.%	169.33	0.0848	11.977	35,34	87,3	3,21	3.348	4.513

4.1.3 CO pulse chemisorption

Catalyst samples, ranging from 0.3 to 8 wt.% Pt/γ-Al_2O_3 (~0.1 g), were analysed to determine the metal dispersion percentage, the metal surface area, and the particle size of the Pt/γ-Al_2O_3 catalysts.

A typical pulse chemisorption profile for CO adsorption on Pt/Al_2O_3 gives the detected CO concentrations on the y-axis and the adsorption time is expressed in seconds. Prior to breakthrough, the system is subjected to a series of CO pulses that interact with available Pt active sites, resulting in a series of peaks. The initial CO pulses showed reduced peak intensities, suggesting that there is significant adsorption onto the accessible Pt surface sites. Peak intensities increased with subsequent pulses as the system progressively approaches saturation due to the increase in adsorption sites. Peak height gradually increased because of fewer adsorption sites becoming available over time. By integrating the difference between the predicted and observed CO pulse areas prior to saturation, the total amount of chemisorbed CO could be determined. This information is essential for maximising catalyst performance in reactions involving hydrogenation oxidation and reforming, where catalytic activity and selectivity are determined by CO adsorption.

According to the CO pulse chemisorption results (Table 4.2), the metal dispersion, surface area and Pt particle size clearly show a trend as a function of the Pt loading. As the Pt wt.% increases from 0.3% to 8%, metal dispersion and metal surface area decrease, while particle size increases. Specifically, at 0.3 wt.%, the highest metal dispersion (65.64%) and largest surface area (162.1 m^2/g) are observed, with the smallest particle size (1.73 nm). As the loading increases from 0.3 wt.% to 8 wt.%, the metal surface areas decreases from 162.1 m^2/g to 87.3 m^2/g and the metal dispersion decrease from 65.64% to 35.34%, respectively. Simultaneously, the m increases from 1.73 nm to 3.21 nm, emphasising how higher Pt loading affects NP aggregation. This trend is observed in literature, where higher Pt loadings result in a lower dispersion of Pt NPs on the Al_2O_3 support due to increased aggregation (Araújo *et al.*, 2019). Araújo *et al* showed that lower Pt loadings increase catalytic activity due to well-dispersed Pt NPs. As the Pt loading increases to 1 wt.%, dispersion decreases; at 2 wt.% significant aggregation occurs, showing large Pt clusters and reduced dispersion, and affecting the catalytic performance (Araújo *et al.*, 2019).

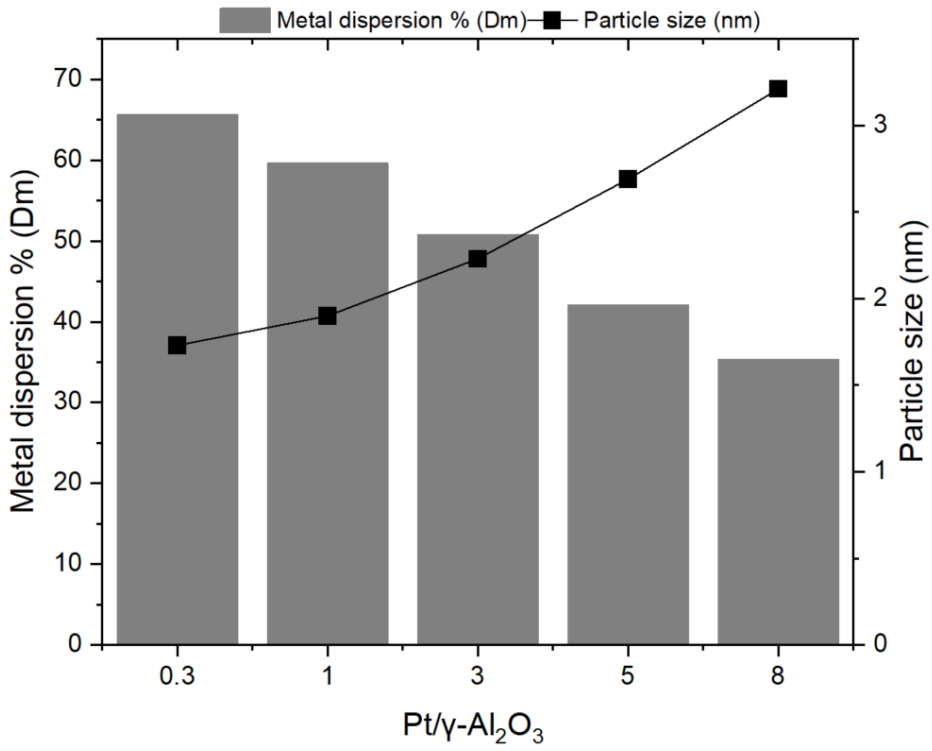

Figure 4.3. Metal dispersion (D_m) and particle size (nm) for five different Pt loadings in Pt/γ-Al_2O_3 (0.3 wt.%, 1 wt.%, 3 wt.%, 5 wt.%, 8 wt.%) determined using CO pulse chemisorption.

Indications are that higher metal loadings result in lower metal dispersion, metal surface area and larger particle sizes. Higher metal particle dispersion facilitates more effective reactant–catalyst surface interaction, which is essential for processes such as oxidation, dehydrogenation, and hydrogenation. However, the trade-off between loading and dispersion implies that more Pt does not necessarily result in higher catalytic efficiency after a particular point. The observed sintering effects and metal agglomeration in high-loading catalysts are in line with this inverse relationship between dispersion and particle size (Peng *et al.*, 2024). Smaller and more evenly distributed NPs are produced at lower Pt concentrations, increasing the proportion of exposed surface atoms that are available for catalytic reactions. TEM analysis confirmed this trend further, showing that larger particle sizes and increased aggregation are correlated with increasing Pt loading.

The catalytic performance of catalysts with lower Pt loadings corresponds to that with smaller and more dispersed NPs. The 0.3 wt.% catalyst with the highest dispersion (65.64%) and the smallest m at 1.11 nm demonstrated the lowest high-boiler formation and the highest dehydrogenation rate. By contrast, the 8 wt.% catalyst with a lower dispersion (35.34%) and a larger m at 4.53 nm demonstrated decreased dehydrogenation productivity and increased by-product formation.

As demonstrated by both CO pulse chemisorption and TEM analysis, the decreased number of

accessible Pt surface sites as a result of NP agglomeration is the cause of this performance decline at higher loadings. The increase in particle size at higher loadings is a sign of sintering and NP aggregation, which reduces the availability of surface atoms (Peng *et al.*, 2024). Further TEM results are given in Section 4.1.6.

4.1.4 Hydrogen temperature programmed reduction

The TCD signal (uV) was plotted against temperature in the H_2-TPR profiles of the Pt/γ-Al_2O_3 catalysts. At 200 °C, a primary reduction peak appears in all samples, signifying the ease of reduction of widely distributed PtO_x species to metallic Pt. This primary peak widens and intensifies with increasing Pt loading, indicating a greater amount of reducible oxide and a more extensive distribution of PtO_x support interaction strengths. The 8 wt.% Pt/γ-Al_2O_3 exhibits a noticeable peak at 225 °C, which is indicative of more bulk-like or strongly bound PtO_2 species, where higher temperatures are required to reduce. Low-loading catalysts on the other hand (0.3–1 wt.%) show small symmetric peaks near 200 °C, suggestive of uniformly small oxide clusters that readily reduce. The trends observed in CO chemisorption and TEM are mirrored in these shifts and peak broadenings with increasing Pt content: larger aggregated particles at high loadings show stronger metal to support interactions and consequently higher reduction temperatures. Higher metal loadings have been shown to cause both broadened TPR peaks and the appearance of high-temperature reduction features in Pt/γ-Al_2O_3 systems (Alexeev *et al.*, 2005).

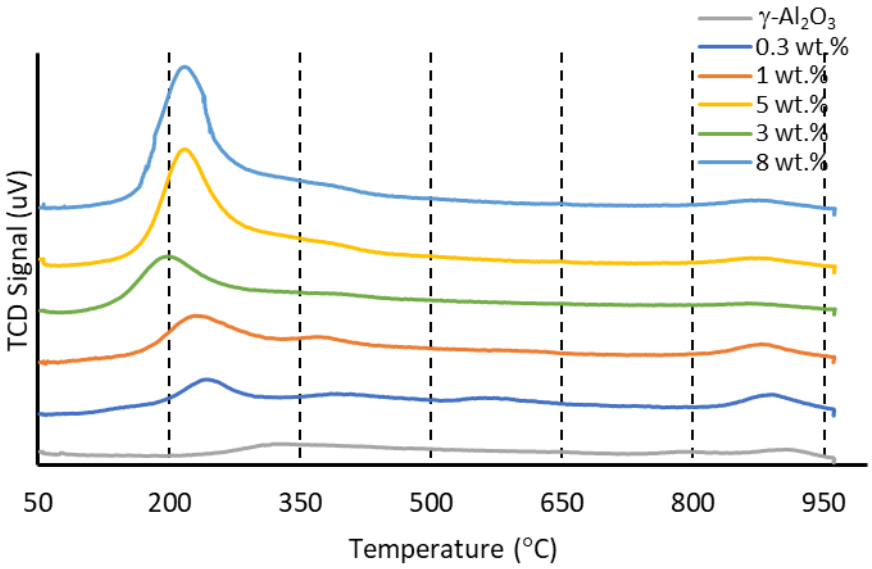

Figure 4.4. H_2-TPR of Pt/γ-Al_2O_3 with various Pt loadings (0.3–8 wt.%) and the γ-Al_2O_3 reference.

4.1.5 Scanning electron microscopy–energy dispersive X-ray spectroscopy

SEM-EDS analysis confirmed the presence of Pt in the reduced catalysts. The catalysts features are seen in Figures 4.5, 4.23, 4.27, 4.31, and 4.32, offering key details about their composition and morphology. SEM-EDS analysis allows for the evaluation of coating thickness homogeneity and structural alterations both before and after dehydrogenation, in addition to confirming the successful deposition of Pt. A relatively uniform Pt dispersion was obtained from the coating thickness measurements derived from SEM imaging. An even distribution of metals makes the active sites more accessible, which enhances reaction efficiency. Furthermore, possible structural degradation, sintering or particle agglomeration can be visually assessed using after-dehydrogenation SEM images. Such degradation can have a substantial impact on the longevity and activity of catalysts. The binders were tested, and their coatings were visually assessed using SEM-EDS. Catalyst optimisation was achieved partially through the use of SEM-EDS to observe the effects of various binders on catalyst stability and porosity by comparing SEM images taken before and after dehydrogenation.

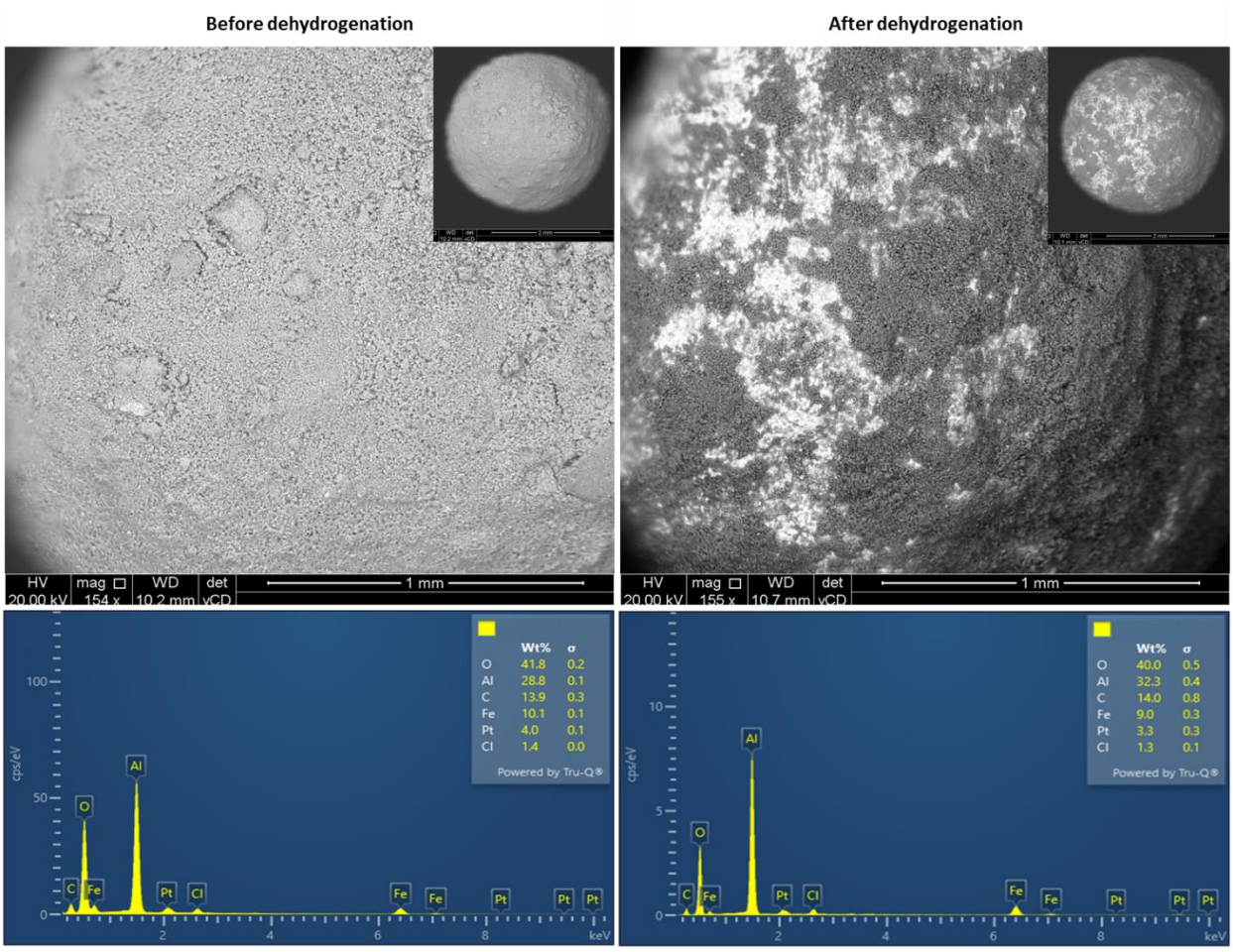

Figure 4.5. SEM micrographs (top) and corresponding EDS spectra (bottom) of SS pellets coated with 5 wt.% Pt/γ-Al_2O_3 (0.11 mol%) before (left) and after (right) dehydrogenation. Process conditions: 50 mL batch reactor, T = 260 °C, reaction time = 55 min, Volume H12-BT (VH12-BT) = 10 mL.

The SEM-EDS images in Figure 4.5 shows 5 wt.% Pt/γ-Al_2O_3 (0.11 mol%) before and after dehydrogenation, displaying good coating stability under reaction conditions. A comparatively even and continuous layer of catalyst is seen prior to dehydrogenation, signifying effective binder application and catalyst deposition. Although there is some surface roughening after 55 min dehydrogenation at 260 °C, no noticeable cracking or coating loss was evident. This implies that the catalyst coating maintains its structural integrity throughout the reaction. The reduction in Pt wt.% after dehydrogenation is due to Pt NP sintering or agglomeration, reducing surface exposure detectable by EDS. Additionally, some coating flakes off during the reaction, lowering its surface concentration.

4.1.6 Transmission electron microscopy

The particle size distribution of Pt NPs in Pt/γ-Al_2O_3 catalysts with Pt loadings (0.3–8 wt.%) on γ-Al_2O_3

is shown in Figure 4.6. TEM measurements of particle size distributions before and after dehydrogenation are displayed in the histograms. A high degree of Pt dispersion on the γ-Al_2O_3 support is indicated by the distributions of smaller Pt NPs at lower Pt loadings. When Pt loading reaches 3 wt.% there is a shift in the distribution of particle sizes toward larger particles, indicating a certain level of accumulation. Regarding the 5 wt.%, the particle size distribution shows a wider spread with particles ranging from 1 nm to >5 nm and a peak shift to about 2. 5 nm. The transition to larger NPs is more prominent in the 8 wt.% Pt/γ-Al_2O_3 catalyst, where the particle size distribution reaches 13 nm, indicating increased metal loading.

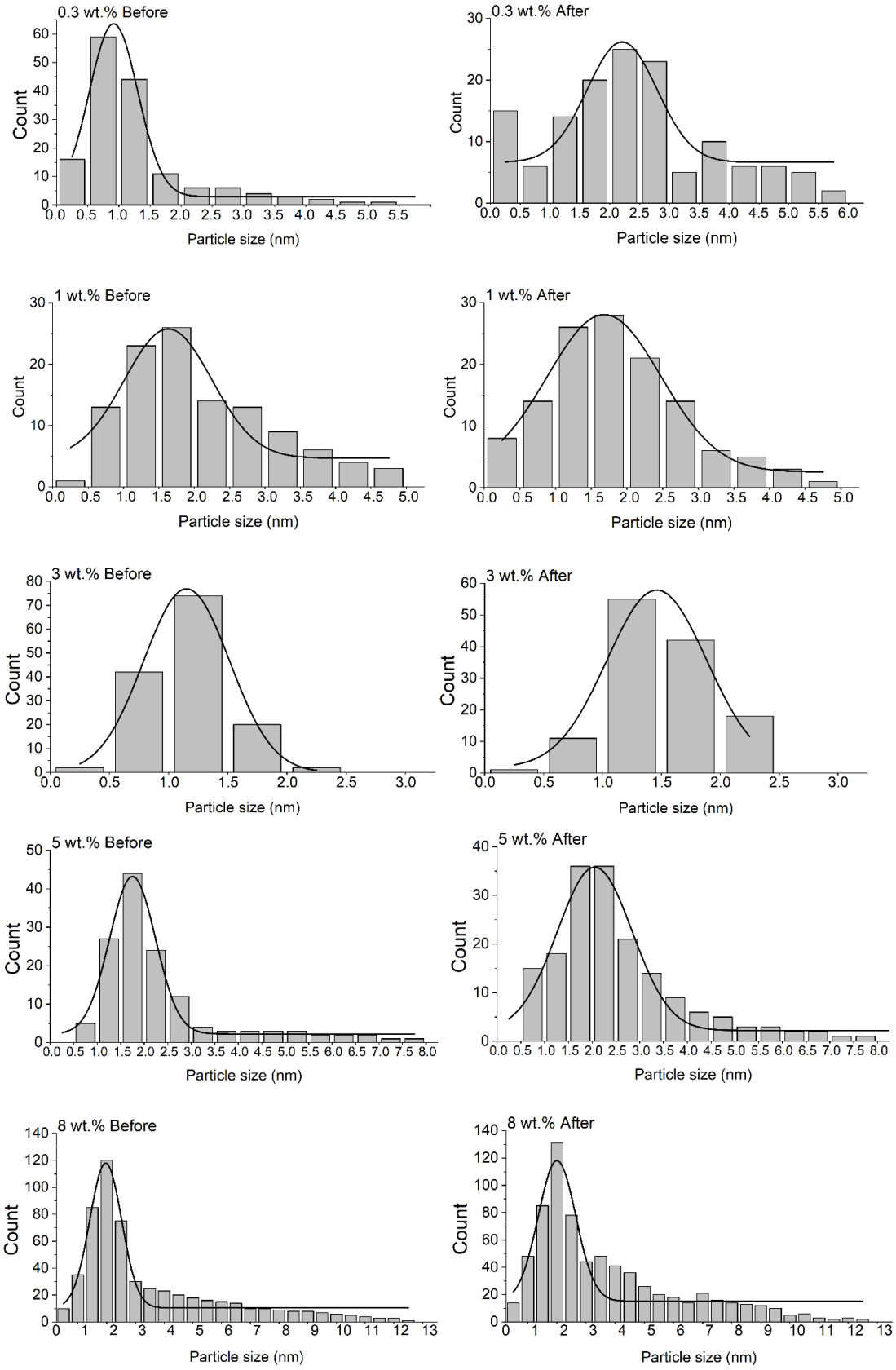

Figure 4.6. Pt NP size distribution for Pt/γ-Al_2O_3 with various Pt loadings (0.3-8 wt.%), before dehydrogenation (left) and after dehydrogenation (right).

Table 4.2 Log-normal distribution parameters, the mean and mode of Pt NPs obtained by TEM before and after dehydrogenation reactions.

Catalyst	σ	μ	m	mode
Before dehydrogenation				
0.3 wt.% Pt/Al_2O_3	0.591	-0.066	1.114	0.660
1 wt.% Pt/Al_2O_3	0.880	0.801	3.281	1.028
3 wt.% Pt/Al_2O_3	0.952	0.459	2.582	0.664
5 wt.% Pt/Al_2O_3	0.459	1.063	3.214	2.345
8 wt.% Pt/Al_2O_3	0.815	1.179	4.531	1.672
After dehydrogenation (80 min)				
0.3 wt.% Pt/Al_2O_3	0.637	0.787	2.692	1.464
1 wt.% Pt/Al2O3	1.068	0.602	3.232	0.583
3 wt.% Pt/Al_2O_3	0.954	0.496	2.582	0.664
5 wt.% Pt/Al_2O_3	0.459	1.063	3.214	2.345
8 wt.% Pt/Al_2O_3	0.757	1.647	6.914	2.926

Where σ is the log-normal standard deviation, μ is the log-normal mean, and m is the mean particle size.

According to the log-normal distribution parameters tabulated (Table 4.3), TEM analysis shows the presence of Pt NPs in all catalyst samples. Before dehydrogenation, the m varied from 1.11 nm to 4.53 nm—there was a distinct upward trend in size with increasing Pt loading. The log-normal mean standard deviation (μ) showed a similar pattern, indicating that higher Pt concentrations led to larger NPs, due to increased precursor availability and synthesis-related coalescence. It is commonly known that systems with higher metal loadings have nucleating particles closer together, which encourages aggregation and results in larger final particle sizes (Grillo *et al.*, 2017). Notably, the mode value of 0.66 nm for 3 wt.% Pt/γ-Al_2O_3 indicates a broad particle size distribution and the presence of smaller particles, despite a relatively high mean size.

The majority of samples showed a discernible increase in particle size following 80 min of dehydrogenation, suggestive of sintering effects. The sintering temperature of Pt is at 700 °C—confirmed by Harris, who found that heating to 700 °C in air resulted in extremely quick sintering, and after 8 h the mean particle diameter increased from 50 Å to 300 Å (Harris, 1986). According to the shape of the particle size distributions and the types of particle structures seen in sintered catalysts, the mechanism was a mix of Ostwald ripening, and whole particle migration and coalescence (Harris, 1986). The catalyst with the most significant increase in particle size was the 8 wt. % Pt/γ-Al_2O_3, increasing from 4.53 nm to 6.91 nm, which is in line with higher metal loadings tending to encourage the migration of NPs under reaction conditions. The dehydrogenation reactions occur at 260 °C, which

is a significantly lower temperature, not causing sintering. Therefore, the Pt catalyst is stable and active throughout dehydrogenation, ensuring effective catalytic performance. There was a smaller increase in particle size for the 3 wt.% Pt/γ-Al_2O_3, indicating that sintering was less notable at lower Pt concentrations.

Significantly, the mode size of the 1 wt.% Pt/γ-Al_2O_3 catalyst decreased, which suggests particle redistribution as opposed to widespread growth in average particle size. This behaviour is consistent with the findings of other research on supported Pt catalysts, where the evolution of particle size is dependent on the support's thermal stability as well as metal loading (Auer *et al.*, 2020). The difference of the σ values shed more light on these changes. Dehydrogenation catalysts with higher Pt loadings showed wider distributions, whereas lower Pt loadings maintained a comparatively narrow distribution, indicating greater particle size variability. According to similar findings documented in the literature, depending on the catalyst composition and the support characteristics, the thermal treatment at high temperatures causes particle redistribution (Mäki-Arvela & Murzin, 2013). Data suggest that synthesis-related effects such as enhanced nucleation, aggregation and possible coalescence during calcination are responsible for the larger particle sizes seen at higher Pt concentrations. As a result, catalyst performance is impacted from the decrease in active surface area at higher loadings. True sintering during the reaction is unlikely because dehydrogenation reactions take place at 260 °C.

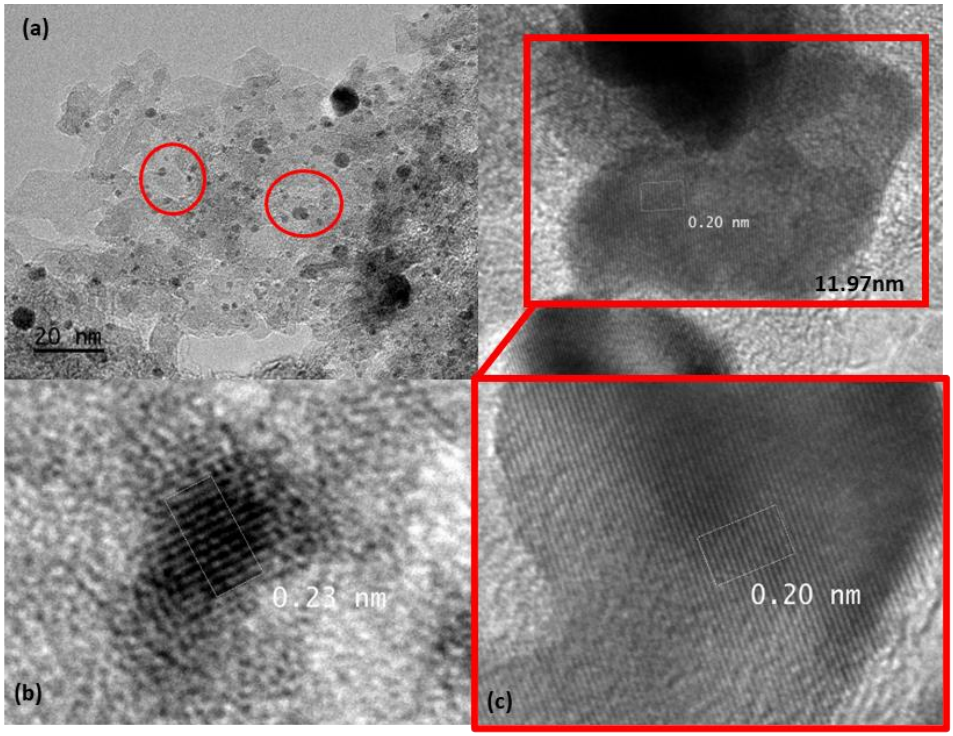

Figure 4.7. TEM images: d-spacing of 8 wt.% Pt/γ-Al_2O_3 where (a) overview of Pt NP's (b) before dehydrogenation and (c) after dehydrogenation. Conditions: 80 mL H12-BT, 265 °C.

Figure 4.7A shows the presence of Pt NPs (dark, well-dispersed particles). The d-spacing values indicate that the 8 wt.% Pt/γ-Al_2O_3 catalyst underwent structural changes before and after dehydrogenation, as revealed by HR-TEM analysis and a measured d-spacing of 0.23 nm prior to dehydrogenation (Figure 4.7B). This closely matches the d-spacing measured for the standard face-centred-cubic (fcc) structure Pt from International Centre for Diffraction Data (ICDD)—it measured the d-spacing Pt(111) at 0.226 nm (2.26 Å) (Faber & Fawcett, 2002). The presence of the Pt(111) crystallographic plane is thus indicated. Furthermore, the image shows a comparatively wide size distribution with smaller NPs scattered throughout the alumina support. Following dehydrogenation at 265 °C over 80 min, the d-spacing is significantly reduced to 0.20 nm (Figure 4.7C).

Sintering-induced particle growth and structural rearrangement are responsible for this lattice contraction. Tabib Zadeh Adibi *et al.* noted that lattice rearrangement and densification result from particle growth and migration processes during the sintering of Pt NPs under thermal treatment, which alters the crystallographic structure. This suggests that this shift in lattice contraction is caused by combination-driven sintering (Tabib Zadeh Adibi *et al.*, 2016).

4.1.7 Thermogravimetric analysis

Weight loss is shown as a function of temperature in the TGA curves of the four binders: two PVAs and two PVPs. At temperatures <200 °C, the initial weight loss is seen mostly as a result of the removal of low molecular weight components and absorbed moisture. Between 300 and 450 °C, there is a noticeable weight loss, explained by the primary decomposition step where the polymer backbone disintegrates and releases volatile degradation products. A slower and more gradual weight loss may take place at higher temperatures, which could be related to the residual carbonaceous material breaking down further and leaving behind charred residues. PVP with a lower molecular weight (PVP 55000) exhibits a more noticeable final decomposition step, which is indicative of variations in the polymer structure and chain length. By highlighting the temperatures at which the highest rates of weight loss take place, the derivative weight curves help to clarify the kinetics of each binder's breakdown (Rao *et al.*, 1999). A factor in determining the binder's thermal stability and decomposition behaviour is its molecular weight (Maity *et al.*, 2015). At lower temperatures, lower molecular weight polymers tend to decompose quickly, whereas higher molecular weight polymers typically show slower decomposition and improved thermal stability.

By determining the temperatures at which decomposition takes place, TGA analysis plays a crucial role in this work—in efforts to select the most suitable binder materials. The structural integrity of the prepared catalyst is influenced by the thermal stability, which guarantees that the selected binder can be completely eliminated during catalyst preparation without leaving residues.

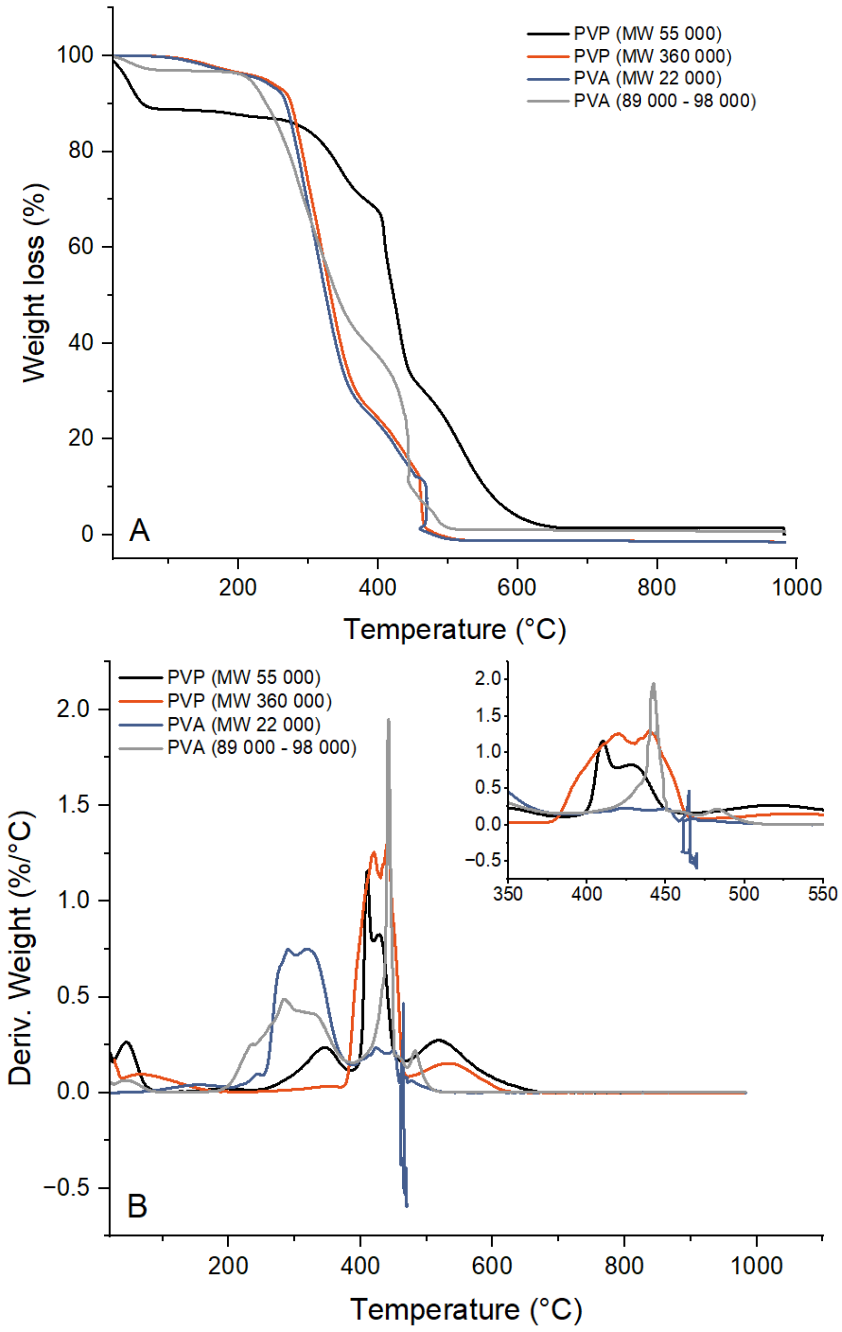

Figure 4.8. TGA curves of four binders: PVP 55000, PVP 360000, PVA 22000 and PVA 89000–98000: (A) weight loss and (B) derivative weight.

4.1.8 X-ray powder diffraction (XRD)

The synthesised catalysts were characterised by XRD to investigate the structural characteristics of Pt/γ-Al_2O_3 (0.3–8 wt.%). The purpose of this analysis was to investigate the existence of crystalline phases and track any changes brought on by an increase in the Pt content.

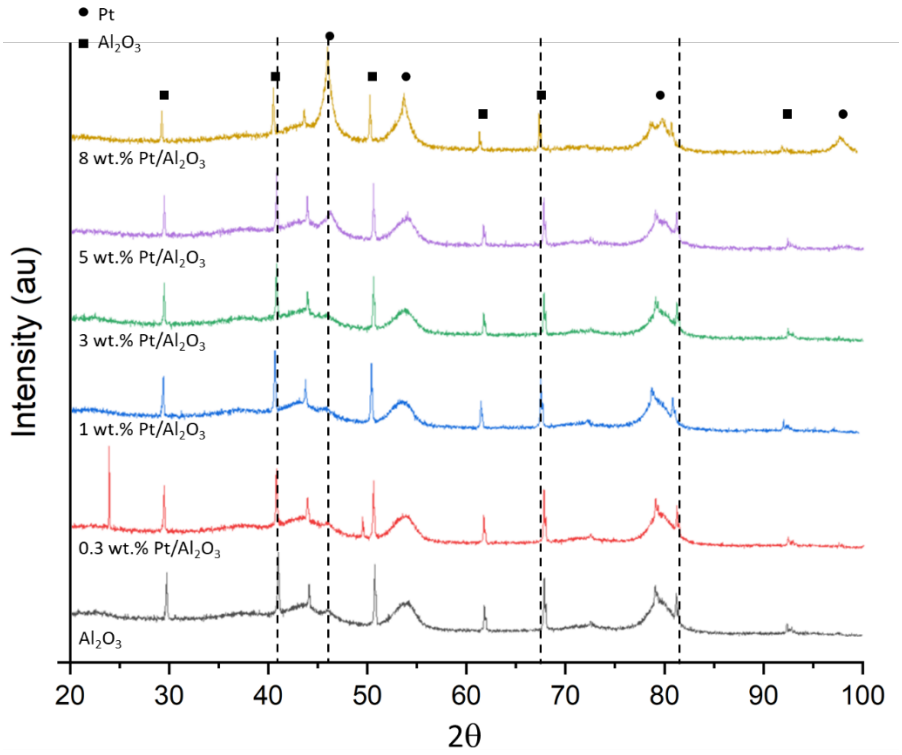

Figure 4.9. XRD patterns of Al_2O_3 support and Pt/γ-Al_2O_3 catalysts (0.3–8 wt.%).

Figure 4.9 shows the XRD patterns of Pt/γ-Al_2O_3 catalysts with various loadings: 0.3–8 wt.%. All the diffraction peaks are attributed to the phase structure of the Al_2O_3 support, including the γ-phase Al_2O_3 and bayerite. The presence of the γ-Al_2O_3 is indicated by the characteristic 2θ values of the diffraction peaks corresponding to the γ-Al_2O_3 support. As the Pt loading increases, additional peaks emerge that correspond to Pt, notably around 39.8°. As the Pt loading increases these Pt peaks then become increasingly more intense, indicating that Pt particles are growing as the Pt concentration increases. At low Pt loadings (0.3 wt.%), the Pt peaks are not clearly visible. This is due to the wide distribution of Pt on the alumina support. Additionally, the figure displays the expected locations of the Pt peaks, as indicated by the vertical black lines around the 2θ values of 39.8° (Pt (111)), 46.2° (Pt (200)), 67.5° (Pt (220)) and 81.5° (Pt (311)), which correspond to the fcc structure of Pt. These results correspond with those of Shah, who reported broad diffraction peaks, where 2θ equals 39.6, 47.4, 67.1 and 81.2 for Pt (111), Pt (200), Pt (220) and Pt (311), respectively (Shah, 2012). This also corresponds to the fcc structure of Pt (JCPDS Card 04-0802).

Furthermore, the γ-Al_2O_3 peaks do not change with changing Pt loadings, thus indicating that the alumina support retains its structural integrity at all Pt concentrations here. This is because Pt accumulates as metallic NP's on the surface of γ-Al_2O_3 without disrupting the lattice, due to weak interaction between Pt and γ-Al_2O_3. The increasing intensity of Pt peaks with loading corresponds to

the growth of these NP's, as also reflected in the particle size data. The relative abundances of Pt, measured by ICP-OES and presented in Table 4.1, confirm the actual Pt loadings in each catalyst sample. This quantitative data supports the XRD observations by showing successful Pt incorporation and correlating with the observed increase in particle size as Pt loading increases.

In line with the increasing intensity of the Pt peaks in the XRD patterns, this suggests that the Pt particles are increasing in size as the concentration increases. Table 4.2 shows the particle size (nm) obtained from the XRD data, where the particle size obtained for 0.3 wt.% is 0.706 nm, indicating the dispersed nature of the Pt. The particle size increases as the concentration of Pt increases, with 2.814 nm, 2.971 nm and 3.348 nm corresponding to 1 wt.%, 5 wt.% and 8 wt.%, respectively. The exception is 1.437 nm for 3 wt.%, which is away from the trend —possibly due to a poor preparation method. The interaction between Pt and Al_2O_3 may result in a more dispersed smaller particle size distribution at low Pt loadings. There are fewer support sites available for dispersion as the Pt loading increases and Pt particles form agglomerations as the Pt content increases.

The crystallinity shown in the XRD patterns results from the well-defined γ-Al_2O_3 support and the fcc structure of Pt. The catalyst's physical structure is preserved by the γ-AlO_3 phase, which offers a stable, high-surface-area scaffold that keeps its structural integrity at all Pt loadings. The increasing crystallinity of Pt NP's with higher loadings reflects particle growth and agglomeration, which directly influences the active site availability and dispersion.

4.2 Inductive Heating for the Dehydrogenation of LOHCs: Assessing Feasibility

An inductive heating module needs to be optimised for the temperatures required for dehydrogenation; otherwise, high temperatures above1000 °C can be reached. This will then lead to decomposition of the LOHC molecule as well as sintering of the catalyst. To overcome the difficulties that inductive heating tests present, several experiments were carried out to assess how well various SS and catalyst configurations performed in the dehydrogenation of H12-BT. The tests sought to determine how changes in SS pellet treatments and catalyst composition affect overall dehydrogenation performance, hydrogen production and heating efficiency.

The following tests were conducted. (1) SS pellets were left uncoated to create a baseline for determining heating behaviour. (2) SS pellets were mixed with Pt/γ-Al_2O_3 to examine the impact of a higher catalyst-to-H12-BT ratio ($n_{Pt}/n_{H12\text{-}BT}$) and (3) Pt/γ-Al_2O_3 coated SS pellets were utilised to assess the impact of coating SS with a catalyst at a lower molar ratio. (4) Pt/γ-Al_2O_3 pellets were mixed with SS pellets to compare the performance with that of the prior configurations. Due to thermocouple

interference above 200 °C, the inductive heater circuit was also automated to increase temperature accuracy.

The purpose of these tests was to determine how the catalyst configurations affected the process's overall viability, the dehydrogenation efficiency, and the inductive heating. During testing of the inductive heating, technical challenges were evident when using only SS pellets immersed in H12-BT. For example, the AC magnetic field interfered with the thermocouple measurements, particularly at temperatures >200 °C. To address this, the inductive heater circuit was then automated to periodically switch off every 2 sec, for 0.1 sec, to obtain more accurate temperature measurements, compensating for the decreasing magnetic permeability of the SS pellets when approaching the Curie temperature (720–750 °C; 316 SS) (Ara, 1989). This is a critical point, beyond which a material loses its magnetic properties, with a reduction in the efficiency of inductive heating.

Figure 4.10 shows the inductive heating temperature and power consumption when using uncoated SS pellets, SS pellets mixed with catalyst-coated SS pellets, and SS pellets mixed with Pt/γAl_2O_3 pellets. Uncoated SS pellets served as a benchmark for comprehending the support materials' initial heating behaviour in the absence of coating or catalytic effects. In the case of the SS pellets without catalyst, an P consumption of 73 W was achieved when a temperature of 260 °C was maintained for approximately 50 min (Figure 4.10a). In the case of the mixed pellets (Pt/γ-Al_2O_3 + SS pellets) at a catalyst to H12-BT ratio of 0.52 mol%, 66 W was consumed for the dehydrogenation of H12-BT at 260 °C (Figure 4.10b), whereas at a lower molar ratio of 0.11 mol%, in the case of the Pt/γ-Al_2O_3 catalyst-coated SS pellets, 68 W was required to maintain a dehydrogenation temperature of 260 °C (Figure 4.10c). Finally, the Pt/γ-Al_2O_3 pellets mixed with uncoated SS pellets (Pt/γ-Al_2O_3 coated SS at 0.11 mol%) required 67 W for the dehydrogenation of H12-BT (Figure 4.10d).

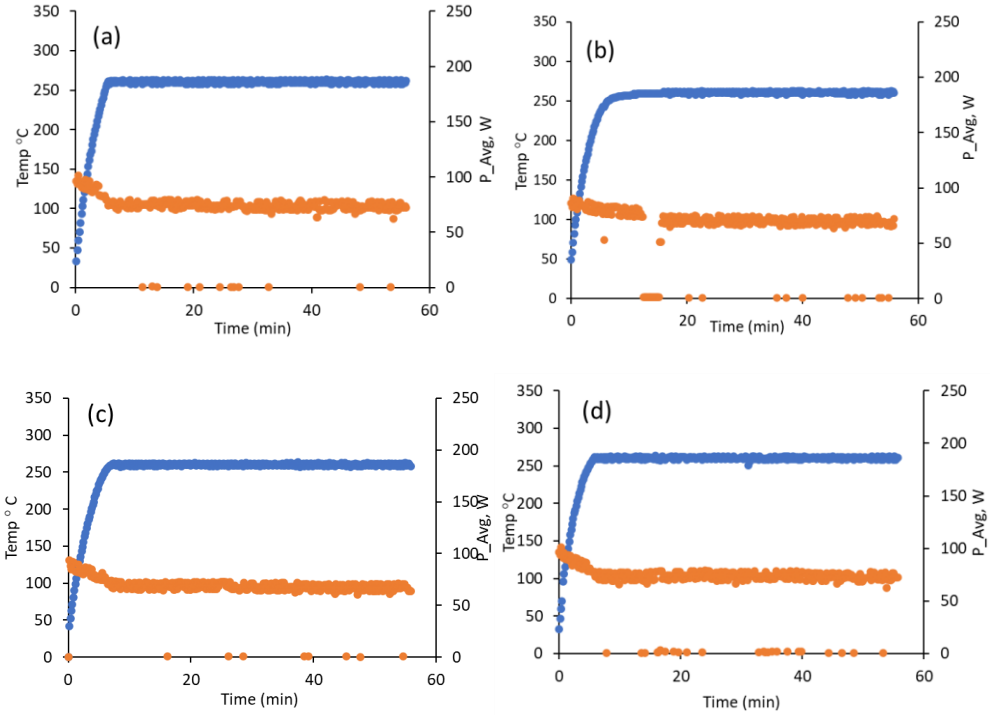

Figure 4.10. Comparison of the inductive heating temperature and power consumption for various configurations: (a) uncoated SS pellets, (b) Pt/γ-Al_2O_3 + SS, $n_{Pt}/n_{H12\text{-}BT}$ = 0.52 mol%, (c) Pt/γ-Al_2O_3 coated SS $n_{Pt}/n_{H12\text{-}BT}$ = 0.11 mol%, (d) Pt/γ-Al_2O_3 + SS, $n_{Pt}/n_{H12\text{-}BT}$ =0.11 mol%. Process conditions: 50 mL batch reactor, T = 260 °C, reaction time = 55 min, VH12-BT = 10 mL.

The power consumption for all the dehydrogenation tests in which Pt/γ-Al_2O_3 + SS was used was lower compared to when only SS pellets were used. This observation suggests that while the core material (SS) is responsible for the inductive heating, due to its electrical conductivity and magnetic permeability, the coating and Pt/γ-Al_2O_3 catalyst pellets could interfere with how the magnetic field interacts with the SS pellets.

To validate the suitability of inductive heating for the dehydrogenation of H12-BT, liquid samples of HBT were taken at 10-min intervals, while the flow rate was recorded manually using a bubble flow meter. The gas collected using a sample bag, was analysed using a Hiden HPR-20 R&D Specialist Gas Analysis System (Hiden, UK). A clear hydrogen peak (m/z = 2; >99.9%), without any impurities, was observed. The catalyst efficiency was calculated in terms of the amount of hydrogen produced per gram of Pt and time ($gH_2gPt^{-1}min^{-1}$). See Figure 4.11. The uncoated SS pellets mixed with Pt/γ-Al_2O_3 catalyst pellets ($n_{Pt}/n_{H12\text{-}BT}$ = 0.11 mol%) exhibited the highest productivity of 0.35 $gH_2gPt^{-1}min^{-1}$, followed by the catalyst-coated SS pellets ($n_{Pt}/n_{H12\text{-}BT}$ = 0.11 mol%) and the uncoated SS pellets mixed with catalyst pellets ($n_{Pt}/n_{H12\text{-}BT}$ = 0.52 mol%) at 0.29 and 0.27 $gH_2gPt^{-1}min^{-1}$, respectively. In the absence of catalysts, no hydrogen production was observed.

Liquid samples from Pt/γ-Al_2O_3 + SS (0.52 mol%) were drawn from the reactor and analysed using GC-SQ-MS to determine the composition of the product: H12-BT, H6-BT and HBT were present (Figure 4.11, right). As expected, the mole fraction of the reactant (H12-BT) decreased with increasing time, leading to the formation of the intermediate H6-BT and the product HBT (Ford *et al.*, 2024). Within the 50-min reaction time, the H6-BT increased more rapidly than the HBT. The concentration of H6-BT decreased during the last 40–50 min, with a subsequent increase in HBT. This confirmed the stepwise dehydrogenation reaction pathway, as reported in literature, where H12-BT converts to HBT via H6-BT (Ford *et al.*, 2024).

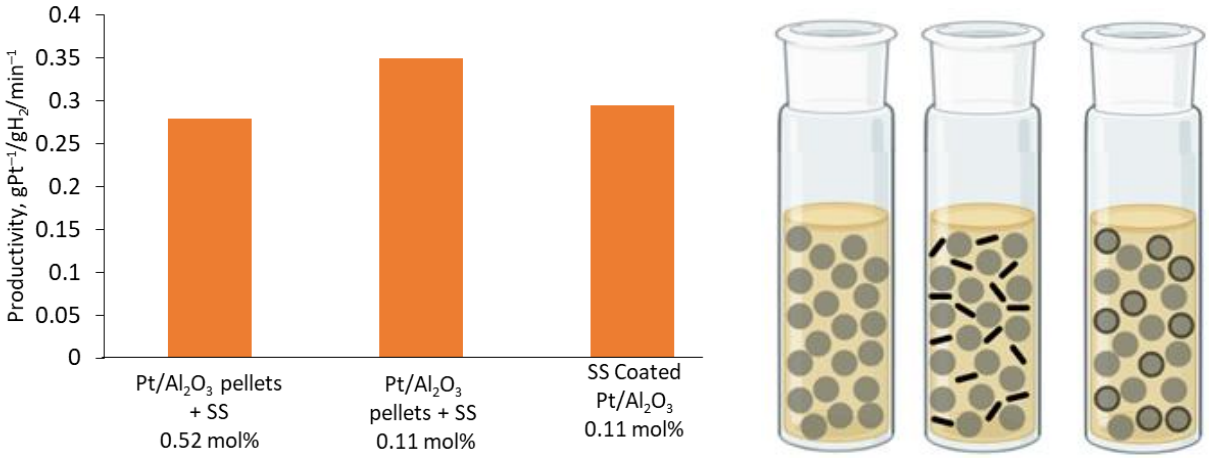

Figure 4.11. Left: Comparison of catalyst productivity for the dehydrogenation of H12-BT, using an inductive heating batch reactor, for three different catalyst configurations: (a) Pt/γ-Al_2O_3 + SS (0.52 mol%), (b) Pt/γ-Al_2O_3 + SS (0.11 mol %), (c) Pt/γ-Al_2O_3 coated SS (0.11 mol%). Right: Three configurations used in the experiments (refer to Figure 3.6).

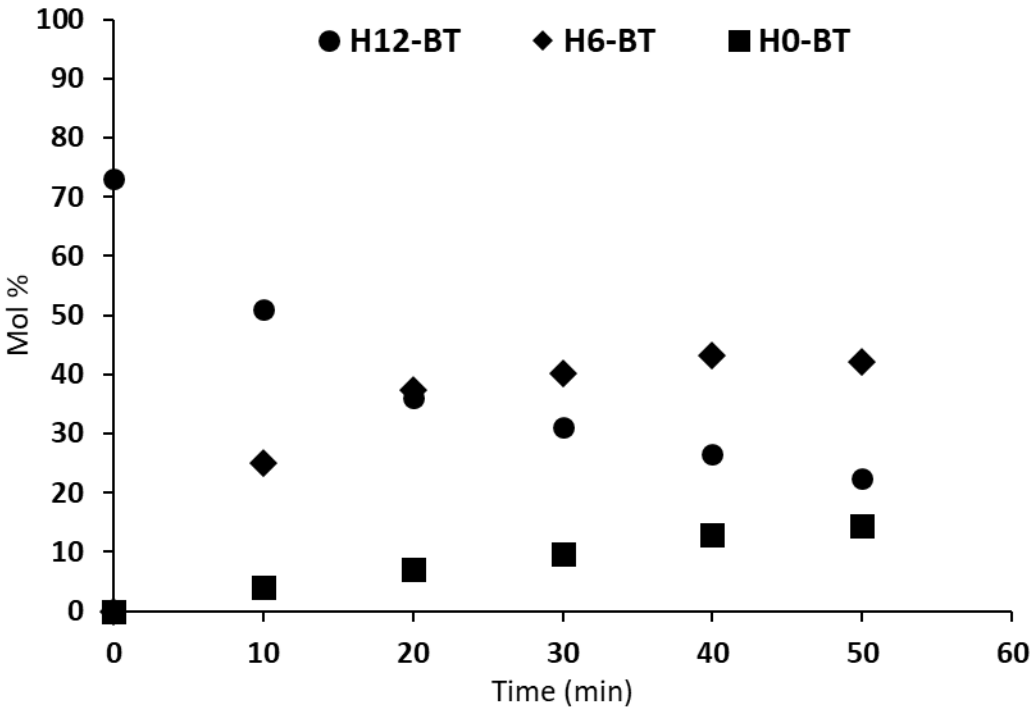

Figure 4.12. Product distribution over reaction time for the dehydrogenation of H12-BT using Pt/γ-Al_2O_3 + SS (0.52 mol%) at 260 °C.

Table 4.4 presents catalyst performance data for the dehydrogenation of H12-BT using inductive heating. The critical role of the Pt catalyst/H12-BT molar ratio on the efficiency of the dehydrogenation process is highlighted. A higher molar ratio leads to an increased DOD conversion of H12-BT and selectivity towards the desired dehydrogenated product (HBT), although at a reduced productivity. This trade-off suggests that optimising the Pt concentration is crucial for the full exploitation of the hydrogen storage capacity of the H12-BT as well as for maximising the catalyst efficiency. Moreover, a decrease in the concentration of Pt by almost 80% (79%) resulted in a 7.4% change in productivity for Pt/γ-Al_2O_3 coated SS pellets, where an improved productivity implies that less catalyst is required to achieve an increased amount of product, thus making the dehydrogenation process more cost effective.

Table 4.3 Catalyst performance data for the dehydrogenation of H12-BT using inductive heating. Process conditions: 50 mL batch reactor, T = 260 °C, reaction time= 55 min, VH12-BT = 10 mL.

Catalyst	**$n_{Pt}/n_{H12\text{-}BT}$ (mol%)**	**Productivity ($gH_2gPt^{-1}min^{-1}$)**	**DOD (%)**	**Conversion (%)**	**Selectivity (%)**
Pt/γ-Al_2O_3 + SS (mix)	0.11	0.35	16	6	3
Pt/γ-Al_2O_3 + SS (mix)	0.52	0.27	45	65	18
Pt/γ-Al_2O_3 coated SS	0.11	0.29	20	15	4

Furthermore, the configuration of the catalyst, i.e., whether mixed with or coated on SS, has an impact on the reaction. Coating the catalyst on SS improves the performance slightly, compared to mixing it at the same platinum to H12-BT ratio. This indicates that catalyst–support interactions also play a role in the reaction efficiency. Desirable targets for the dehydrogenation of LOHCs include the following: productivity >3 gH_2/g_{cat}/min, energy demand <6 kWh/kg-H_2, conversion >90% and selectivity >99.8% (Lin & Bagnato, 2024).

Upon comparing the data in Table 4.4 with the desirable targets for the dehydrogenation of LOHCs, it is evident that none of the catalysts considered here achieve a conversion rate that is >90%, nor a selectivity target that is >99.8%. The Pt/γ-Al_2O_3 + SS (mix) catalyst with nPt/nH12-BT of 0.11 mol% exhibited the highest selectivity of 18%. While none of the catalysts here meet the productivity target (i.e., exceeding 3 gH_2/g_{cat}/min), the highest recorded productivity was 0.35 $gH_2/gPt^{-1}min^{-1}$ for the first Pt/γ-Al_2O_3 + SS (mix) catalyst at 0.11 mol%.

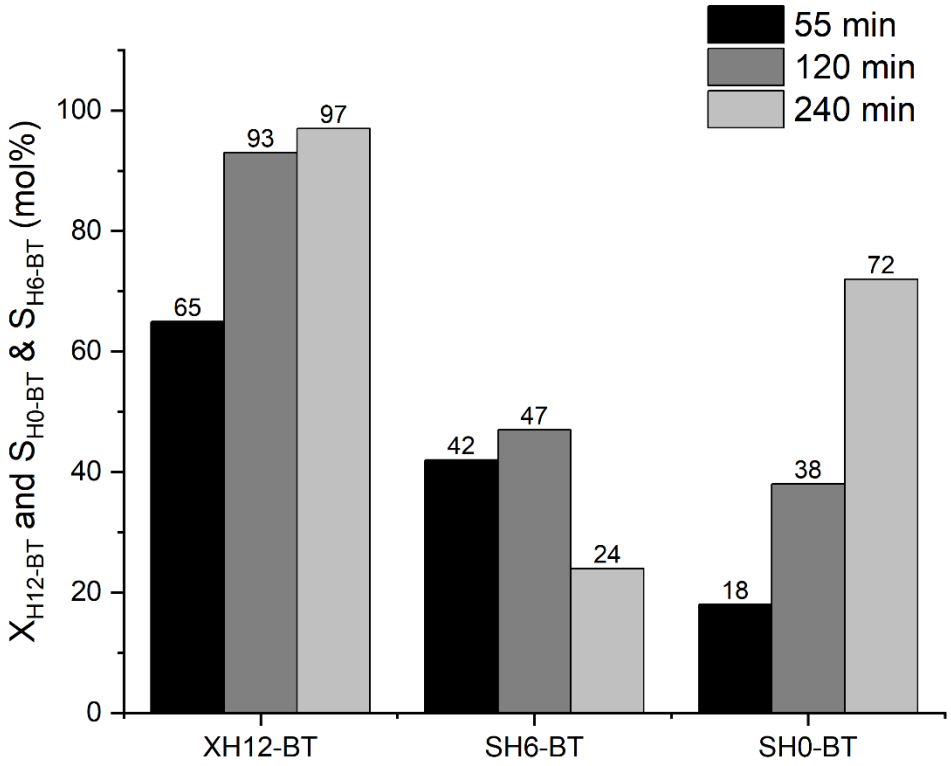

Figure 4.13. H12-BT conversion and selectivity to H6-BT and HBT. Pt/γ-Al_2O_3 + SS (mix): nPt/nH12-BT = 0.52 mol %,T = 260 °C.

Figure 4.13 shows the conversion of H12-BT and its selectivity at different reaction times (55 min, 120 min and 240 min) at 260 °C, with Pt/γ-Al_2O_3 + SS as catalyst (0.52 mol%). There is a clear trend in the conversion of H12-BT and selectivity towards partially and fully dehydrogenated products. The selectivity for H6-BT (X_{H6-BT}) increased with reaction time, increasing from 18% to 72.54% as the reaction time increased from 55 min to 240 min. A high level of reaction efficiency was also demonstrated by the H12-BT (X_{H12-BT}) conversion, which reached 97.82% after 240 min. The X_{H6-BT} peaked at 47.28% after 120 min, but declined to 24.71% after 240 min, as the dehydrogenated product progressed to HBT. These findings demonstrate how the catalyst selectivity changes throughout the reaction and points to an area that could benefit from further refinement towards increased productivity and selectivity for H12-BT. This further points to a progressive reaction pathway, where the catalyst exhibits good conversion and selectivity properties. Although the desired catalyst targets were not yet met, this study demonstrates the feasibility of inductive heating for H12-BT dehydrogenation—yet further research is required on the optimisation hereof, to meet efficiency benchmarks.

Based on the results to date, the best catalyst configuration was found when combining Pt/γ-Al_2O_3

coated SS pellets with uncoated SS pellets at a molar ratio of 0.11%. This combination gave a better balance between reactor stability, energy efficiency and hydrogen productivity. The coated pellet system exhibited a significantly higher hydrogen productivity of 0. 35 gH_2/gPt/min, compared to 0.21 gH_2/gPt/min for the 'loose' physical mixture of Pt/γ-Al_2O_3 with SS pellets. The coated system also outperformed the loose mixture, which converted 56% of the H12-BT within 80 min, reaching 61.9%. The coated catalyst demonstrated an efficient dehydrogenation progression with primarily HBT formation and minimal intermediates (e.g., H6-BT) remaining during prolonged operation, then achieving a final conversion of 97.82%. Additionally, by avoiding the catalyst segregation and hot spot formation that are seen with loose mixtures, the coating approach improved thermal stability and energy transfer during inductive heating. Crucially, during the reaction, the coated SS pellets retained their mechanical integrity, thus making reactor handling easier and reducing the possibility of catalyst loss. Compared to the results of simple physical mixtures, these results clearly demonstrate that Pt/γ-Al_2O_3 coated SS pellets mixed with uncoated SS pellets are a more reliable and effective option for inductively heated LOHC dehydrogenation, offering promising potential for future scale-up.

The use of 5 wt.% Pt/γ-Al_2O_3 for the initial tests arose from it being a commonly used catalyst in another research. This is a result of the number of Pt active sites that allow for near complete conversion, larger Pt NPs that is formed at 5 wt.% loading that prevent rapid deactivation (Wu *et al.*, 2024). The catalyst also remains stable in the range 200–400 °C (Wu *et al.*, 2024). However, a more detailed review of the 0.3 wt.%, 1 wt.%, 3 wt.%, 5 wt.% and 8 wt.% should be carried out, to better understand the impact of Pt loading on catalytic performance under inductive heating.

4.3 Evaluation of Conventional Heating Performance: Dehydrogenation of H12-BT

The DOD and cumulative hydrogen flow for both conventional electrical heating and inductive heating is compared in Figure 4.14. Although here electrical heating achieved a slightly higher DOD (33.83%) than inductive heating (33.10%), the difference is minimal, indicating that both techniques are effective. The gas-phase dehydrogenation exhibits a comparable pattern suggesting similar kinetics and conversion for both electrical and inductive heating. Interestingly, the inductive heating gas-phase dehydrogenation process is still competitive, demonstrating its ability to effectively promote hydrogen release. Moreover, the cumulative hydrogen flow results showed that inductive heating offers a more regulated and consistent hydrogen release, which can be beneficial for process stability, even though electrical heating produces a marginally higher hydrogen output.

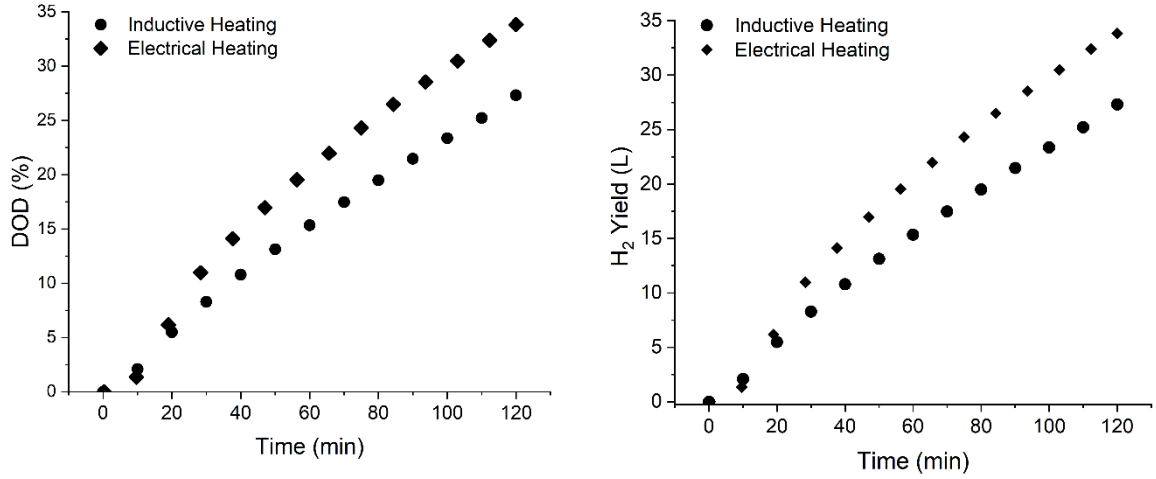

Figure 4.14. Comparison of conventional electrical and inductive heating: (left) DOD and (right) hydrogen yield. Process conditions: coated 5 wt.% Pt/Al_2O_3 SS pellets (81 μm), 50 mL batch reactor, reaction time = 120 min, VH12-BT = 10 mL, T = 260 °C.

Table 4.4. Comparison of electrical and inductive heating.

Heating method	$n_{Pt}/n_{H12\text{-}BT}$ (mol%)	Max flow (mL/min)	Productivity ($gH_2gPt^{-1}min^{-1}$)	Cumulative flow (L)
Inductive	0.089	27.78	0.317	1.65
Electrical	0.089	62.56	0.715	2.03

A quantitative comparison for electrical and inductive heating is given in Table 4.5. Inductive heating produces a more stable and regulated heating profile, leading to prolonged hydrogen production—even at the same catalyst loading as used for electrical heating (0. 089 mol% Pt:H12-BT). The steady temperature gradient of inductive heating creates a more uniform reaction environment, which may improve catalyst longevity and operational stability, even though electrical heating has a higher maximum flow rate (62.56 mL/min) than inductive heating (27.78 mL/min). Furthermore, inductive heating results in a somewhat lower cumulative hydrogen flow, 1.65 L vs. 2.03 L for electrical heating. The technique offers improved heat management, lowering the risk of thermal hotspots and catalyst degradation.

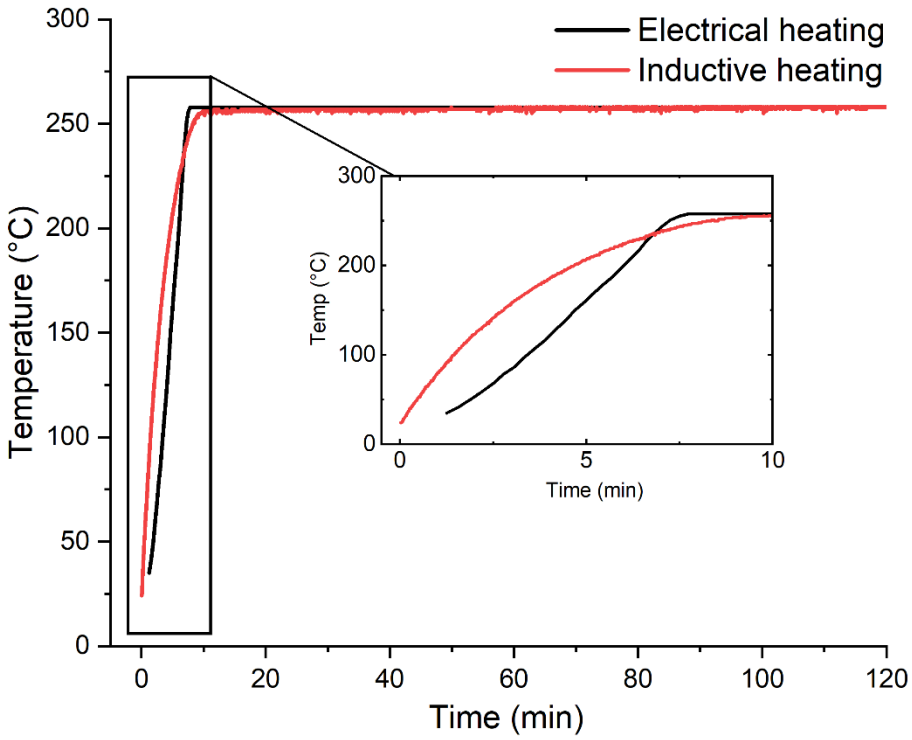

Figure 4.15. Temperature gradient comparison for conventional and inductive heating. Process conditions: coated 5 wt.% Pt/Al_2O_3 SS pellets (81 μm), 50 mL batch reactor, reaction time = 120 min, VH12-BT = 10 mL.

The temperature gradient profiles for inductive and electrical heating are examined in Figure 4.15, which also shows the steady-state behaviour and heating rates. A more controlled and gradual temperature ramp-up is provided by inductive heating, which guarantees even heat distribution throughout the reaction system. The steady increase seen with inductive heating reduces thermal stress on the system, which may result in better long-term performance even though electrical heating reaches the target temperature (250 °C) more quickly. During extended operation times, inductive heating maximises reaction efficiency by maintaining a very stable thermal environment once the target temperature is reached.

In conclusion, effective dehydrogenation is accomplished by both electrical and inductive heating. However, inductive heating is distinguished by its stable and regulated thermal profile. This improves catalyst stability and reduces thermal stress by creating a more homogeneous reaction environment. For BT dehydrogenation inductive heating is a practical and more sustainable option due to its efficient heat distribution and steady hydrogen release, especially for applications requiring long-term operational stability.

4.4 Evaluation of Catalyst Performance: Impact of Loading on Hydrogen Production

Results for the productivity as a function of Pt loading are shown in Figure 4.16: the effects of both a constant Pt/LOHC ratio (0.12 mol%) and constant quantity of Pt/γ-Al_2O_3 (0.2 g) are compared. Both variables were held constant under the same reaction conditions in order to investigate how the Pt/LOHC ratio and Pt/γ-Al_2O_3 mass influence Pt loading and catalytic activity. In the upper figure it is shown that productivity decreases with increasing Pt loading, suggesting an optimal range for catalytic activity. A peak productivity of 0.50 $gH_2/g_{cat}/min$ was observed at 0.35 wt.% Pt/Al_2O_3, but productivity decreases progressively at higher Pt loadings. However, using 0.35 wt.%, 1 wt.% or 3 wt.% for coating on SS pellets makes achieving a higher mol% is limited due to excessive coating thickness of the catalyst layer. A thicker coating also raises further issues with uneven distribution, reduced adhesion, and mass transport limitations. Additionally, the thickness of the coating on SS pellets may introduce diffusion barriers, reducing active site accessibility and the productivity. This suggests that thinner coatings will improve the reaction kinetics during dehydrogenation. This will be discussed further in Section 4.6.

Conversely, the lower figure shows that at a constant catalyst amount (0.2 g), productivity improves with higher Pt loadings—peaking at 8 wt.%, with a value of 0.0177 $gH_2/g_{cat}/min$. Increasing the amount of Pt, while maintaining the same catalyst mass, increases the concentration of active sites as the wt.% increases. This implies better dispersion because a higher Pt loading usually results in a more even distribution of Pt on the catalyst surface, increasing the number of active sites available for the dehydrogenation reaction. Higher Pt loading results in increased catalytic activity, which suggests that the Pt is more evenly distributed and makes Pt sites more accessible throughout the reaction.

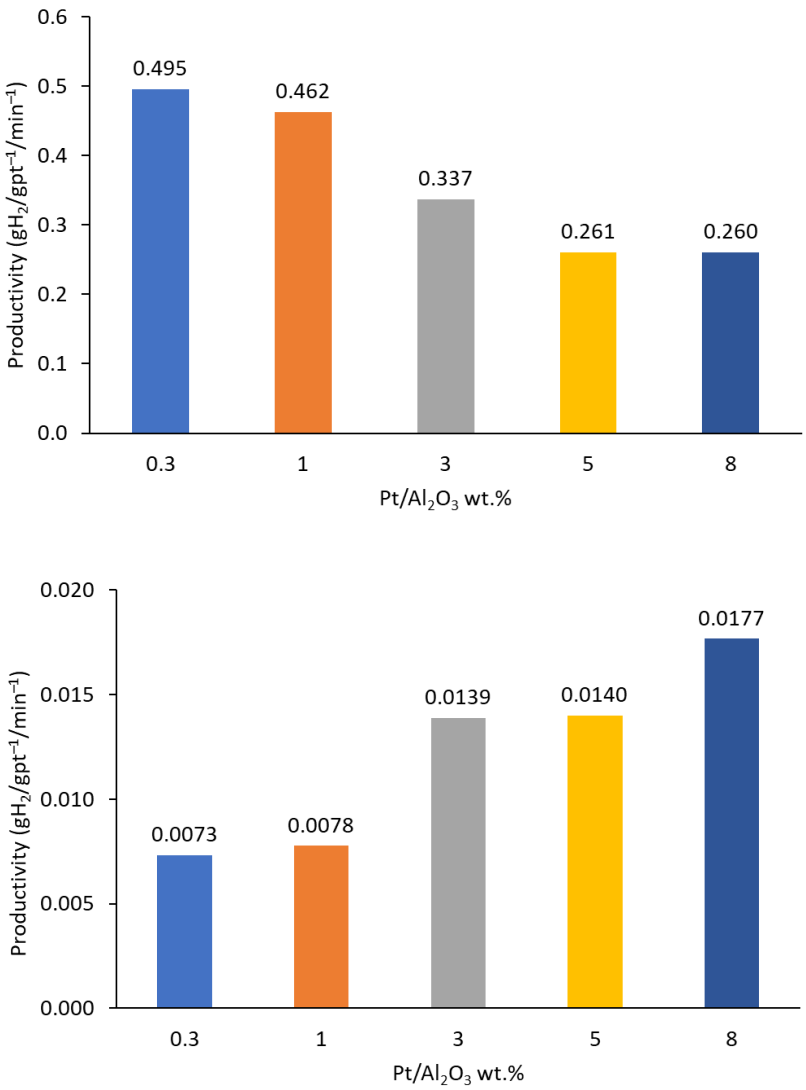

Figure 4.16. Peak productivity for Pt/γ-Al_2O_3 catalysts (0.3–8 wt.%). Upper: using a constant Pt amount (0.12 mol%); Lower: using a constant Pt/γ-Al_2O_3 catalyst amount (0.2 g). Process conditions: 4 h, 10 mL BT, 270 °C.

The DOD obtained Pt/γ-Al_2O_3 catalysts (0.3–8 wt.%) is shown in Figure 4.17, where the highest DOD obtained was 88% for 1 wt.% Pt/γ-Al_2O_3 in the upper graph. The DOD drops to 67% at 3 wt.% and declines further to 56% and 54% for 5 wt.% and 8 wt.% respectively. These results show that when the Pt amount is kept constant the best DOD is achieved using 1 wt.%. However, practicality issues prevent 1wt.% from being a viable option as the coating thickness needed to achieve 0.12mol% is unreliable and cracks off the SS support. In the lower graph the catalyst amount is kept constant and the highest DOD achieved is 65% for 8 wt.%, followed by 56% and 54% for 5 wt.% and 3 wt.% respectively. The DOD drops to 17% for 0.3 wt.%. These results show the importance of Pt/LOHC ratio and the effect it has on dehydrogenation performance. The 8 wt.% catalyst was not explored further due to the

expensive costs associated with Pt and trying to minimise costs for the feasibility of this setup.

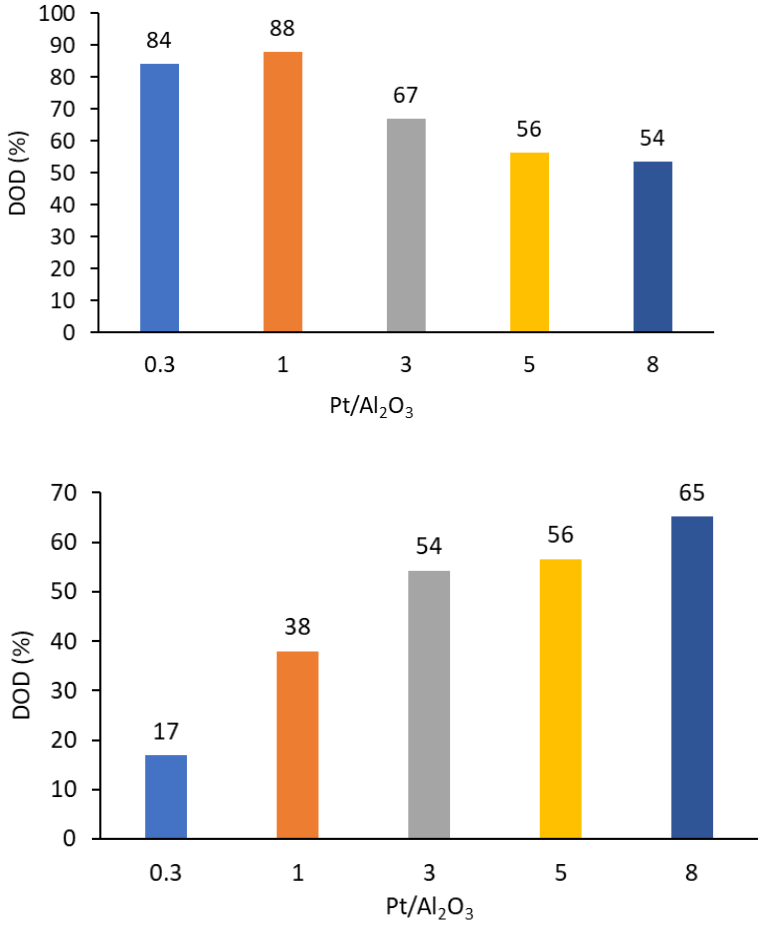

Figure 4.17. DOD achieved for Pt/γ-Al_2O_3 catalysts (0.3–8 wt.%). Upper: using a constant Pt amount (0.12 mol%); Lower: using a constant catalyst amount (0.2 g). Process conditions: 4 h, 10 mL BT, 270 °C.

This trend is further supported in Figure 4.18, showing the cumulative hydrogen yield. When maintaining constant Pt (left), the lower Pt loadings (0.3 wt.% and 1 wt.%) result in increased hydrogen productivity, with a peak at 1 wt.%, after which the efficiency decreases. This decrease is a direct result of fewer active sites available at higher Pt loadings. The dispersion decreases due to the high concentration of Pt, which causes the Pt to clump together, thus reducing the catalytic efficiency overall.

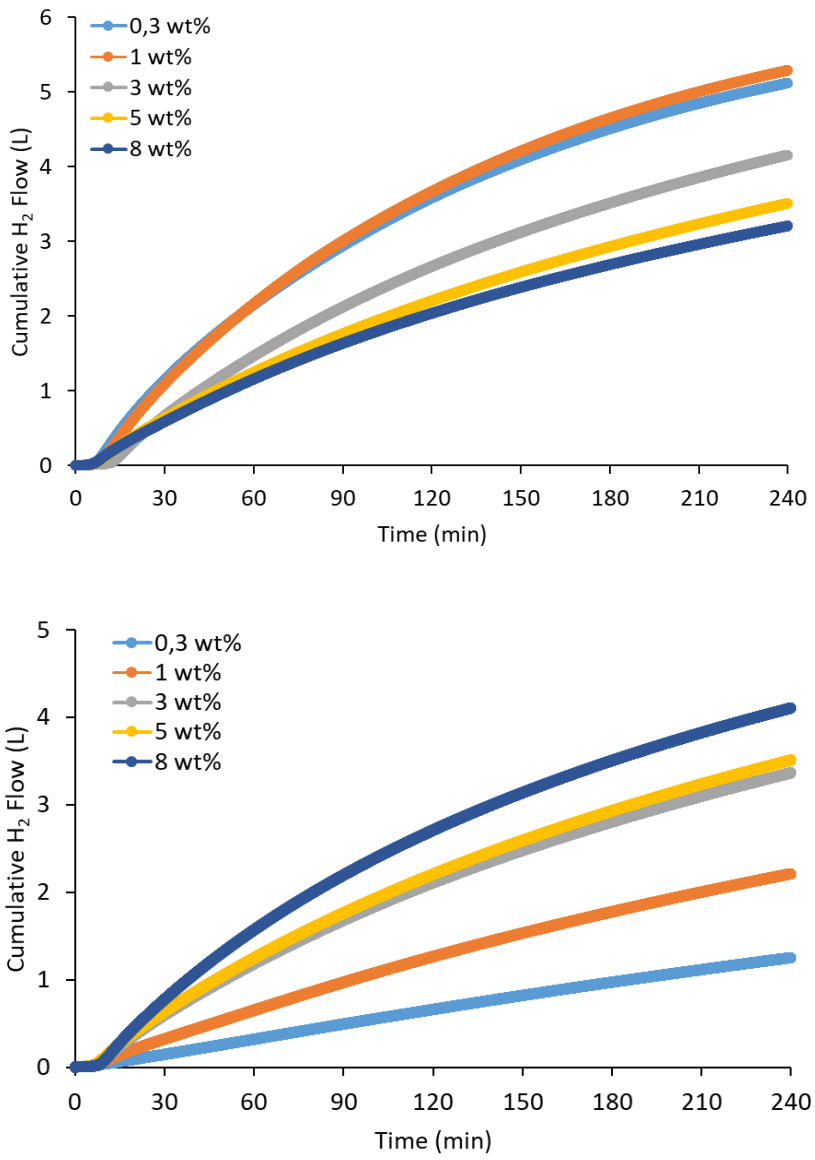

Figure 4.18. Cumulative H_2 flow for Pt/γ-Al_2O_3 catalysts (0.3–8 wt.%). Top: using a constant Pt amount (0.12 mol%); bottom: using a constant catalyst amount (0.2 g). Process conditions: 4 h, 10 mL BT, 270 °C.

The molar fraction distribution of BT is given in Figure 4.19 showing H12-BT, H6-BT, HBT and the by-product m-fluorene for across Pt/γ-Al_2O_3 catalysts (0.3–8 wt.%). When the platinum amount is kept constant H12-BT decreases at Pt loadings increases, where 0.3 wt.% converts the least H12-BT to H6-BT or HBT and 8 wt.% showing the lowest molar fraction for H12-BT and the highest molar fraction of HBT.

On the right where the catalyst amount is kept constant, 0.3 wt.% shows the highest molar fraction of HBT and lowest fraction of H12-BT. The molar fraction of H12-BT increases with increasing Pt loading and the molar fraction of HBT decreases with increasing Pt loading.

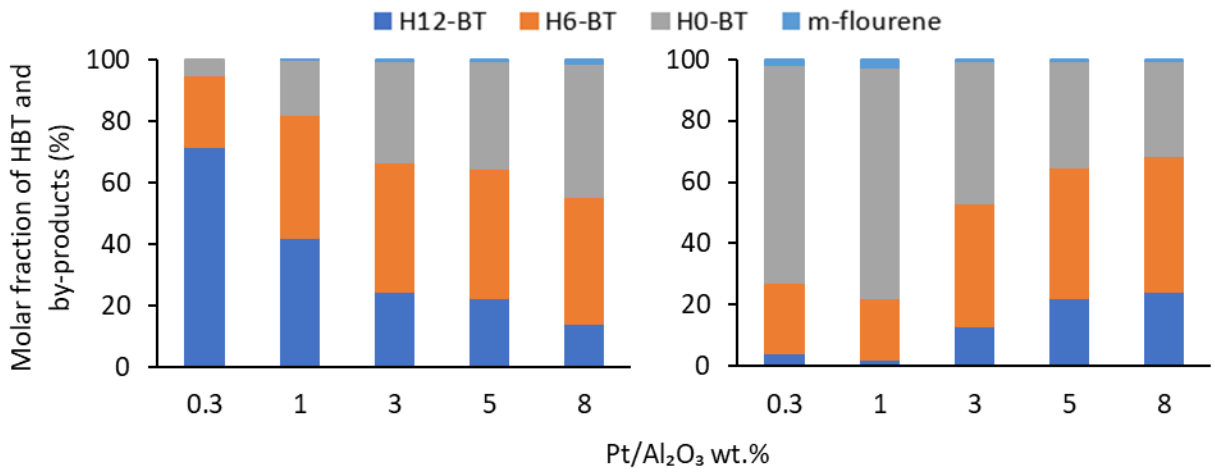

Figure 4.19. Molar fraction of HBT and by-products for Pt/γ-Al_2O_3 catalysts (0.3–8 wt.%). Left: using a constant Pt amount (0.12 mol%); right: using a constant catalyst amount (0. 2 g). Process conditions: 4 h, 10 mL BT, 270 °C.

4.5 Evaluation of Catalyst Performance: Different Washcoat Binders

4.5.1 Evaluation of different washcoat binders at constant Pt/γ-Al_2O_3 concentration and the coating thickness

Various washcoat binders were investigated to determine the effects of binder type and molecular weight on catalyst coating performance. When using a constant Pt/γ-Al_2O_3 concentration and coating thickness. The catalytic performance was tested through the use of different binders: PVA 22000, PVA 89000–98000, PVP 55000 and PVP 360000. Both the productivity and cumulative flow were evaluated. The binders were added at a binder concentration of 0.5%. Further practical details/process conditions were as follows: 50 mL batch reactor, 270 °C, reaction time 80 min, 10 mL H12-BT (VH12-BT = 10).

PVP 55000 gave the highest hydrogen productivity, indicating superior catalytic performance. PVP 360000, on the other hand, showed reduced productivity (0.14 gH_2/g_{Pt}/min), indicating that its higher molecular weight might impede mass transport or accessibility to the catalytic sites. A better balance between film stability and reactant mobility was achieved with the higher molecular weight (MW 89000–98000). PVA (MW89000-98000) binders performed better than their lower molecular weight counterpart (MW 22000) with a productivity of 0.21 gH_2/g_{Pt}/min as opposed to 0.18 gH_2/g_{Pt}/min.

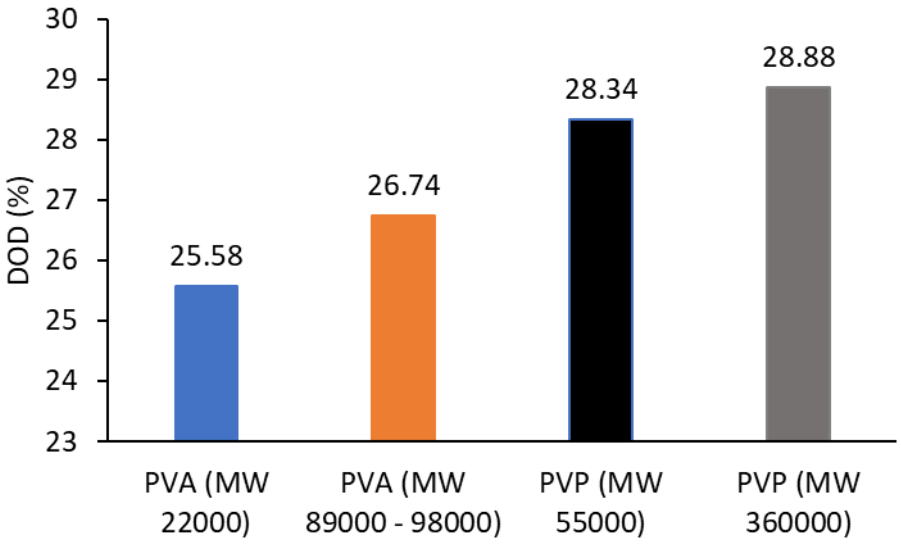

Figure 4.20. DOD for SS pellets coated with 5 wt.% Pt/γ-Al_2O_3 after dehydrogenation, using different binders. Process conditions: 50 mL batch reactor, T = 270 °C, reaction time = 80 min, VH12-BT = 10 mL, binder concentration 0.5 wt.%.

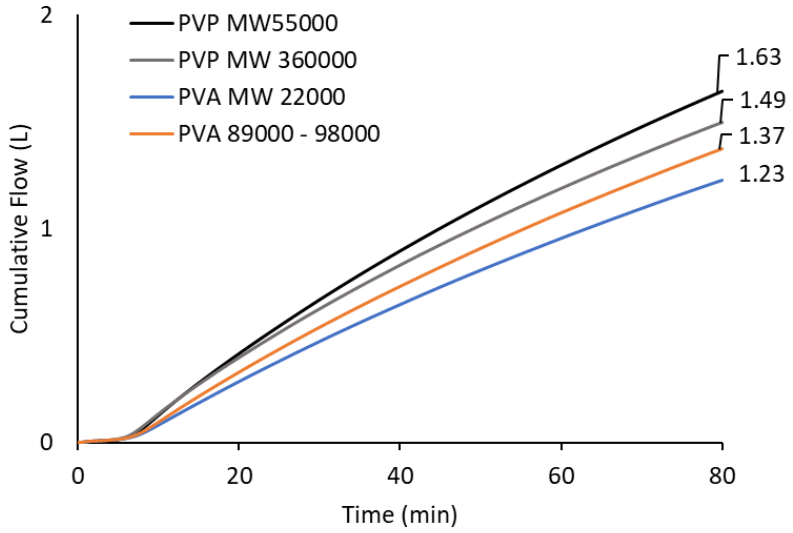

Figure 4.21. Cumulative flow for SS pellets coated with 5 wt.% Pt/γ-Al_2O_3 after dehydrogenation, using different binders. Process conditions: 50 mL batch reactor, T = 270 °C, reaction time = 80 min, VH12-BT = 10 mL, binder concentration 0.5 wt.%.

The productivity outcomes are supported by the cumulative flow trends, which show that PVP 55000 gave the highest hydrogen release over time, followed by PVP 360000, PVA 89000–98000 and PVA 22000. While PVP-based binders typically performed better than the PVA-based ones in terms of hydrogen evolution, the observed differences indicated that performance within each polymer type

is greatly impacted by molecular weight variations. The ideal viscosity and porosity properties of PVP 55000 that afford efficient gas diffusion may be the reason for its superior performance (Zahra *et al.*, 2024).

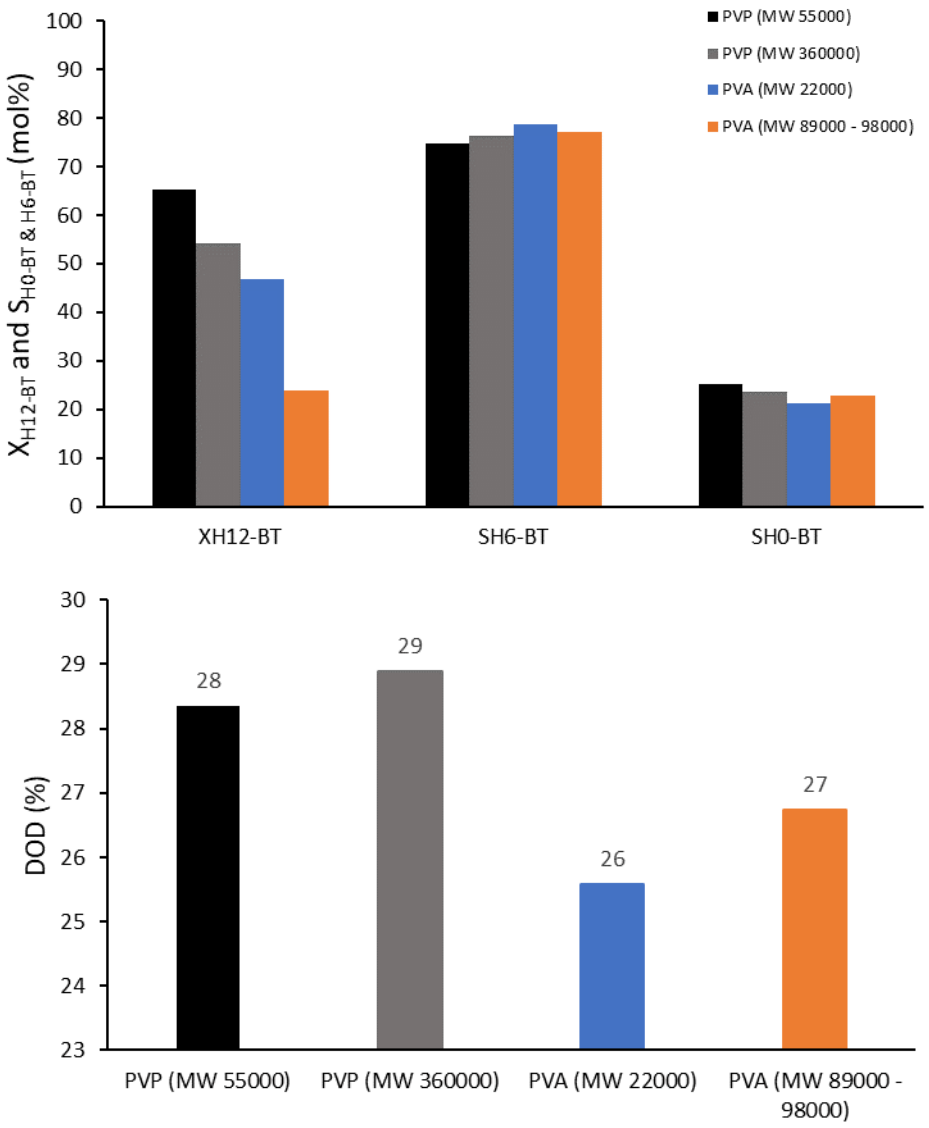

Figure 4.22. Conversion and selectivity (top) and DOD (bottom) for SS pellets coated with 5 wt.% Pt/Al_2O_3, after dehydrogenation, using different binders: (a) PVA 22000, (b) PVA 89000, (c) PVP 55 000, (d) PVP 360000. Process conditions: 50 mL batch reactor, T = 270 °C, reaction time = 80 min, VH12-BT = 10 mL, binder concentration 0.5 wt.%.

PVP 55000 achieves the highest conversion of 65% while PVA 89000–98000 gives the lowest (24%). See Figure 4.22 (top). This suggests that the binder selection has a significant impact on catalytic efficiency. The similar performance of all binders in SH6-BT (75%–79%) indicates that the binder effects are minimal in terms of selectivity for the reaction. The selectivity towards HBT presents a

narrow difference, suggesting that binder influence decreases as the reaction proceeds.

Figure 4.22 (bottom) shows the DOD trend: PVP 360000 exhibits the highest DOD of 29%, while PVP 55000 has a DOD of 28%; this implies that PVP promotes better hydrogen evolution. The difference in results between the PVP molecular weights suggests that reactant diffusion is hindered by a high viscosity (such as PVP 360000). PVA binders give a lower DOD, suggesting a stronger bond with the catalyst or substrate, which could limit access to the active site.

Table 4.5. Productivity, max flow, cumulative flow, and average power (P) of various binders, after dehydrogenation. Process conditions: 50 mL batch reactor, T= 270 °C, reaction time = 80 min, VH12-BT = 10 mL, binder concentration 0.5 wt.%.

Binders	**n_{Pt}/n_{H12-BT} (mol%)**	**Max flow (mL/min)**	**Max P_avg (W)**	**Productivity ($gH_2gPt^{-1}min^{-1}$)**	**Cumulative Flow (L)**
PVP 55000	0,123	35,04	83,39	0,25	1.63
PVP 360000	0,119	18,128	72,11	0,14	1.49
PVA 22000	0,117	23,968	74,38	0,18	1.37
PVA MW 89000–98000	0,118	27,808	74,15	0,21	1.23

Additional information about the effects of molecular weight and binder type on dehydrogenation performance is given in Tables 4.6 and 4.7. The superior catalytic efficiency of PVP 55000 is further supported by data in Table 4.6—the highest productivity (0.25 gH_2/g_{Pt}/min) and cumulative flow (1.63 L) are achieved. Significantly, lower max flow (18.13 mL/min) and productivity (0.14 gH_2/g_{Pt}/min) were observed with PVP 360000, despite it having the highest DOD (29%) (see Table 4.7). This suggests that increased molecular weight may hinder gas evolution, possibly because of mass transfer limitations.

Table 4.6. Conversion, selectivity, and DOD obtained from various binders after dehydrogenation. Process conditions: 50 mL batch reactor, T = 270 °C, reaction time = 80 min, VH12-BT = 10 mL, binder concentration 0.5 wt.%.

Catalyst	Conversion (%)	Selectivity H6-BT	Selectivity HBT	DOD (%)
PVP 55000	65,39	74,73	25,27	28
PVP 360000	54,26	76,31	23,69	29
PVA 22000	46,69	78,69	21,31	26
PVA 89000–98000	23,85	77,07	22,93	27

PVA 22000 and PVA 89000–98000, on the other hand, exhibited intermediate productivity although they have the lowest conversion: 47% and 24%, respectively. PVA 89000–98000 achieved a marginally higher value (0.21 gH_2/g_{Pt}/min). Table 4.7 also shows that conversion rates differed greatly, with PVP 55000 showing the highest conversion (65%), even though selectivity trends were generally consistent across binders. This implies that the dynamics of hydrogen release and catalyst utilisation are significantly influenced by binder selection. According to the selectivity data, PVP with higher molecular weight gives marginally increased selectivity at the expense of lower hydrogen evolution performance. These findings highlight the necessity of maintaining molecular weight balance for ideal dehydrogenation kinetics, by highlighting the trade-off between binder adhesion, catalyst dispersion and diffusion constraints.

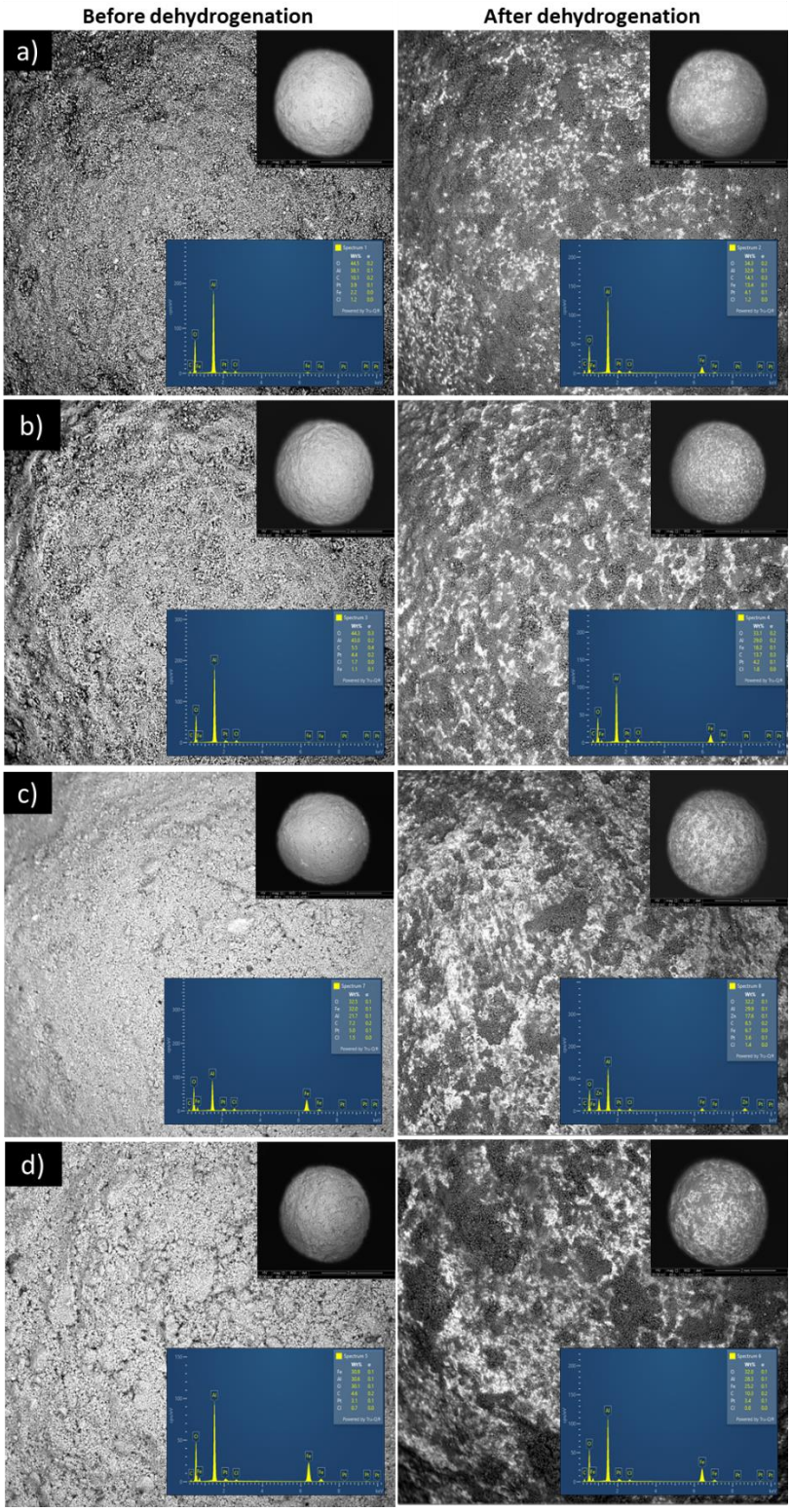

Figure 4.23. SEM-EDS analysis of SS pellets coated with 5 wt.% Pt/Al_2O_3, both pre- and post-dehydrogenation, using different binders: (a) PVA 22000, (b) PVA 89000-89000, (c) PVP 55000, (d) PVP 360000. Process conditions: 50 mL batch reactor, T = 270 °C, reaction time = 80 min, VH12-BT = 10 mL, binder concentration 0.5 wt.%.

SEM-EDS analysis indicated significant differences in the elemental distribution and surface morphology of SS pellets coated with 5 wt.% Pt/Al_2O_3. The surface shown in Figure 4.23a shows a comparatively uniform coating, with few to no catalyst clusters on the surface. Moderate roughening is evident after dehydrogenation, suggesting moderate adhesion and binder stability. As seen in Table 4.7, PVA 89000 gives the lowest hydrogen conversion. Figure 4.23b shows a more noticeable surface roughness after dehydrogenation, which could lead to intermediate productivity levels. This suggests that a thicker less homogeneous coating caused by PVA with a higher molecular weight would impede mass transport. This is supported by research carried out by Liang *et al.*; they showed that higher molecular weight PVA forms denser and more entangled networks due to longer polymer chains, which can result in thicker coatings with less uniformity. This denser network structure enhances mechanical strength but can also restrict diffusion pathways, thereby impeding mass transport (Liang *et al.*, 2024). The increased hydrogen productivity of PVP 55000 (0.26 gH_2/g_{Pt}/min) at 0.50 wt.% is attributed to a more uniform coating, with finely distributed Pt clusters (Figure 4.23c). This shows the best adhesion–diffusion balance and improved catalyst accessibility. The strong binder stability, which supports high cumulative hydrogen flow, is demonstrated by the slight morphological changes seen in post-dehydrogenation images.

In contrast, PVP 360000 (Figure 4.23d) shows notable clusters and non-uniform distribution, especially after dehydrogenation, indicative of limited mass transfer and poor binder dispersion (Liang *et al.*, 2024). The decreased productivity and cumulative flow is probably due to underscoring the negative effect that too high molecular weight has on catalytic activity.

The surface morphology of 5 wt.% $Pt/\gamma\text{-}Al_2O_3$ coated SS pellets prepared using the four different polymer binders is shown in Figure 4.24. A rougher texture is seen when using PVA MW 22000 (a) whereas a more uniform and smooth coating is seen when using PVA 89000 (b). Both samples (c) and (d) were prepared using PVP, with (d) showing the most consistent coating and uniformity.

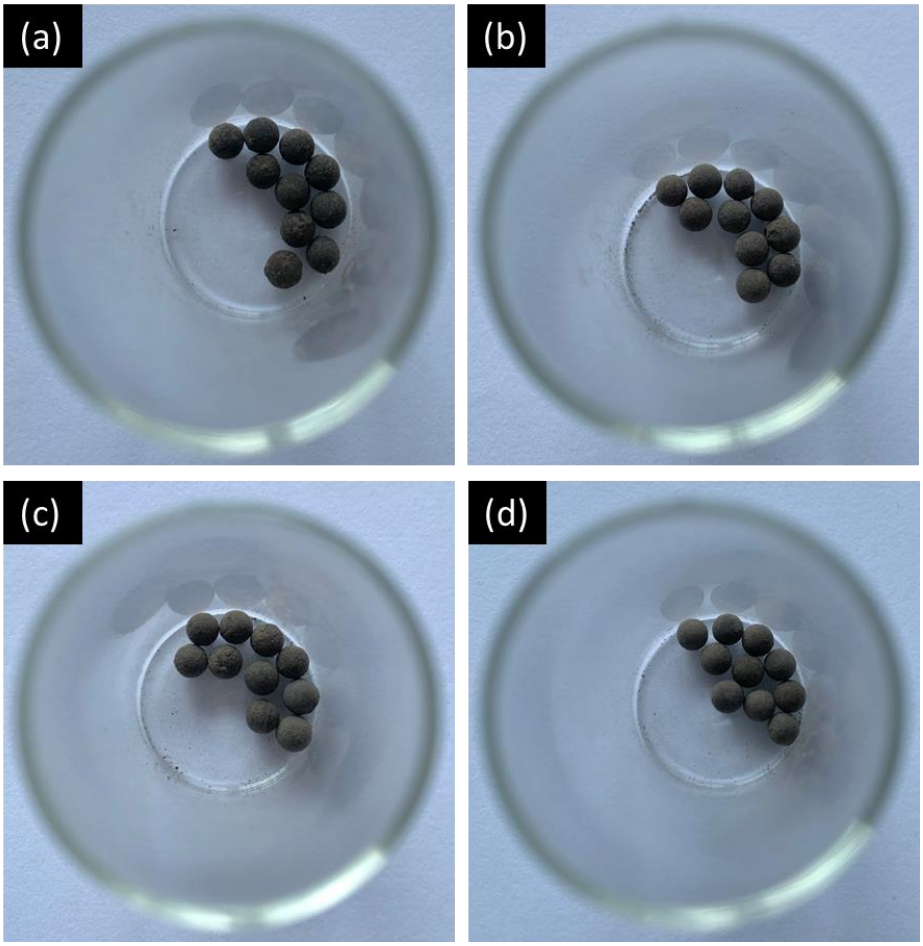

Figure 4.24. Photographs of 5 wt.% Pt/γ-Al_2O_3 coated SS pellets, with four different binders: (a) PVA 22000, (b) PVA 89000-98000, (c) PVP 55000, (d) PVP 360000.

4.5.2 Effect of binder concentration on catalytic activity

The effect of binder concentration on the catalytic activity of 5 wt.% Pt/γ-Al_2O_3 coated SS pellets, using PVP 55000 as the polymer binder, was also investigated. The binder concentration directly influences coating morphology, catalyst adhesion, active site exposure and ultimately the hydrogen evolution performance—hence. It is crucial to understand its role. A trade-off between adequate catalyst dispersion and preventing diffusion limitations brought on by an excess of binder layers was examined by methodically altering the binder concentrations.

Specifically, the following was investigated: how varying the concentration of PVP 55000 affected productivity, cumulative flow and catalytic performance of SS pellets coated with 5 wt.% Pt/γ-Al_2O_3 and PVP binder. Here, catalyst IDs have been assigned to each catalyst to facilitate reference to them. The catalyst IDs are as follows: Abb (0.25 wt.%), Acc (0.50 wt.%), Add (0.75 wt.%) and Aee (1.00 wt.%). These catalyst IDs are introduced in Table 4.8 (to facilitate the comparison of results between text and figures). Figure 4.25 shows the productivity and cumulative flow as a function of PVP binder

concentration (PVP 55000): 0.25–1 wt.%. The highest productivity was observed when using Acc 0.26 gH_2/g_{Pt}/min. The lower concentration of Abb showed reduced productivity (0.19 gH_2/g_{Pt}/min) and total volume of 1.11 L. Higher concentrations of Add and Aee showed a somewhat reduced productivity, the lowest being Aee, with 0.12 gH_2/g_{Pt}/min, due to diffusion limitations brought on by thicker binder layers that prevent reactants from reaching catalytic sites (Liang *et al.*, 2024).

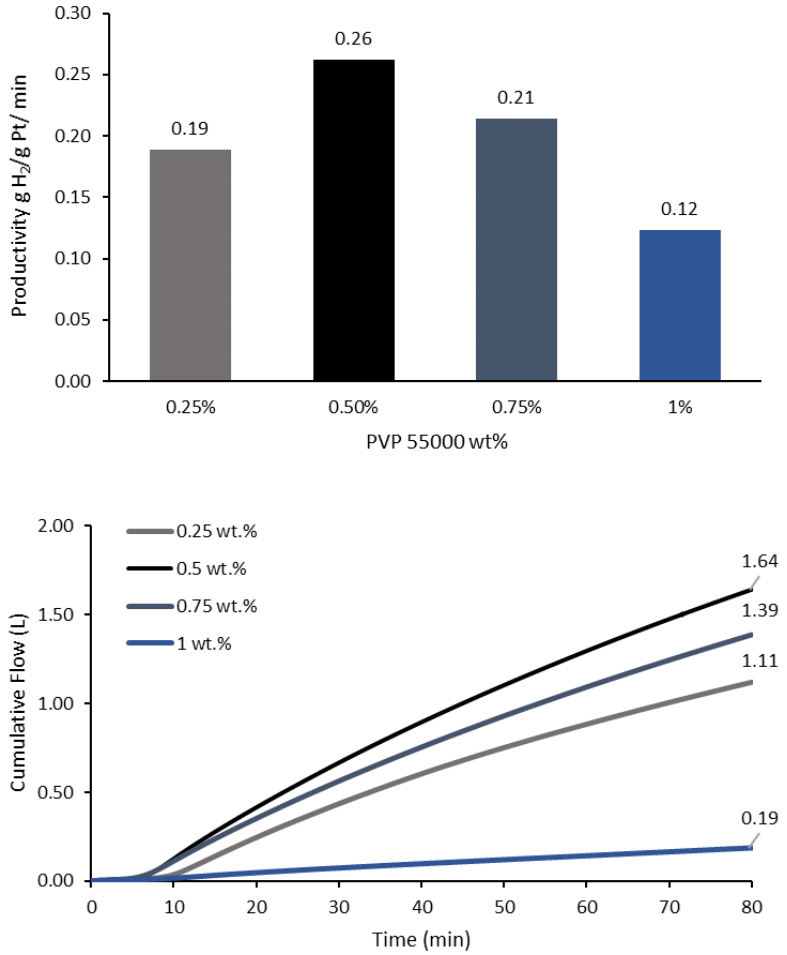

Figure 4.25. Hydrogen productivity (top) and cumulative flow (bottom) for SS pellets coated with 5 wt.% Pt/γ-Al_2O_3 before and after dehydrogenation, using different binder concentrations of PVP 55000 (0.25–1 wt.%). Process conditions: 50 mL batch reactor, T = 270 °C, reaction time = 80 min, VH12-BT = 10 mL.

Figure 4.26 illustrates the effect of binder concentration on the catalytic performance of 5 wt.% Pt/γ-Al_2O_3 coated SS pellets during dehydrogenation. The concentration of the binder has a significant impact on the DOD, conversion, and selectivity, by affecting the morphology of the coating and the dispersion of Pt. Abb, Add and Aee exhibited low conversion: 31%, 14% and 12%, respectively. The Acc is the only concentration exhibiting reasonably high conversion (65%) and selectivity for HBT

(25%), suggesting the optimal catalyst dispersion of active sites. The DODs observed for 0.5 wt.% and Add were similar: 28.3% and 27.8%, respectively. The overall low conversion and selectivity for Aee corresponds to the non-uniform coating and catalyst clusters seen in Figure 4.23d. This suggests that there is extensive binder coverage when using Aee, which obstructs catalytic sites and prevents good dehydrogenation. This tendency suggests that, although moderate binder concentrations promote efficient catalytic activity, excessive quantities reduce performance due to diffusion restrictions.

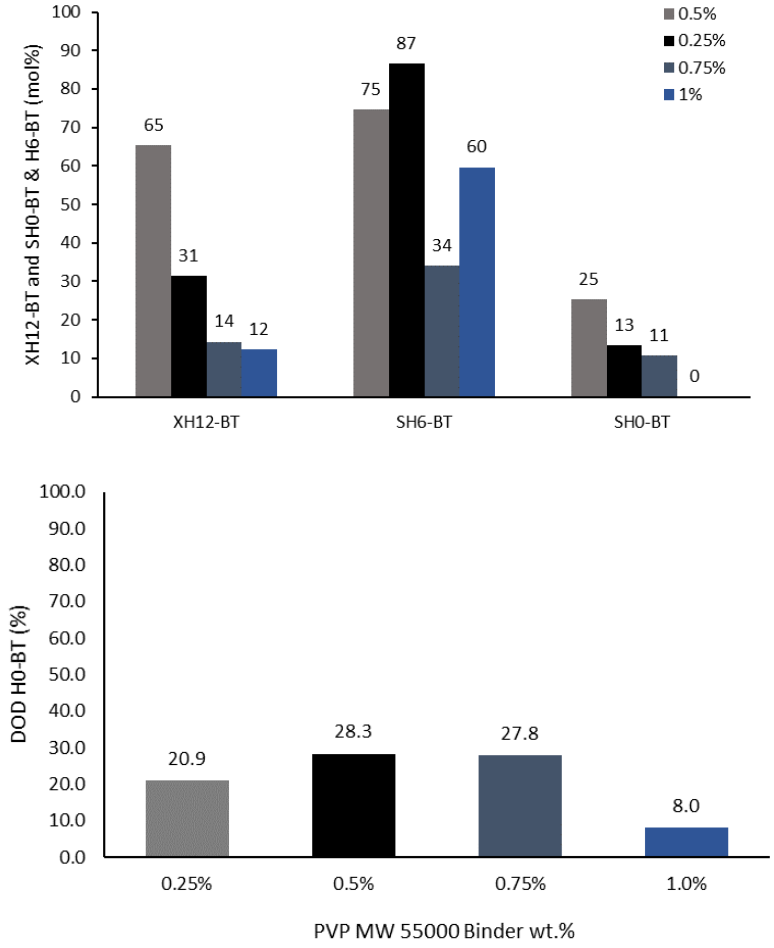

Figure 4.26. Conversion and selectivity (top) and DOD (bottom) of SS pellets coated with 5 wt.% Pt/γ-Al_2O_3 before and after dehydrogenation, using different binder concentrations of PVP 55000 (0.25–1 wt.%). Process conditions: 50 mL batch reactor, T = 270 °C, reaction time = 80 min, VH12-BT = 10 mL.

The rate constant (k), initial rate of reaction (r), and turnover frequency (TOF) can be calculated using equations 4.1 and 4.2 (Sotoodeh *et al.*, 2012), using initial concentration of reactant (C_0), molecular weight of platinum (MW_{Pt}), platinum loading (M_{Pt}), and dispersion (D). TOF is calculated to estimate the number of active sites involved in the reaction for each catalyst.

$$r = k \times C_0 \quad \text{...(4.1)}$$

$$TOF = \frac{K \times MW_{Pt} \times C_0}{M_{Pt} \times D} \quad \text{...(4.2)}$$

Table 4.8 shows the productivity, maximum flow, cumulative flow, and P at various PVP 55000 concentrations during dehydrogenation. Acc achieved the highest flow (35. 04 mL/min) and productivity (0.26 gH_2/g_{Pt}/min) during dehydrogenation of H12-BT; it showed good catalytic efficiency, from better catalyst dispersion and accessibility of active sites. Acc showed the highest TOF (59.80 min^{-1}), indicating that it offers the most efficient utilisation of active sites. Add had a lower TOF (48.28 min^{-1}), suggesting that while the catalyst is still effective, its lower Pt dispersion reduces its efficiency compared to Acc. Add had an average TOF of 43.65 min^{-1}, while Aee had the lowest TOF (27.61 min^{-1}), indicating poor active site utilisation. This can be attributed to larger Pt particles and diffusion limitations from excessive binder concentration, reducing the catalyst's overall efficiency (Xie *et al.*, 2020).

Table 4.7. Productivity, max flow, cumulative flow, P and TOF for various concentrations of PVP binders after dehydrogenation. Process conditions: 50 mL batch reactor, T= 270 °C, reaction time = 80 min, V_{H12-BT} = 10 mL.

Catalyst ID	PVP 55000 (wt.%)	n_{Pt}/n_{H12-BT} (mol%)	Pt amount (g)	Max flow (mL/min)	Max P_avg (W)	Productivity ($gH_2gPt^{-1}min^{-1}$)	Cumulative flow (L)	TOF (min^{-1})
Abb	**0,25**	0,1177	0,01179	24,89	78,72	0,19	1.11	43.65
Acc	**0,50**	0,1193	0,01195	35,04	83,39	0,26	1.64	59.80
Add	**0,75**	0,1267	0,01269	30,38	74,71	0,21	1.39	48.28
Aee	**1,00**	0,1195	0,01197	10,24	80,07	0,12	0.19	27.61

This trend is supported by dispersion measurements, which show that the metal dispersion is higher at lower Pt loadings (65.64% for 0.3 wt.%), resulting in smaller particle sizes (1.73 nm for CO chemisorption and 1.11 nm for TEM). In contrast, Aee yields the lowest productivity (0.12 gH_2/g_{Pt}/min) and a markedly decreased maximum flow rate (10.24 mL/min). Diffusion limitations brought on by high binder coverage that prevent reactants from reaching catalytic sites are the cause of this decrease. The cumulative flow decreases from 1.64 L to 0.19 L from Acc to Aee, confirming the detrimental effect that high binder concentration has on the evolution of hydrogen.

The effects of PVP concentration on conversion, selectivity and DOD are further detailed in Table 4.9. At Acc, the maximum conversion (65.39%) is achieved, which is in agreement with the peak productivity in Table 4.8. Selectivity towards H6-BT is 74.73% at 0.75 wt.% PVP (MW 55000), whereas selectivity towards HBT is 25.27%, suggesting effective dynamics of hydrogenation and dehydrogenation. The hydrogenation step (from H12-BT to H6-BT) is the step that determines the rate of this reaction, as evidenced by the higher selectivity towards H6-BT at Acc. The comparatively low selectivity towards HBT (25.27%) in contrast to the high selectivity for H6-BT indicates that there is limited dehydrogenation activity at this stage, preventing the complete conversion to HBT.

Table 4.8. Conversion, selectivity, and DOD obtained from various concentrations of PVP binders after dehydrogenation. Process conditions: 50 mL batch reactor, T = 270 °C, reaction time = 80 min, VH12-BT = 10 mL.

Catalyst ID	PVP MW55000 (wt.%)	Conversion (%)	Selectivity H6-BT	Selectivity HBT	DOD %
Abb	**0,25**	31,46	86,56	13,44	20,87
Acc	**0,50**	65,39	74,73	25,27	28,34
Add	**0,75**	3,99	75,20	24,40	27,83
Aee	**1,0**	12,40	94,45	0	3,44

With Aee, the H12-BT conversion falls to 12.40% and the HBT selectivity is zero. This is supported by results of Romero *et al*., demonstrating how the catalytic performance of Pt/PVP catalysts is hindered by high binder concentrations caused by leftover PVP breakdown products. As residues fill micropores and block active sites, a higher PVP content significantly reduces the Bronsted acid sites and pore accessibility, according to IR spectroscopy and textural analysis. The Pt/PVP sample with the highest PVP concentration demonstrated very low conversion at 673K. Catalytic activity measurements also showed that catalysts with higher PVP residuals have significantly lower n-hexadecane conversion rates (Romero *et al.*, 2022). Thus, lingering PVP residues impair hydrogen release and deactivate or block active sites, which ultimately reduces the catalyst efficiency in hydrocracking procedures.

With Acc, the DOD peaks at 28.34%, showing the best possible balance between conversion and selectivity, while at Aee the DOD is at its lowest (3.44%), thereby validating diffusion constraints. The

PVP concentration has a significant impact on dehydrogenation performance, as these results demonstrate. Although moderate concentrations (Acc) do improve flow productivity and DOD, because of diffusion limitations, however, excessive amounts hinder catalytic efficiency.

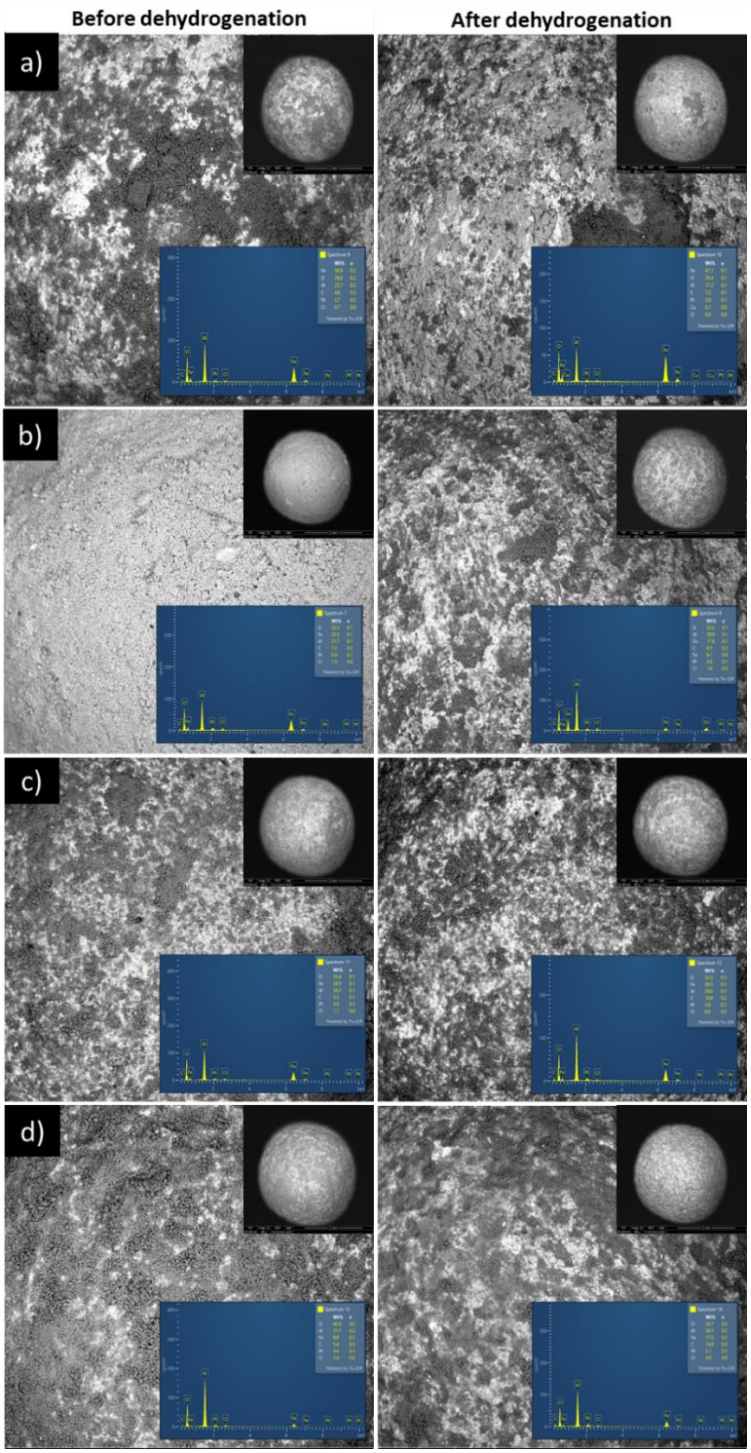

Figure 4.27. SEM-EDS of SS pellets coated with 5 wt.% Pt/γ-Al_2O_3 before and after dehydrogenation, using different binder concentrations of PVP 55000: (a) Abb, (b) Acc, (c) Add, (d) Aee. Process conditions: 50 mL batch reactor, T= 270 °C, reaction time = 80 min, VH12-BT = 10 mL.

Figure 4.27 shows the SEM-EDS images for SS pellets coated with carrying 0.25wt.%, 0.5wt.%, 0.75wt.% and 1wt.% of PVP 55000 and 5 wt.% Pt/γ-Al_2O_3 before and after dehydrogenation. Figure 4.27a shows that the coating is not uniformly distributed—a few clusters are seen on the surface. This suggests that the Acc concentration is too low to allow for adequate catalytic adhesion on the surface of the SS pellet. Surface roughening is visible in post-dehydrogenation images, indicating minimal binder stability and adhesion. The lower productivity (0.19 gH_2/g_{Pt}/min) and cumulative flow (1.11 L) for Abb shown in Table 4.8 are consistent with Figure 4.27, suggesting that active site exposure and catalytic efficiency are restricted by insufficient binder concentration (Romero *et al.*, 2022). PVP aids in the distribution of the Pt/γ-Al_2O_3 the over the SS pellet and functions to retain the coating on the SS pellets, to maximise the heating between the LOHC and the catalyst.

According to Figure 4.27b, Acc demonstrates the ideal catalytic adhesion and dispersion—the coating looks more homogeneous and finely distributed prior to dehydrogenation. Effective diffusion pathways and high binder stability are demonstrated by the minimal morphological changes following dehydrogenation. This aligns with data in Table 4.8, with the highest productivity (0.26 gH_2/g_{Pt}/min). The ideal balance between catalyst coverage and active site accessibility promotes effective hydrogen evolution and is responsible for improved performance. In contrast, Figure 4.27c is less uniform, with more noticeable clustering both before and after dehydrogenation. Diffusion limitations and decreased active site exposure are suggested by increased clustering—these factors translate into lower productivity (0.21 gH_2/g_{Pt}/min).

Figure 4.27d suggests that increased binder concentrations impair mass transfer and alter the kinetics of hydrogen release. Results for Aee indicate non-uniform surface morphology and significant catalyst clusters. Following dehydrogenation, significant cluster formation and roughening suggest inadequate binder dispersion and significant diffusion constraints. This correlates with the lowest productivity (0.12 gH_2/g_{Pt}/min) and cumulative flow (0.19 L). Taken together, these morphological findings support the idea that catalyst distribution, active site exposure and diffusion kinetics are significantly impacted by the binder concentration (Romero *et al.*, 2022). Therefore, maximising hydrogen production and preserving catalytic efficiency during dehydrogenation depend on maintaining an ideal binder concentration.

EDS analysis revealed significant differences in elemental distribution across various PVP binder concentrations for coated SS pellets. The sample with the lowest PVP concentration (Abb) had the most noticeable characteristic peaks for the SS substrate, suggesting that the coating coverage was

incomplete; the substrate signals were the highest, with Fe registering ~28 wt.% and Cr ~15 wt.%, with only 1.8 wt.% Pt present. These substrate signals gradually decreased as the PVP concentration increased, al through samples Acc to Aee showed improved coating thickness and homogeneity.

In sample Acc, with moderate PVP concentration, coating integrity was increased, with decreased Fe and Cr contributions from the substrate below 15 wt.%, while the Pt content was maintained at 2.5 wt.%—thus suggesting a catalyst layer that is better preserved. Samples Add and Aee, which had the highest binder concentrations, gave an increased Al and O signals from the Al_2O_3 support, reaching up to 22 wt.% combined; the Pt content was marginally reduced to 2.2 wt.%. This indicates that an excessive concentration of binder could partially obscure the catalytic active sites, whilst improving film uniformity.

Productivity peaked with Acc (0.5 wt.%) (see Table 4.8), with the highest hydrogen productivity of 0.26 $gH_2/gPt/min$ and cumulative flow of 1.64 L. At this binder concentration there is adequate reactant diffusion and balanced catalyst distribution. At Abb (0.25 wt.%), lower productivity was 0.19 $gH_2/gPt/min$ and cumulative flow 1.11 L, which aligns with observations in Figure 4.27(a), showing non-uniform coating and minimal binder adhesion, thus indicating poor catalyst adhesion caused by insufficient binder coverage. Diffusion restrictions from thicker binder layers (Add and Aee) resulted in decreased productivity, 0.21 $gH_2/gPt/min$ and 0.12 $gH_2/gPt/min$, at higher concentrations. This correlates with results of SEM-EDS analysis, which shows increased clustering and non-uniform coating. It was evident that Acc (0.50 wt.%) produced the most homogeneous coating with finely dispersed Pt clusters. PVP contributes to maintaining a steady cumulative flow and high productivity. The stability of the binder and catalytic efficiency depend on maintaining the ideal coating thickness. Coating thickness directly affects catalyst distribution, adhesion, and diffusion kinetics.

4.6 Evaluation of Catalyst Performance: Various Coating Thicknesses

The productivity, DOD, H_2 yield, and molar fractions of hydrogenated by-products were examined to assess the effect of coating thickness on the performance of Pt/γ-Al_2O_3 catalysts. Two distinct platinum loadings (3 wt.% and 5 wt.%) were used in the experiments on SS pellets with different coating thicknesses (62 μm, 81 μm, 100 μm and 125 μm) to evaluate the effects of these variables on catalytic activity and efficiency. There is a notable difference between the two loadings. Productivity for 3 wt.% coated SS pellets shows a slight increase as the coating thickness increases from 62 μm to 81 μm, but a sharp decline after 100 μm, indicating that too thick a coating hinders catalytic efficiency due to diffusion limitations (Hart *et al.*, 2020c). Conversely, when coated with 5 wt.%, a more noticeable peak is seen at 81 μm, followed by a decline.

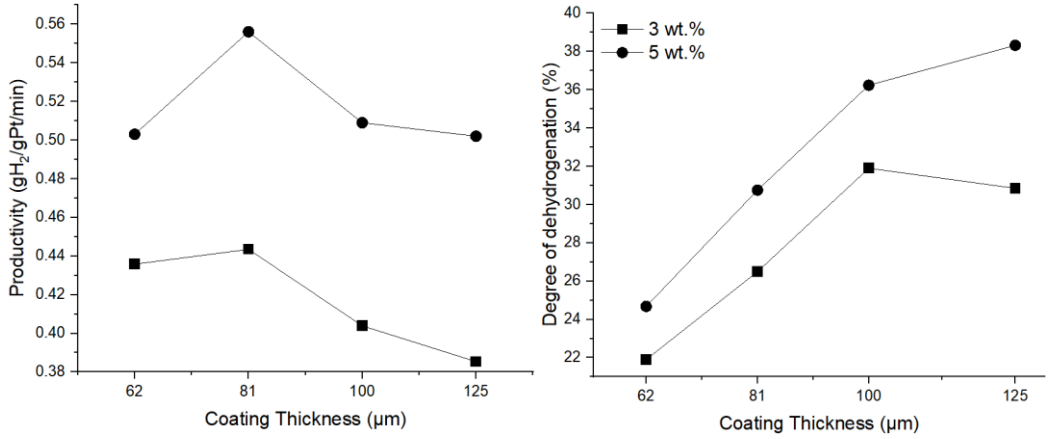

Figure 4.28. Comparison of the productivity (left) and DOD (right) for Pt/γ-Al_2O_3 (3 and 5 wt.%), with four different coating thickness (62 μm, 81 μm, 100 μm, 125 μm) on SS pellets. Process conditions: 50 mL batch reactor, T= 270 °C, reaction time = 120 min, VH12-BT = 10 mL.

The DOD trend differs. Both loadings show a noticeable increase in DOD, with the 5 wt.% outperforming the 3 wt.%. This implies that, although thicker coatings limit active site availability, the higher platinum loading partially offsets the effect of thicker coatings and reduced active site accessibility. The trade-off between catalytic activity and diffusion resistance is highlighted by the difference between productivity and dehydrogenation efficiency, underscoring the necessity of selecting the ideal coating thickness.

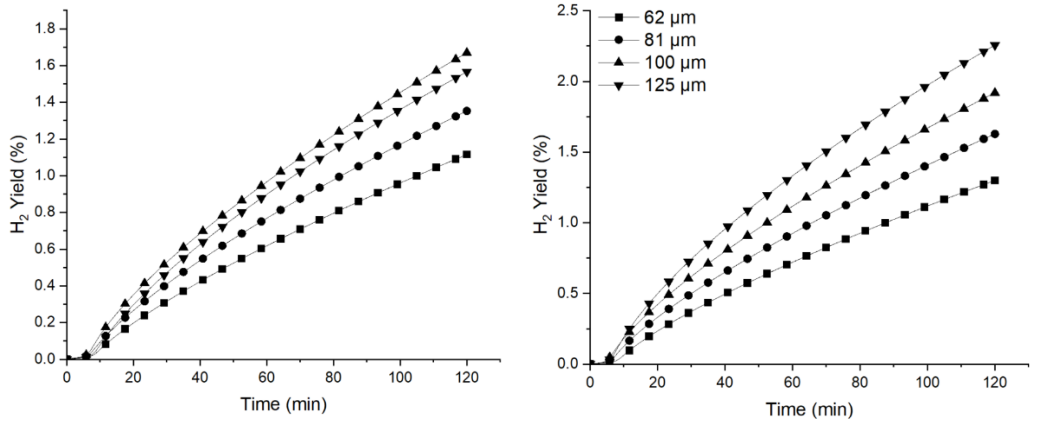

Figure 4.29. Comparison of H_2 yield obtained for 3 wt.% Pt/γ-Al_2O_3 (left) and 5 wt.% Pt/γ-Al_2O_3 (right), with four different coating thickness (62 μm, 81 μm, 100 μm, 125 μm) on SS pellets. Process conditions: 50 mL batch reactor, T= 270 °C, reaction time =120 min, VH12-BT = 10 mL.

The trend seen in Figure 4.29 shows a relationship between the coating thickness and metal loading. As the coating thickness increases, the hydrogen yield increases for both catalyst loadings. For all four thicknesses, the 5 wt.% shows a more noticeable effect. More active sites are produced for a higher

metal loading and higher loadings overcomes diffusion limitations associated with thicker coatings. The yield–time profiles show a nearly linear trend, suggesting constant dehydrogenation kinetics. Thicker coatings maintain catalytic activity for a longer period due to improved thermal stability; this is supported by the increasingly clear separation between curves as the reaction proceeds. Notably, although both catalysts gain from thicker coatings, the 3 wt.% catalyst shows diminishing returns after 100 μm.

Solymosi *et al*. investigated the use of SS plates for the dehydrogenation of BT(H18-DBT)and report that the flat structure allows efficient heat transfer directly to the active sites (Solymosi *et al.*, 2021). The coating is applied directly onto the SS plate and reduces heat loss—improved thermal conductivity in comparison to pelletised catalysts was evident. These authors further stated that the coating thickness affects the active surface areas, with thinner coatings increasing the exposure to active sites, potentially enhancing activity and productivity, whereas thicker coatings could lead to diffusion limitations and reduced efficiency. The dip-coating process described leads to variations in the loadings, after adjusting the immersion parameters, implying that coating thickness directly impacts catalyst performance.

Figure 4.30 shows the fraction of H12-BT gradually decreases with increasing coating thickness for both catalysts, suggesting improved dehydrogenation. An increased coating thickness leads to a lower molar fraction of H12-BT. At lower coating thicknesses, there is a higher molar fraction of H12-BT, 57% and 63% at 62 μm and 81 μm, respectively, before decreasing to 49% and 51% at higher thicknesses.

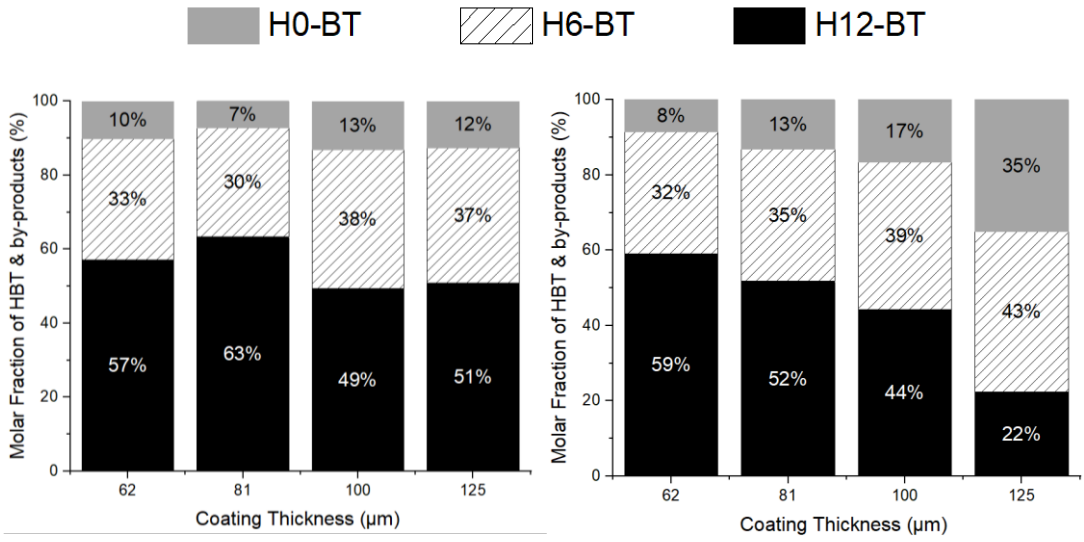

Figure 4.30. Comparison of molar fraction obtained for H12-BT, H6-BT and HBT for 3 wt.% Pt/γ-Al_2O_3 (left) and 5 wt.% Pt/γ-Al_2O_3 (right), with four different coating thicknesses (62 μm, 81 μm, 100 μm, 125 μm) on SS pellets. Process conditions: 50 mL batch reactor, T= 270 °C,

reaction time = 120 min, VH12-BT = 10 mL.

The DOD can be limited by thicker coatings because the latter impede diffusion and reduce catalytic efficiency. Thinner coatings, on the other hand, enable better diffusion, which may not be as effective in promoting deeper stages of dehydrogenation, however. This is further supported by the corresponding increase in H6-BT and HBT fractions, especially the increase in fully dehydrogenated HBT at 100 μm and 125 μm. A more noticeable shift in molar fractions is seen with the 5 wt.%, where the molar fraction of HBT increases with the coating thickness. At 125 μm, the molar fraction of H12-BT decreases to 22%, compared to the 51% obtained for 3 wt.%. Notably, by-products such as m-fluorene remain below 1%, suggesting few side reactions in which by-products are formed.

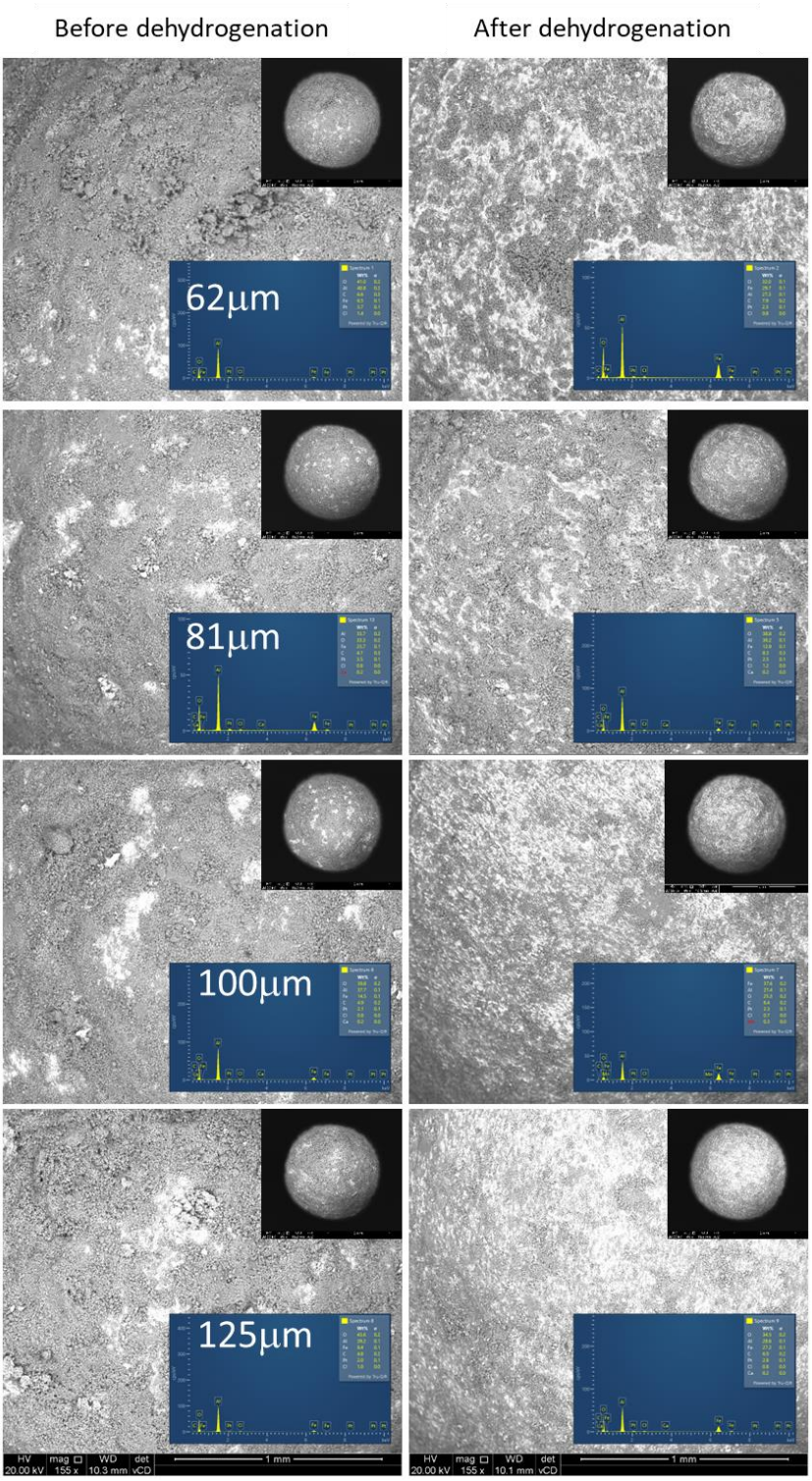

Figure 4.31. SEM-EDS of SS pellets coated with 3 wt.% Pt/γ-Al_2O_3 before and after dehydrogenation, using 0.5 wt.% PVP 55000, with increasing coating thickness (62 µm, 81 µm, 100 µm, 125 µm). Process conditions: 50 mL batch reactor, T = 260 °C, reaction time = 80 min, VH12-BT = 10 mL.

Analysis of SS pellets coated with 3 wt.% Pt/γ-Al_2O_3 before and after dehydrogenation shows clear morphological changes at the various coating thicknesses (62 μm, 81 μm, 100 μm and 125 μm). EDS spectra confirm the presence of Pt, Al, and O, and showed that the coatings appear uniform and well distributed prior to dehydrogenation. After dehydrogenation, there is little loss of elemental composition. As the coating thickness increases, to 100 μm and 125 μm, the surface becomes uneven and rough after dehydrogenation. Both the thicknesses 62 μm and 81 μm show better coating after dehydrogenation, with the 81 μm having the most even coating after dehydrogenation.

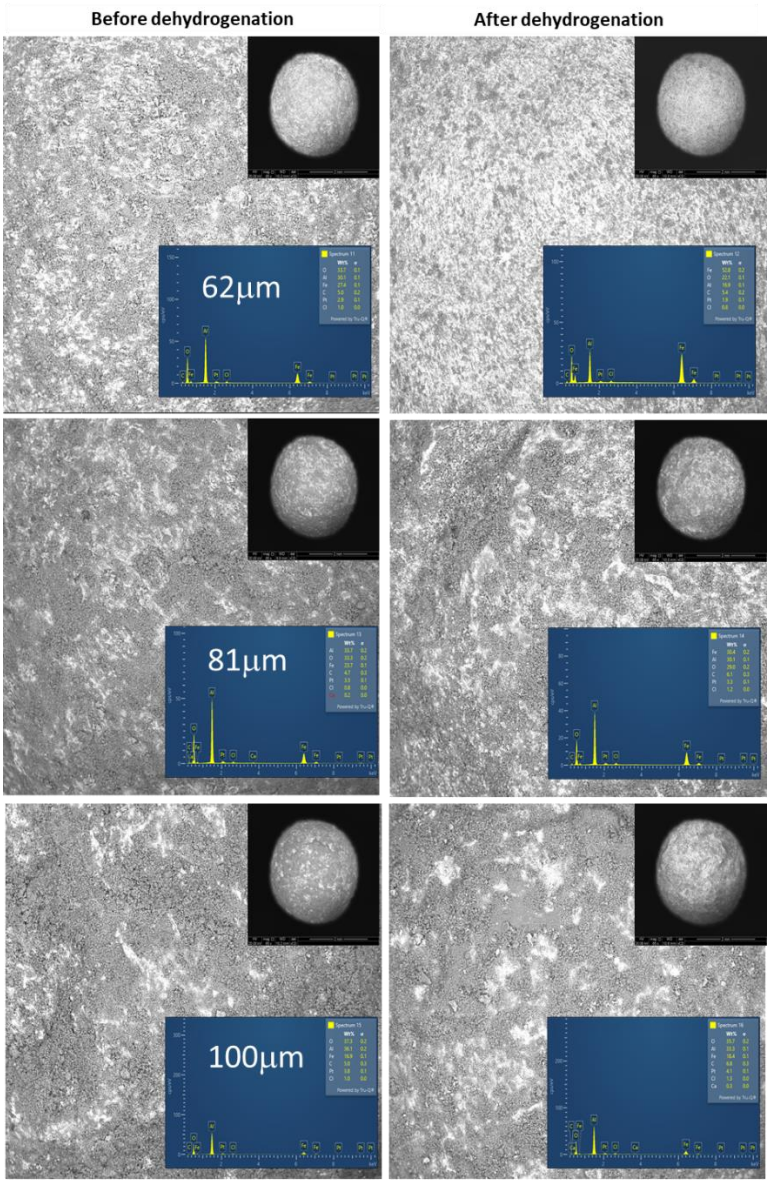

Figure 4.32. SEM-EDS of SS pellets coated with 3 wt.% Pt/γ-Al_2O_3 before and after dehydrogenation, using 0.5 wt.% PVP 55000, with increasing coating thickness (62 μm, 81 μm, 100 μm, 125 μm). Process conditions: 50 mL batch reactor, T= 260 °C, reaction time = 80 min, VH12-BT = 10 mL.

Figure 4.32 shows the SEM-EDS of SS pellets coated with 5 wt.% under the same conditions as in Figure 4.31. Prior to dehydrogenation, the coatings 62 μm, 81 μm, 100 μm and 125 μm are relatively uniform while after dehydrogenation, the surface coatings are non-uniform and rough spots without catalyst are clearly seen. This is supported by the EDS which shows a lower percentage of Pt, Al, and O present.

Both the 3 wt.% and 5 wt.% catalysts showed similar trends for all four coating thicknesses. Thicker coatings (100 μm and 125 μm) show a decreased efficiency due to diffusion limitations, whereas the thinner coatings (62 μm and 81 μm) achieve higher hydrogen production rates. Similar trends were seen with the molar fractions, where the highest conversion is seen at intermediate coating thicknesses, whereas excessive coating thicknesses prevents reactant diffusion and catalyst utilisation. Successful dehydrogenation was confirmed by molar fraction analysis, which shows that 5 wt.% coated SS pellets exhibit a higher HBT molar fraction compared to the 3 wt.%. SEM-EDS images of Pt/γ-Al_2O_3 coatings at 3 wt.% and 5 wt.% show that increases in surface roughness intensify as the catalyst loading and thickness increase.

4.7 Catalyst Cycle Tests

The stability of the catalyst and the consequences of catalyst deactivation were determined by assessing the performance over several reaction cycles, specifically, over the course of four consecutive reaction cycles. The tests focused on the cumulative flow, DOD, productivity, and by-product formation. See Figure 4.33.

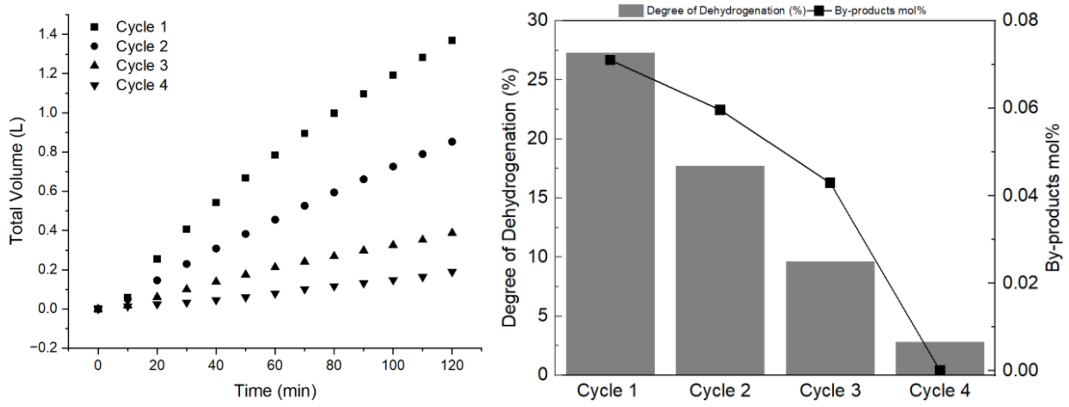

Figure 4.33. Cumulative flow (left) and DOD (right) over four cycle runs of dehydrogenation of H12-BT. Process conditions: 50 mL batch reactor, T= 270 °C, reaction time = 120 min, VH12-BT = 10 mL.

A progressive decline in gas evolution is seen for each cycle, with the maximum overall flow seen in cycle 1 (compared to in cycle 4). This indicates catalyst deactivation and coating deterioration over consecutive cycles. A similar trend is seen for the DOD over consecutive cycles: an initial DOD of 27%

at cycle 1 decreased to 3% by cycle 4. By-product formation exhibited a decreasing trend as the number of cycle runs increased, indicating that a catalyst's reduced activity restricts the occurrence of side reactions (usually linked to by-product formation). Decreased catalytic activity appears to have a direct impact on both primary and secondary reaction pathways, as indicated by the association between the decline in dehydrogenation efficiency and the formation of by-products.

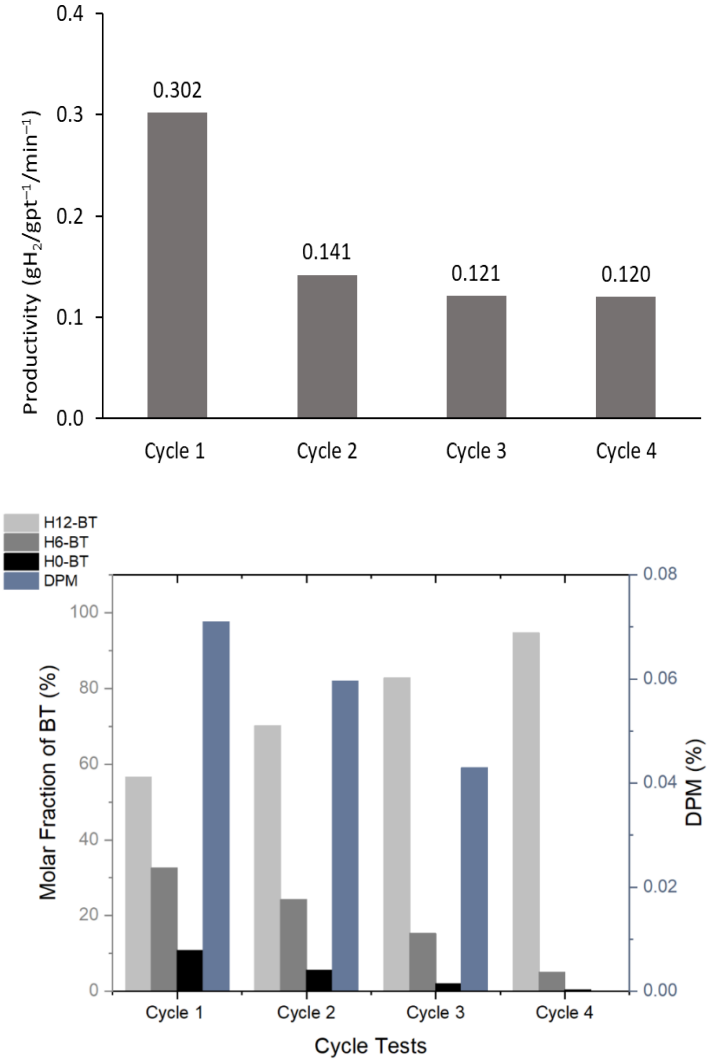

Figure 4.34. Productivity (above) and molar fraction percentages of BT, H6-BT and H12-BT (below) over four reaction cycles. Process conditions: 50 mL batch reactor, T= 270 °C, reaction time = 120 min, VH12-BT = 10 mL.

There is a noticeable drop in the productivity after cycle 1; it decreases from 0.302 gH_2/g_{Pt}/min to 0.141 in cycle 2 and ends at 0.120 in cycle 4. This decrease points to a progressive loss of the catalyst, most likely due to deactivation. This pattern is further supported by the molar fraction distribution of BT derivatives, which shows that the concentration of fully hydrogenated H12-BT decreases over the cycles, whereas the concentrations of partially hydrogenated H6-BT and unconverted HBT exhibit

comparatively steady or rising trends. Remarkably, diphenylmethane (DPM) is a minor by-product, especially in the earlier cycles, indicating that side reactions decrease as the catalyst activity declines. The observed changes in product selectivity therefore emphasise the relationship between catalyst stability and hydrogenation efficiency.

4.8 Kinetic Study of H12-BT Dehydrogenation: Effect of the Pt/□-Al_2O_3 Coating Thickness on Reaction Parameters

The influence of the Pt/γ-Al_2O_3 catalyst coating thicknesses (62 µm, 81 µm, 100 µm and 125 µm) on SS pellets was investigated in an inductive batch reactor to assess the impact on kinetic parameters, including the reaction rate, rate constant and TOF. The dehydrogenation experiments were conducted in an inductive batch reactor within the dehydrogenation temperature range 225–255 °C, with hydrogen conversion <70%, to minimise back reactions and transfer hydrogenation at high conversions (Wunsch *et al.*, 2018).

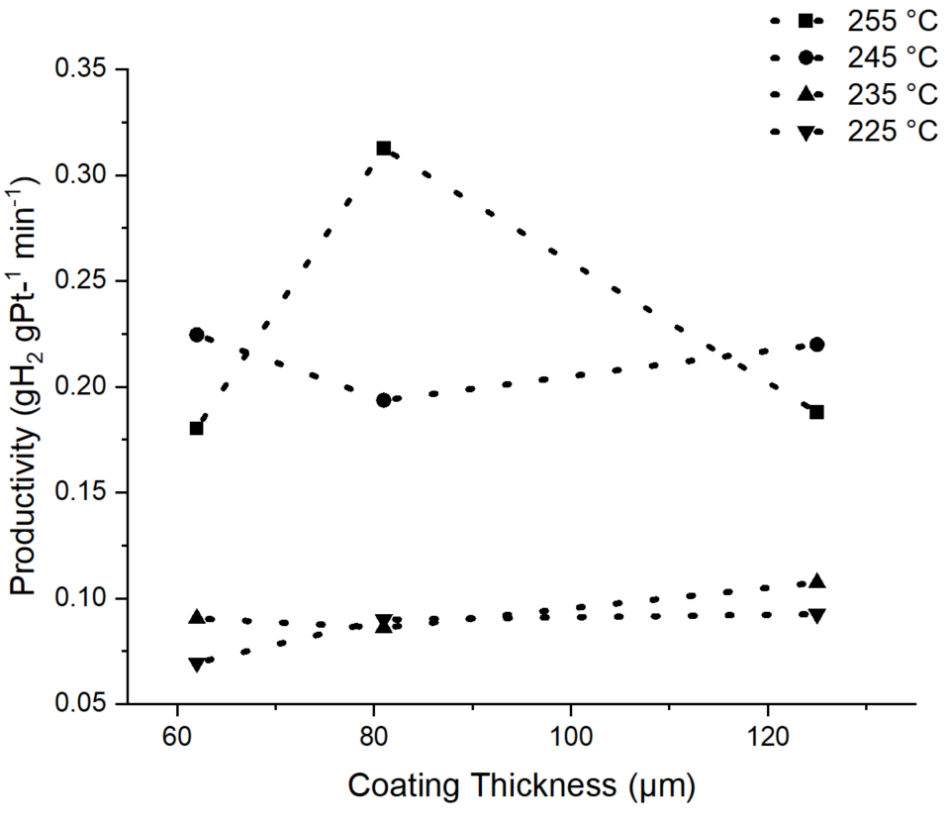

Figure 4.35. Productivity as a function of diffusion length for 5 wt.% Pt/γ-Al_2O_3 with three different coating thicknesses (62 µm, 81 µm, 125 µm) on SS pellets in an inductive batch reactor. Process conditions: 50 mL batch reactor, T= 225– 255 °C, reaction time =80 min, VH12-BT = 10 mL.

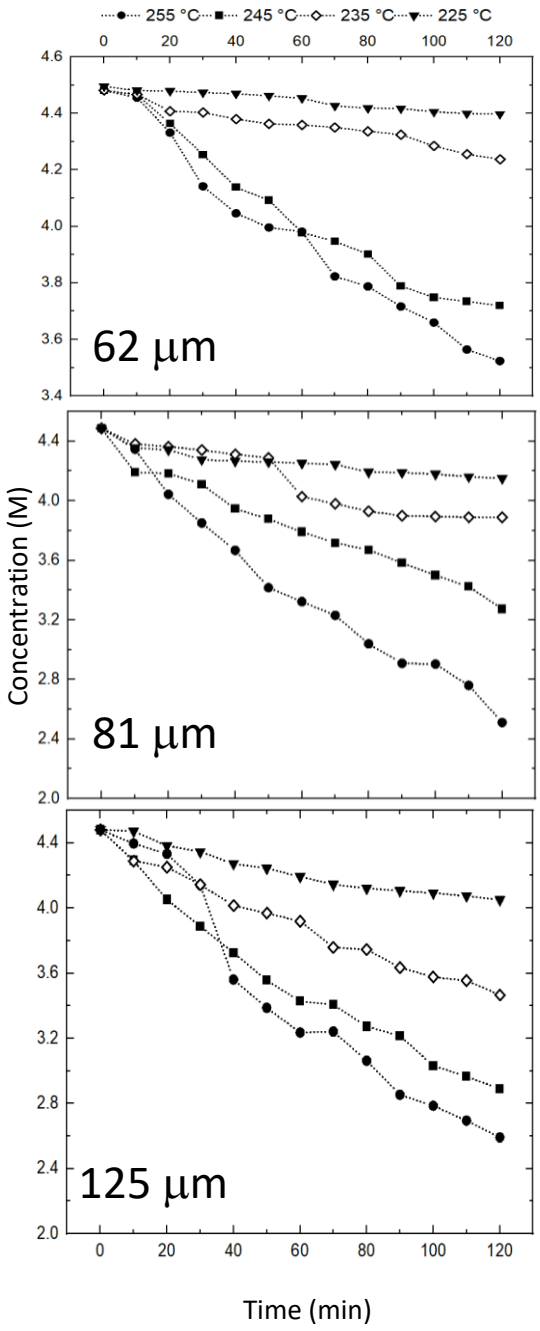

Figure 4.36. Change in concentration of H12-BT over time for 5 wt.% Pt/γ-Al_2O_3 with three different coating thicknesses (62 μm, 81 μm, 125 μm) on SS pellets in an inductive batch reactor. Process conditions: 50 mL batch reactor, = reaction time 120 min, VH12-BT = 10 mL, T=260°C.

The results showed the concentration of H12-BT decreasing over time, with higher temperatures accelerating the reaction, as shown in Figure 4.36. As the temperature increases, the concentration gradient becomes steeper, showing a more significant reduction in H12-BT. This figure also compares the change in H12-BT concentration for three different catalyst coating thicknesses (62 μm, 81 μm,

125 µm) across temperatures ranging from 225 °C to 255 °C. The 81 µm coating demonstrated the best overall efficiency, achieving the most significant reduction in H12-BT concentration. This indicated an optimal balance between catalytic surface area and mass transfer efficiency. In contrast, the 62 µm coating, while initially with fast reaction rates, showed lower overall efficiency due to limited catalytic material. The 125 µm coating, on the other hand, resulted in the slowest reaction rates, likely due to diffusion limitations caused by the thicker layer.

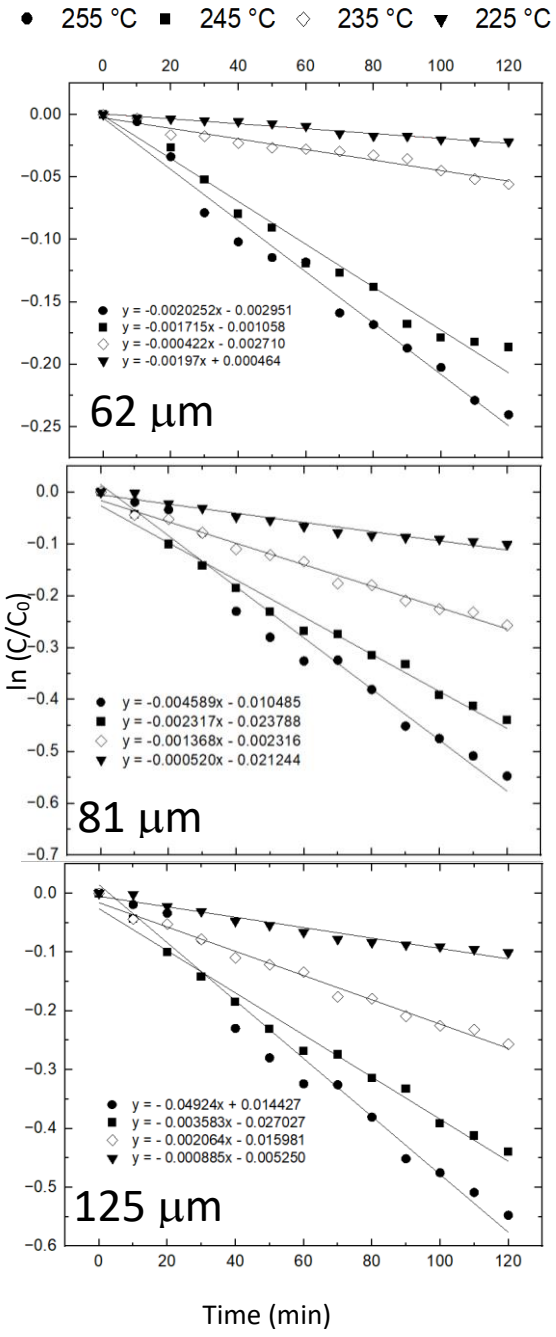

Figure 4.37. Representation of first-order kinetic model for the dehydrogenation of H12-BT using 5 wt.% Al_2O_3 with three different coating thicknesses (62 µm, 81 µm, 125 µm) on SS pellets

in an inductive batch reactor. Process conditions: 50 mL batch reactor, reaction time = 120 min, VH12-BT = 10 mL, T=260°C.

Figure 4.37 demonstrates the first-order kinetics of H12-BT dehydrogenation using 5 wt.% Al_2O_3 coated SS pellets (62 µm, 81 µm, 125 µm). The linear $\ln(C/C_o)$ vs. time plots confirm first-order behaviour, with reaction rates increasing at higher temperatures (255 °C and 245 °C) and decreasing with thicker coatings. The 62 µm coating gave the fastest rates due to superior heat and mass transfer, while the 125 µm coating gave slower rates, likely due to greater thermal and diffusion resistance. Intermediate behaviour was observed for the 81 µm coating. Rate constants derived from $\ln(C/C_o)$ vs. time plots demonstrated a clear dependence on both temperature and coating thickness, with thinner coatings outperforming due to reduced thermal resistance.

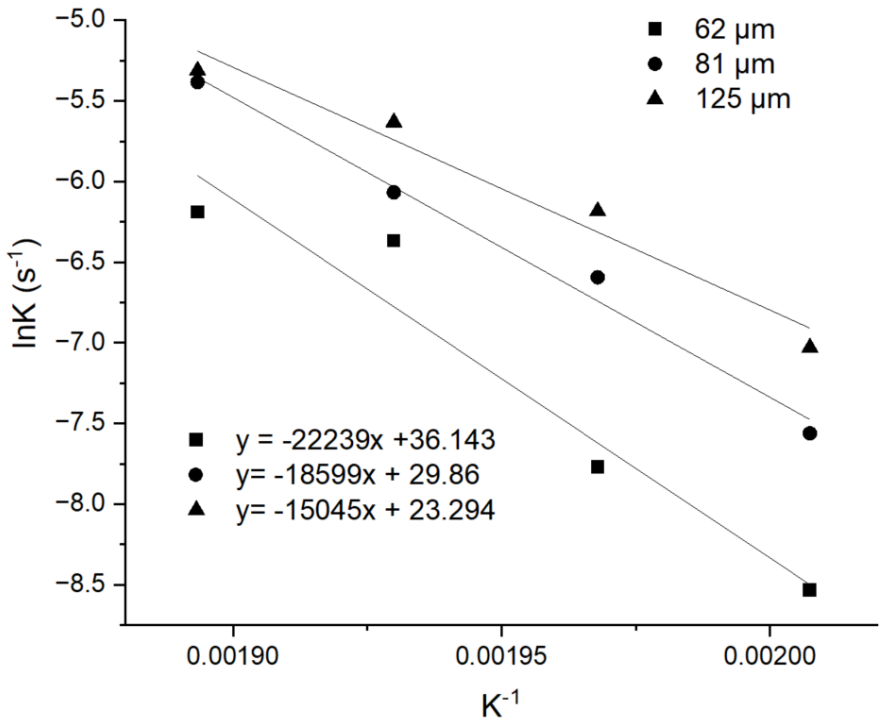

Figure 4.38. Arrhenius plots for the calculation of apparent activation energy for 5 wt.% Pt/γ-Al_2O_3, with three different coating thicknesses (62 µm, 81 µm, 125 µm) on SS pellets, in an inductive batch reactor. Process conditions: 50 mL batch reactor, reaction time = 120 min, VH12-BT = 10 mL, T=260°C.

Figure 4.38 shows the Arrhenius plots for calculating the E_a of H12-BT dehydrogenation using 5 wt.% Pt/γ-Al_2O_3 coated SS pellets (62 µm, 81 µm and , 125 µm). The linear relationships between lnk and $1/T(K^{-1})$ confirmed the Arrhenius behaviour of the reaction, with slopes indicating activation energies.

The thinnest coatings (62 µm) gave the highest E_a at 184.895 kJ/mol.K, while the thickest coating (125 µm) gave the lowest E_a at 125.08 Kj/mol.K, reflecting reduced thermal resistance and improved

catalytic efficiency in thinner coatings. Intermediate E_a was observed for the 81 µm coating (154.632 Kj/mol.K).

The rate constants, initial reaction rates, TOFs and E_a for these coating thicknesses and reaction conditions are summarised in Table 4.10. The slopes were obtained from a minimum of twelve points, and a fit accuracy of 96%, which indicates excellent model fitting, emphasising the reliability of the derived activation energies. The data highlights that thinner coatings facilitate faster reactions at elevated temperatures due to enhanced heat transfer and surface availability, while thicker coatings mitigate this effect, potentially due to diffusion barriers.

Table 4.9. Comparison of rate constants (k), initial reaction rates, TOFs and activation energies for 5 wt.% Pt/Al_2O_3, with three different coating thicknesses, between 225 °C and 255 °C.

Catalyst coating (µm)	Temperature (°C)	k (min^{-1})	r (min^{-1}/gcat)	TOF (min^{-1})	E_a (KJ/mol.K)
61	225	0.000197	0.020	1.55	184.895
	235	0.000422	0.042	3.37	
	245	0.001715	0.170	12.17	
	255	0.002052	0.204	16.01	
82	225	0.000520	0.052	3.24	154.632
	235	0.001368	0.136	8.44	
	245	0.002317	0.231	14.20	
	255	0.004589	0.457	28.12	
125	225	0.000885	0.088	3.46	125.084
	235	0.002064	0.205	8.08	
	245	0.003579	0.356	13.97	
	255	0.004924	0.490	19.23	

According to Table 4.10, the rate constant, initial reaction rate and TOF increase at each of the temperatures considered here as the thickness of the catalyst coating increases from 61 µm to 125

µm. However, as the coating thickness increases so the E_a decreases: 184.895 kJ/mol.K for 61 µm, 154.632 kJ/mol.K for 82 µm and 125.084 kJ/mol.K for 125 µm. This pattern clearly suggests the existence of mass transfer constraints as the thinner catalyst coatings (61 µm) show behaviour dominated by reaction kinetics, which increases the activation energy. The apparent E_a is essentially decreased as the coating thickness increases due to increased internal diffusion resistance within the catalyst layer. This implies that at higher thicknesses the reactant diffusion to active catalytic sites becomes more constrained, transferring control from reaction kinetics to mass transfer constraints. The trade-off between higher initial reaction rates and the increasing impact of mass transfer constraints at higher coating thicknesses is explained by the increasing TOF with coating thickness, which occurs because transport resistance limits the accessibility of active sites.

This is supported by results reported by others. Peters *et al.* reported that thinner catalyst layers (24 µm) have negligible mass transfer effects and exhibit kinetic behaviour dominated by intrinsic catalyst activity (Peters *et al.*, 2015). A shift toward diffusion-controlled regimes is indicated by a decrease in E_a with increasing layer thickness. Overall, productivity decreases as a result, with the thinnest layer reaching a maximum hydrogen productivity of 10.9 gH_2/g_{Pt}/min. Diffusion resistance prevents reactants from reaching active sites, therefore thinner layers exhibit lower efficiencies. The increase in apparent TOF as the layer thickness decreases illustrates how reactant diffusion is constrained by mass transfer constraints, thus reducing the efficient use of active catalytic sites. The findings validate a crucial compromise between catalytic performance diffusion resistance and layer thickness (Peters *et al.*, 2015).

4.9 LOHC Analysis

Following dehydrogenation, the reaction mixture was qualitatively analysed to determine the LOHC composition and evaluate the development of intermediates and by-products. The use of GC-MS to identify and characterise the chemical composition of the reaction mixture addresses here, rather than conversion alone. GC-MS was used to determine selectivity trends and qualitatively evaluate the presence of by-products and dehydrogenation intermediates. Table 4.11 summarises the GC-MC retention times recorded for the key intermediates and isomers of H12-BT. Several retention times correspond to various partially dehydrogenated species.

Table 4.10. Retention times recorded during the dehydrogenation of H12-BT using GC-MC.

Isomers	Retention time (min)
H12-BT	29.7–32.6
H6-BT	32.3–35
HBT	35.3–39.2

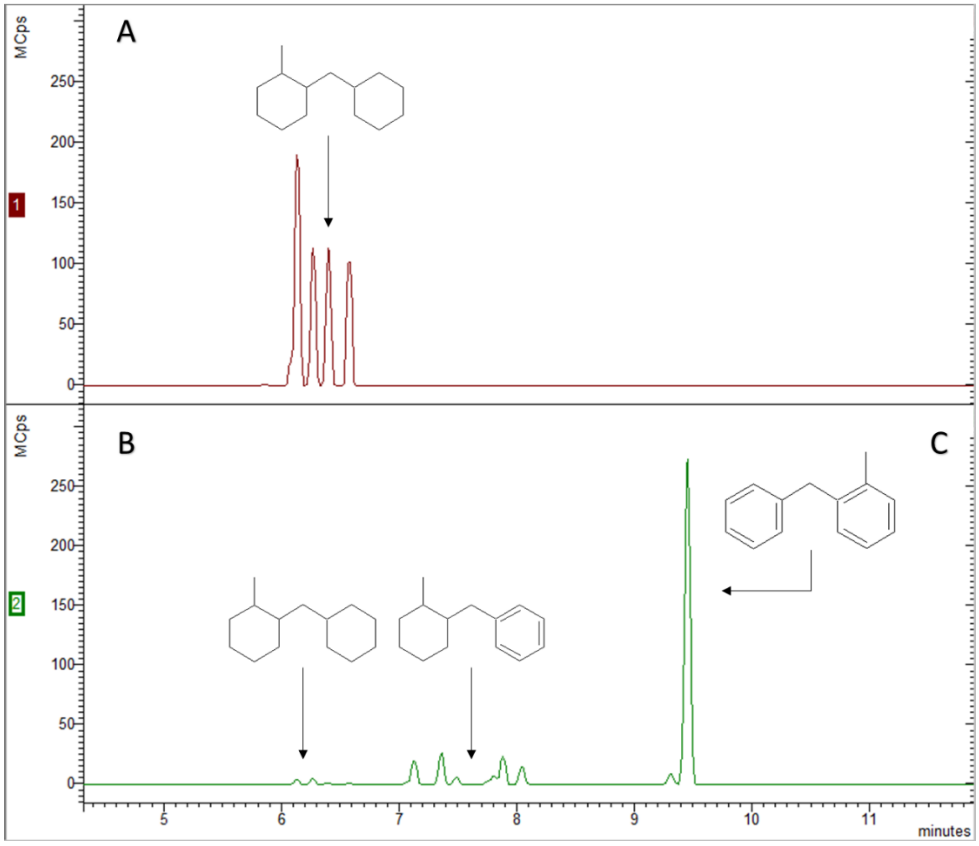

Figure 4.39. Example of GC-MC chromatogram depicting H12-BT (A), H6-BT and HBT (C), showing the retention times as tabulated in Table 4.11.

Figure 4.39 shows the peaks obtained from the GC-MS corresponding to H12-BT, the intermediate H6-BT and the dehydrogenated HBT. The peaks were integrated, and the DOD was calculated using equation 2.2.

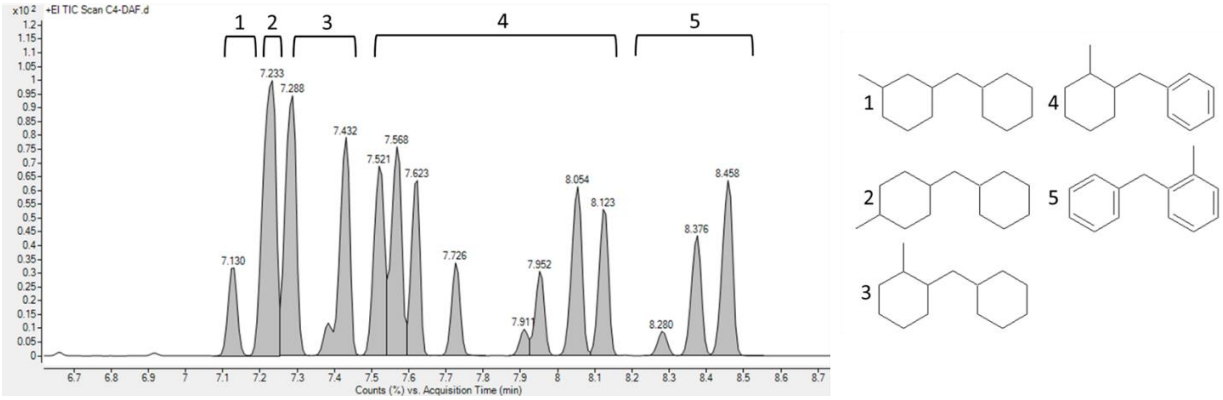

Figure 4.40. GC-MS chromatogram obtained after dehydrogenation of H12-BT showing H6-BT and HBT. (NIST 17 mass spectral library used to identify the compounds.)

4.10 Key Findings

Feasibility of inductive heating for the catalytic dehydrogenation of LOHCs inductive BTwas thoroughly assessed. The use of inductive heating with Pt/γ-Al_2O_3 catalysts was efficient in improving hydrogen evolution. Compared to conventional heating, inductive heating exhibited a more consistent and controlled thermal profile, which could reduce thermal stress and enhance catalyst performance over the long run. Pt/γ-Al_2O_3 $_3$ catalysts with various loadings: 0.3–8 wt.%. were tested. That with the 5 wt.% loading exhibiting the best overall performance, where the best balance was struck between stability, hydrogen productivity and catalytic activity. Higher loadings (8 wt.%) caused limitations in diffusion and particle accumulation.

Of the binders that were tested, the PVP 55000 at 0.5 wt.% balanced adhesion and diffusion, affording the highest catalytic efficiency here, whereas higher molecular weight binders resulted in decreased productivity and diffusion limitations. Regarding coating thickness, the result have shown that intermediate layers (81 μm) perform best, optimising hydrogen evolution while avoiding diffusion resistance seen in thicker coatings (100 μm). It was further investigated here how coating thickness affected reaction kinetics. It was determined that thicker coatings create transport restrictions while thinner coatings promote faster reaction rates through improved heat and mass transfer.

The dehydrogenation reaction followed first-order kinetics, with activation energy decreasing with increasing coating thickness according to kinetic analysis. Arrhenius plots showed that thicker coatings shifted toward diffusion-limited behaviour while thinner coatings showed higher activation energies because of a reaction-controlled mechanism. Higher catalyst loading caused the TOFs to increase with greater coating thickness, however, excessive thickness impeded mass transport. A comparison of inductive and conventional electrical heating revealed that the former afforded a more controlled

thermal profile, which improves catalyst longevity and process stability, while the latter produced a slightly higher DOD.

Using the analytical techniques BET, SEM-EDS, TEM, XRD, ICP-OES and CO pulse chemisorption, detailed characterisation was carried out to examine surface area, porosity, metal dispersion, particle size, and crystallinity. The accuracy of the catalyst preparation procedure was demonstrated by ICP-OES, verifying that actual Pt loadings closely matched target values. According to the results of CO pulse chemisorption, metal dispersion decreased as the Pt content increased, resulting in a smaller active surface area and larger particles. According to BET analysis, due to partial pore blockage and metal particle agglomeration an increasing Pt loading decreases surface area, thus limiting nitrogen access to internal surface sites. The BET and pore volume data showed that this effect intensifies at higher loadings. Higher Pt concentrations resulted in more clustering. SEM-EDS verified uniform Pt coating at lower loadings. TEM analysis showed that catalyst activity is affected by an increase in NP size due to increase in Pt loading. The presence of Pt crystallites and the structural integrity of the Pt/γ-Al_2O_3 support were confirmed by XRD patterns, which showed sharper Pt peaks at higher loadings.

Cycling tests demonstrated a decrease in hydrogen evolution and reaction efficiency along with progressive catalyst deactivation over several runs. Performance declined, as evidenced by the DOD, which decreased from 27% in cycle 1 to 3% by cycle 4. Furthermore, productivity decreased over the cycles, indicating possible deactivation mechanisms (poisoning or catalyst sintering). This is supported by the description of catalyst deactivation brought on by sintering and poisoning, in a hot pressure swing reactor (Jorschick *et al.*) It was shown that, over several cycles, surface contamination and progressive agglomeration significantly decreased the number of available active sites and the overall reaction efficiency. The dehydrogenation pathway and the intermediates were validated by GC-MS analysis of the liquid phase, revealing a gradual conversion of H12-BT to HBT, via H6-BT, with little production of by-products (m-fluorene).

Energy efficiency was established by comparing the same reaction under both heating techniques (electrical heating and inductive heating), with the same catalyst loading (0.089 mol% Pt:H12-BT). Although electrical heating resulted in greater hydrogen flow, inductive heating resulted in a more stable, controlled hydrogen release, with lower peak temperatures and a more consistent temperature gradient (Figure 4.15), thus lowering thermal stress and possible energy loss. In summary, this study showed that inductive heating can indeed be successfully used to dehydrogenate H12-BT and, furthermore, it provides a more energy-efficient option than traditional electrical heating.

5. Chapter 5: Conclusions and Recommendations

5.1 Conclusions

The main aim of this study was to determine whether inductive heating could address the shortcomings of conventional heating systems, particularly the high energy usage and uneven temperature distribution that limit the effectiveness of H12-BT dehydrogenation.

The present study addressed the determination of the feasibility of inductive heating for the catalytic dehydrogenation of H12-BT. To this end, the following specific topics, as headlined in Sections 5.1.1.–5.1.6, were investigated/addressed. Conclusions to each are presented below (5.1.1–5.1.6).

Overall, this study has demonstrated that inductive heating is indeed a viable approach for LOHC dehydrogenation—resolving limitations of conventional heating methods by improving energy efficiency, catalyst composition, and mass transfer dynamics. Inductive heating provides a scalable and effective method for hydrogen release, thus advancing the potential of LOHC technology in sustainable energy systems.

5.1.1 Synthesising Pt/γ-Al_2O_3 catalysts with different metal loadings (0.3, 1, 3 and 8 Pt wt.%), using the wet impregnation method

Utilising several advanced characterisation techniques, it was established that f Pt/γ-Al_2O_3 catalysts were successfully synthesised through the wet impregnation method; metal loadings ranging from 0.3 wt.% to 8 wt.% were obtained. ICP-OES confirmed the Pt loadings where the actual loadings closely matched the target loadings. (For example, the target loading of 5 wt.% Pt had an actual loading of 5.36 wt.%.) Changes in surface area and pore volume were shown by BET analysis, confirming that Pt was deposited onto the γ-Al_2O_3 support. With increasing clusters at higher Pt concentrations, TEM imaging showed well-dispersed Pt NPs at lower loadings. XRD analysis confirmed Pt crystallinity and showed that loading increased the intensity of distinct Pt (111) peaks. According to CO pulse chemisorption, as the Pt wt.% increases from 0.3% to 8%, the dispersion and surface area decrease, while particle size increases. At 0.3 wt.%, the highest dispersion (65.64%) and largest surface area (162.1 m^2/g) are observed, while particle size increases from 1.73 nm to 3.21 nm—highlighting the impact of elevated Pt loading on NP aggregation.

5.1.2 Preparing inductively active catalyst materials of varying shell thickness of Pt/γ-Al_2O_3 on SS pellets, using a dip coating method, and determining the effect of the added polymer binders

The study examined the effects of four polymer binders on catalyst adhesion, active site exposure and diffusion properties: PVP 55000, PVP 360000, PVA 22000 and PVA 89000–98000. PVP 55000 (=X wt.%) showed the highest catalytic efficiency, allowing for improved catalyst dispersion and reactant accessibility. Further binder concentrations (0.25–1 wt.%) were tested. Here, 0.5 wt.% showed the best catalytic adhesion with the highest cumulative flow (1.63 L) and hydrogen productivity (0.25 $gH_2/gPt^{-1}/min^{-1}$). Reduced concentrations (0.25 wt.%) led to insufficient catalyst adhesion whereas greater concentrations (0.75 wt.%) decreased hydrogen productivity by 16%, by causing metal agglomeration and diffusion constraints.

5.1.3 Conducting the dehydrogenation of H12-BT using a batch reactor system, then evaluating the catalyst performance in terms of productivity, selectivity, and conversion

The catalytic performance was methodically assessed in a batch reactor under controlled conditions—conversion, selectivity and hydrogen productivity were key performance indicators. The best performing catalyst was 5 wt.% Pt/γ-Al_2O_3 with an optimal conversion (65%), selectivity (18%) and hydrogen productivity (0.35 $gH_2/gPt/min$). Lower Pt loadings (0.35 wt.%) showed poor dehydrogenation efficiency while higher metal loadings (8 wt.%) showed a decrease in the number of available active sites through metal accumulation. A 60% decrease in hydrogen productivity over four cycles was found in multi-cycle stability tests, mostly due to catalyst deactivation and by-product formation.

5.1.4 Investigating the effect of catalyst shell thickness on mass transfer limitations during the dehydrogenation of H12-BT

The effectiveness of mass transfer and catalytic activity were found to be significantly influenced by the coating thickness. Upon varying the coating thickness from 62 μm to 12 5μm, it was found that the 81 μm coating preformed the best, achieving a hydrogen productivity of 0.29 $gH_2/gPt/min$. Due to improved heat and mass transfer, thinner coatings (62 μm) enabled higher reaction rates; however, thicker coatings (125 μm) reduced hydrogen productivity by 12%. Following first-order reaction kinetics, kinetic analysis verified that dehydrogenation changed from a reaction-controlled to a diffusion-limited process at higher coating thicknesses, with activation energy decreasing from 184.9

kJ/mol for 62 μm to 125.1 kJ/mol for 125 μm.

A comparison between 3 wt.% and 5 wt.% catalysts at varying coating thicknesses (62–125 μm) revealed that all coating thicknesses exhibited similar trends, where thinner coatings producing more hydrogen. The 81 μm coating thickness gave the highest productivity, whereas the thickest coating gave decreased hydrogen productivity, 12%. The H12-BT molar fractions decreased from 57% to 49% for the 3 wt.%, indicating high conversion at intermediate coating thicknesses. At 5 wt.%,the H12-BT molar fractions decreased from 63% to 22%. Thicker coatings, 100 μm and 125 μm, impaired reactant diffusion and resulted in decreased performance. SEM analysis showed that as catalyst loading and thickness increase, surface roughness increases. During four cycles, multi-cycle stability tests showed a 60% decrease in hydrogen productivity, mostly because of catalyst deactivation and by-product formation.

5.1.5 Catalytic activity assessment for the release of hydrogen from LOHCs, utilising various characterisation techniques: ICP, TPR, CO pulse chemisorption, H2-TPR, SEM-EDS, BET, TEM, HR-TEM, XRD and TGA

Thorough characterisation validated the catalyst synthesis and dehydrogenation performance of Pt/γ-Al_2O_3. SEM-EDS showed a shift from well-dispersed NPs at lower loadings (0.3 wt.%) to catalyst accumulation clusters at higher loadings (8 wt.%). BET analysis demonstrated a decrease in surface area with increasing Pt loading. A surface area decreased from 186.8 m^2/g at 0.3 w.% to 169.3 m^2/g at 8 wt.%, illustrating how Pt aggregation affects active surface area. TEM imaging showed an increase in NP size with increasing Pt loading, from 1.11 nm for 0.3 wt.% to 4.53 nm for 8 wt.% before dehydrogenation, and later to 2.69 nm and 6.91 nm, respectively, after 80 min reaction. HR-TEM analysis. Confirming sintering effects and the migration of NPs at elevated Pt concentrations. Larger Pt crystallite formation was indicated by sharper Pt peaks and a corresponding increase in Pt crystallinity at higher loadings according to XRD analysis. CO pulse chemisorption showed that as the Pt content increased, the metal dispersion decreased from 65.64% to 35.34% for the 0.3 wt.% and 8 wt.%, respectively.

HR-TEM analysis revealed that, following dehydrogenation, the d-spacing decreased from 0.23 nm to 0.20 nm, indicating lattice contraction brought on by sintering. The initial weight loss for polymers is seen at 200 °C in TGA data (due to moisture loss), followed by a higher loss at 300-450 °C, showing the primary decomposition step. PVP MW 55000 exhibited the greatest loss. Polymers with a higher molecular weight degraded more slowly, showing better thermal stability. Tests of multi-cycle

dehydrogenation showed progressive catalyst deactivation from the first to the fourth cycle: hydrogen productivity decreased by 60% and the DOD decreased from 27% to 3%. With few adverse reactions, the stepwise dehydrogenation pathway from H12-BT to HBT via H6-BT was confirmed by GC-MS analysis.

5.1.6 Comparing inductive and electrical heating for LOHC dehydrogenation

Inductive heating produced more consistent and focused heat delivery, thus reducing thermal stress, and enhancing catalyst stability, while electrical heating produced a marginally higher dehydrogenation efficiency. Inductive heating showed a lower cumulative hydrogen flow (1.65 L) compared to electrical heating (2.03 L). While electrical heating performed marginally better, with 0.38 gH_2/gPt/min, inductive heating reached a maximum hydrogen productivity of 0.35 gH_2/gPt/min. By enabling controlled temperature gradients and quicker heat transfer, inductive heating assists in minimising energy losses that are often linked to conventional heating techniques.

Superior thermal control was exhibited by inductive heating, which allowed for uniform and localised heat distribution, thus reducing thermal stress and extending the catalyst life. However electrical heating was linked to higher energy losses and irregular thermal gradients that aided in catalyst degradation over extended periods of operation, despite producing a slightly higher dehydrogenation efficiency (33.83%) compared to inductive heating (33.10%); however, electrical heating is associated with greater energy losses and non-uniform heat distribution. Inductive heating gives enhanced process efficiency and decreases overall energy consumption by enabling precise and quick heat transfer. A scalable environmentally friendly method of releasing hydrogen is therefore inductive heating, which reduces the inherent inefficiencies of traditional heating.

5.2 Recommendations for future work

The potential application of LOHC technology in, particularly, transportation has been identified, for large-scale hydrogen storage and distribution. However, the high energy demand and uneven temperature distribution within the endothermic dehydrogenation processes is the major drawback of the LOHC system, which remains an attractive technique that is fully compatible with existing infrastructure. Electromagnetic inductive heating addresses limitations associated with conventional heating methods for endothermic dehydrogenation reactions of LOHCs—it may offer faster heating rates, while directing the heat from the core of the inductively active materials to the catalyst and the surrounding fluid. In order to improve the effectiveness and scalability of LOHC dehydrogenation via inductive heating, further studies are required. Future recommendations include the following.

- Optimisation of the acidity of the support medium Al_2O_3, towards optimising the catalytic performance. Comparison can be made between Lewis and Bronsted acid sites on support medium Al_2O_3. The acidity of the support affects unwanted side reactions like cracking or coke formation in addition to influencing Pt dispersion. More advanced catalyst preparation methods, including doping and thermal controlled methods, should be considered in efforts to investigate the effect of the acidity of the support material on adsorption and desorption behaviour.

i. The synthesis of ferromagnetic iron and iron oxide NPs for the use in inductive heating, to investigate dehydrogenation of LOHCs in addition to the density functional theory method (DFT). Studies have shown that iron NP catalysts achieve 100% conversion and selectivity in the dehydrogenation of 1,2,3,4-tetrahydroquinoline (Yang *et al.*, 2021). Ferromagnetic iron and iron oxide NPs' ferromagnetic properties provide efficient heat generation through inductive heating and, together with the high surface area and nanoscale reactivity of iron and the NPs, could exhibit exceptional catalytic activity.

ii. Switching from a batch type to a continuous-flow reactor configurations may be a crucial first step in increasing process scalability and efficiency. A continuous-flow reactor configuration should be tested in an effort to improve process efficiency and thermal control. Furthermore, precise thermal control, quicker start-up times and increased system efficiency could all be achieved by combining inductive heating with a continuous-flow batch reactor.

Future developments in inductive heating-based LOHC dehydrogenation can open the door to more effective scalable and economically feasible hydrogen storage options by tackling these important research areas. Such efforts will support the wider adoption of LOHC technology in sustainable energy systems by facilitating energy advancements and reducing heat loss, especially in industrial applications.

6. References

Aakko-Saksa, P.T., Cook, C., Kiviaho, J. & Repo, T. 2018. Liquid organic hydrogen carriers for transportation and storing of renewable energy–Review and discussion. *Journal of Power Sources*, 396:803-823.

Abdalla, A.M., Hossain, S., Nisfindy, O.B., Azad, A.T., Dawood, M. & Azad, A.K. 2018. Hydrogen production, storage, transportation and key challenges with applications: A review. *Energy Conversion and Management*, 165:602-627.

Abu-Laban, M., Muley, P.D., Hayes, D.J. & Boldor, D. 2017. Ex-situ up-conversion of biomass pyrolysis bio-oil vapors using Pt/Al2O3 nanostructured catalyst synergistically heated with steel balls via induction. *Catalysis Today*, 291:3-12.

Adametz, P., Müller, K. & Arlt, W. 2016. Energetic evaluation of hydrogen storage in metal hydrides. *International Journal of Energy Research*, 40(13):1820-1831.

Al-ShaikhAli, A.H., Jedidi, A., Cavallo, L. & Takanabe, K. 2015. Non-precious bimetallic catalysts for selective dehydrogenation of an organic chemical hydride system. *Chemical Communications*, 51(65):12931-12934.

Alconada, K. & Barrio, V.L. 2024. Enhancing Perhydrobenzyltoluene Dehydrogenation Performance with Co, Mo and Mn Metal Oxides: A Comparative Study with Pt/Al2o3 Catalyst. *Mo and Mn Metal Oxides: A Comparative Study with Pt/Al2o3 Catalyst*, 41(47):22097-22103.

Alconada, K. & Barrio, V.L. 2024. Enhancing perhydrobenzyltoluene dehydrogenation performance with Co, Mo and Mn metal oxides: a comparative study with Pt/Al2o3 catalyst. *Applied Catalysis B: Environment and Energy*, 357:124349.

Alexeev, O.S., Chin, S.Y., Engelhard, M.H., Ortiz-Soto, L. & Amiridis, M.D. 2005. Effects of reduction temperature and metal− support interactions on the catalytic activity of Pt/γ-Al2O3 and Pt/TiO2 for the oxidation of CO in the presence and absence of H2. *The Journal of Physical Chemistry B*, 109(49):23430-23443.

Ali, A., Rohini, A.K., Noh, Y.S., Moon, D.J. & Lee, H.J. 2022. Hydrogenation of dibenzyltoluene and the catalytic performance of Pt/Al2O3 with various Pt loadings for hydrogen production from perhydro-dibenzyltoluene. *International Journal of Energy Research*, 46(5):6672-6688.

Andersson, J. & Grönkvist, S. 2019. Large-scale storage of hydrogen. *International Journal of Hydrogen Energy*, 44(23):11901-11919.

Ara, K. 1989. Magnetic characteristics of ferromagnetic stainless steels. *IEEE Transactions on Magnetics*, 25(3):2617-2623.

Araújo, J.C., Oton, L.F., Oliveira, A.C., Lang, R., Otubo, L. & Bueno, J.M. 2019. On the role of size controlled Pt particles in nanostructured Pt-containing Al2O3 catalysts for partial oxidation of methane. *International Journal of Hydrogen Energy*, 44(50):27329-27342.

Asiaban, S., Kayedpour, N., Samani, A.E., Bozalakov, D., De Kooning, J.D., Crevecoeur, G. & Vandevelde, L. 2021. Wind and solar intermittency and the associated integration challenges: A comprehensive review including the status in the Belgian power system. *Energies*, 14(9):2630.

Auer, F., Hupfer, A., Bösmann, A., Szesni, N. & Wasserscheid, P. 2020. Influence of the nanoparticle size on hydrogen release and side product formation in liquid organic hydrogen carrier systems with supported platinum catalysts. *Catalysis Science & Technology*, 10(19):6669-6678.

Barthélémy, H., Weber, M. & Barbier, F. 2017. Hydrogen storage: Recent improvements and industrial

perspectives. *International Journal of Hydrogen Energy*, 42(11):7254-7262.

Bhogeswararao, S. & Srinivas, D. 2015. Catalytic conversion of furfural to industrial chemicals over supported Pt and Pd catalysts. *Journal of Catalysis*, 327:65-77.

Bollmann, J., Schmidt, N., Beck, D., Preuster, P., Zigan, L., Wasserscheid, P. & Will, S. 2023. A path to a dynamic hydrogen storage system using a liquid organic hydrogen carrier (LOHC): burner-based direct heating of the dehydrogenation unit. *International Journal of Hydrogen Energy*, 48(3):1011-1023.

Bollmann, J., Mitländer, K., Beck, D., Schühle, P., Bauer, F., Zigan, L., ... Will, S. 2023. Burner-heated dehydrogenation of a liquid organic hydrogen carrier (LOHC) system. *International Journal of Hydrogen Energy*, 48(77):30039-30056.

Borges, C.L.T. 2012. An overview of reliability models and methods for distribution systems with renewable energy distributed generation. *Renewable and Sustainable Energy Reviews*, 16(6):4008-4015.

Brigljević, B., Byun, M. & Lim, H. 2020. Design, economic evaluation, and market uncertainty analysis of LOHC-based, CO2 free, hydrogen delivery systems. *Applied Energy*, 274:115314.

Brückner, N., Obesser, K., Bösmann, A., Teichmann, D., Arlt, W., Dungs, J. & Wasserscheid, P. 2014. Evaluation of Industrially applied heat-transfer fluids as liquid organic hydrogen carrier systems. *ChemSusChem*, 7(1):229-235.

Centeno, T. & Stoeckli, F. 2010. The assessment of surface areas in porous carbons by two model-independent techniques, the DR equation and DFT. *Carbon*, 48(9):2478-2486.

Cho, J.-Y., Kim, H., Oh, J.-E. & Park, B.Y. 2021. Recent Advances in homogeneous/heterogeneous catalytic hydrogenation and dehydrogenation for potential liquid organic hydrogen carrier (LOHC) Systems. *Catalysts*, 11(12):1497.

Choi, Y., Wu, X., Lee, J. & Na, K. 2024. Catalytic dehydrogenation for hydrogen production controlled by metal-supported heterogeneous catalysts. *Catalysis Science & Technology.*

Chu, C., Wu, K., Luo, B., Cao, Q. & Zhang, H. 2023. Hydrogen storage by liquid organic hydrogen carriers: Catalyst, renewable carrier, and technology-A review. *Carbon Resources Conversion*, 6(4):334-351.

Dabbagh, H.A., Rasti, E., Yalfani, M.S. & Medina, F. 2011. Formation of γ-alumina nanorods in presence of alanine. *Materials Research Bulletin*, 46(2):271-277.

Dao, Q.N., On, E., Ramadhani, S., Lee, K., Sohn, H., Choi, S.H., ... Kim, Y. 2024. Catalytic insights into perhydro-benzyltoluene dehydrogenation: Probing surface characteristics revealed by DRIFTS study. *International Journal of Hydrogen Energy*, 56:1284-1293.

Dauletbay, A. 2024. Transportation of Hydrogen: Hydrogen Usage. In. *Hydrogen Technologies-Advances, Insights, and Applications*: IntechOpen, 6(4):334-351.

Dennis, J., Bexten, T., Petersen, N., Wirsum, M. & Preuster, P. 2021. Model-based analysis of a liquid organic hydrogen carrier (LOHC) system for the operation of a hydrogen-fired gas turbine. *Journal of Engineering for Gas Turbines and Power*, 143(3):031011.

Dornheim, M., Baetcke, L., Akiba, E., Ares, J.-R., Autrey, T., Barale, J., ... Charbonnier, V. 2022. Research and development of hydrogen carrier based solutions for hydrogen compression and storage. *Progress in Energy*, 4(4):042005.

Durbin, D. & Malardier-Jugroot, C. 2013. Review of hydrogen storage techniques for on board vehicle applications. *International Journal of Hydrogen Energy*, 38(34):14595-14617.

Dürr, S., Zilm, S., Geißelbrecht, M., Müller, K., Preuster, P., Bösmann, A. & Wasserscheid, P. 2021.

Experimental determination of the hydrogenation/dehydrogenation-Equilibrium of the LOHC system H0/H18-dibenzyltoluene. *International Journal of Hydrogen Energy*, 46(64):32583-32594.

Ertl, G., Knözinger, H. & Weitkamp, J. 1997. *Handbook of Heterogeneous Catalysis*.

Faber, J. & Fawcett, T. 2002. The powder diffraction file: present and future. *Structural Science*, 58(3):325-332.

Falamaki, C., Naimi, M. & Aghaie, A. 2006. Dip-coating technique for the manufacture of alumina microfilters using PVA and Na-CMC as binders: a comparative study. *Journal of the European Ceramic Society*, 26(6):949-956.

Fikrt, A., Brehmer, R., Milella, V.-O., Müller, K., Bösmann, A., Preuster, P., ... Arlt, W. 2017. Dynamic power supply by hydrogen bound to a liquid organic hydrogen carrier. *Applied Energy*, 194:1-8.

Ford, D., Kruger, G., Garidzirai, R., Modisha, P., Krieg, H. & Bessarabov, D. 2024. Feasibility of induction heating for the dehydrogenation of liquid organic hydrogen carriers. *International Journal of Hydrogen Energy*, 77:520-525.

Franco, A. & Rocca, M. 2024. Renewable electricity and green hydrogen integration for decarbonization of “hard-to-abate” industrial sectors. *Electricity*, 5(3):471-490.

Garidzirai, R., Modisha, P., Shuro, I., Visagie, J., van Helden, P. & Bessarabov, D. 2021. The effect of Mg and Zn dopants on Pt/Al2O3 for the dehydrogenation of perhydrodibenzyltoluene. *Catalysts*, 11(4):490.

Geburtig, D., Preuster, P., Bösmann, A., Müller, K. & Wasserscheid, P. 2016. Chemical utilization of hydrogen from fluctuating energy sources–Catalytic transfer hydrogenation from charged Liquid Organic Hydrogen Carrier systems. *International Journal of Hydrogen Energy*, 41(2):1010-1017.

Geiling, J., Steinberger, M., Ortner, F., Seyfried, R., Nuß, A., Uhrig, F., ... März, M. 2021. Combined dynamic operation of PEM fuel cell and continuous dehydrogenation of perhydro-dibenzyltoluene. *International Journal of Hydrogen Energy*, 46(72):35662-35677.

Geißelbrecht, M., Mrusek, S., Müller, K., Preuster, P., Bösmann, A. & Wasserscheid, P. 2020. Highly efficient, low-temperature hydrogen release from perhydro-benzyltoluene using reactive distillation. *Energy & Environmental Science*, 13(9):3119-3128.

Gergely, R. & Hochenauer, C. 2023. Heating strategies for efficient combined inductive and convective heating of profiles. *Energies*, 16(16):5895.

Gianotti, E., Taillades-Jacquin, M.l., Rozière, J. & Jones, D.J. 2018. High-purity hydrogen generation via dehydrogenation of organic carriers: a review on the catalytic process. *ACS Catalysis*, 8(5):4660-4680.

Granovskii, M., Dincer, I. & Rosen, M.A. 2007. Greenhouse gas emissions reduction by use of wind and solar energies for hydrogen and electricity production: economic factors. *International Journal of Hydrogen Energy*, 32(8):927-931.

Grillo, F., Van Bui, H., Moulijn, J.A., Kreutzer, M.T. & Van Ommen, J.R. 2017. Understanding and controlling the aggregative growth of platinum nanoparticles in atomic layer deposition: an avenue to size selection. *The Journal of Physical Chemistry Letters*, 8(5):975-983.

Harb, H., Elliott, S.N., Ward, L., Foster, I.T., Klippenstein, S.J., Curtiss, L.A. & Assary, R.S. 2023. Uncovering novel liquid organic hydrogen carriers: a systematic exploration of chemical compound space using cheminformatics and quantum chemical methods. *Digital Discovery*, 2(6):1813-1830.

Harris, P. 1986. The sintering of platinum particles in an alumina-supported catalyst: Further transmission electron microscopy studies. *Journal of Catalysis*, 97(2):527-542.

Hart, A., Adam, M., Robinson, J.P., Rigby, S.P. & Wood, J. 2020a. Inductive heating assisted-catalytic

dehydrogenation of tetralin as a hydrogen source for downhole catalytic upgrading of heavy oil. *Topics in Catalysis*, 63:268-280.

Hart, A., Adam, M., Robinson, J.P., Rigby, S.P. & Wood, J. 2020b. Tetralin and decalin H-donor effect on catalytic upgrading of heavy oil inductively heated with steel balls. *Catalysts*, 10(4):393.

Hart, A., Adam, M., Robinson, J.P., Rigby, S.P. & Wood, J. 2020c. Hydrogenation and dehydrogenation of tetralin and naphthalene to explore heavy oil upgrading using NiMo/Al2O3 and CoMo/Al2O3 catalysts heated with steel balls via induction. *Catalysts*, 10(5):497.

Hassan, Q., Sameen, A.Z., Salman, H.M., Jaszczur, M. & Al-Jiboory, A.K. 2023. Hydrogen energy future: Advancements in storage technologies and implications for sustainability. *Journal of Energy Storage*, 72:108404.

Hassan, Q., Algburi, S., Sameen, A.Z., Salman, H.M. & Jaszczur, M. 2024. Green hydrogen: A pathway to a sustainable energy future. *International Journal of Hydrogen Energy*, 50:310-333.

Haupt, A. & Müller, K. 2017. Integration of a LOHC storage into a heat-controlled CHP system. *Energy*, 118:1123-1130.

Huang, C., Wang, Y., Zhong, R., Sun, Z., Deng, Y. & Duan, L. 2023. Induction heating enables efficient heterogeneous catalytic reactions over superparamagnetic nanocatalysts. *Chinese Chemical Letters*, 34(9):108101.

Hwang, C.-P. & Yeh, C.-T. 1996. Platinum-oxide species formed by oxidation of platinum crystallites supported on alumina. *Journal of Molecular Catalysis A: Chemical*, 112(2):295-302.

Hwang, J., Maharjan, K. & Cho, H. 2023. A review of hydrogen utilization in power generation and transportation sectors: Achievements and future challenges. *International Journal of Hydrogen Energy*, 48(74):28629-28648.

Idakiev, V.V., Marx, S., Roßau, A., Bück, A., Tsotsas, E. & Mörl, L. 2015. Inductive heating of fluidized beds: Influence on fluidization behavior. *Powder Technology*, 286:90-97.

Jang, M., Shin, B.S., Jo, Y.S., Kang, J.W., Kwak, S.K., Yoon, C.W. & Jeong, H. 2020. A study on hydrogen uptake and release of a eutectic mixture of biphenyl and diphenyl ether. *Journal of Energy Chemistry*, 42:11-16.

Jeyaraj, M., Gurunathan, S., Qasim, M., Kang, M.-H. & Kim, J.-H. 2019. A comprehensive review on the synthesis, characterization, and biomedical application of platinum nanoparticles. *Nanomaterials*, 9(12):1719.

Jiang, Z., Gong, X., Wang, B., Wu, Z. & Fang, T. 2019. A experimental study on the dehydrogenation performance of dodecahydro-N-ethylcarbazole on M/TiO2 catalysts. *International Journal of Hydrogen Energy*, 44(5):2951-2959.

Jorschick, H., Geißelbrecht, M., Eßl, M., Preuster, P., Bösmann, A. & Wasserscheid, P. 2020. Benzyltoluene/dibenzyltoluene-based mixtures as suitable liquid organic hydrogen carrier systems for low temperature applications. *International Journal of Hydrogen Energy*, 45(29):14897-14906.

Jorschick, H., Preuster, P., Dürr, S., Seidel, A., Müller, K., Bösmann, A. & Wasserscheid, P. 2017. Hydrogen storage using a hot pressure swing reactor. *Energy & Environmental Science*, 10(7):1652-1659.

Karakaya, C. & Deutschmann, O. 2012. A simple method for CO chemisorption studies under continuous flow: Adsorption and desorption behavior of Pt/Al2O3 catalysts. *Applied Catalysis A: General*, 445:221-230.

Kerscher, M., Jander, J.H., Cui, J., Wasserscheid, P., Rausch, M.H., Koller, T.M. & Fröba, A.P. 2023.

Thermophysical properties of the liquid organic hydrogen carrier system based on diphenylmethane with the byproducts fluorene or perhydrofluorene. *International Journal of Hydrogen Energy*, 48(76):29651-29662.

Kim, J., Boo, K., Cho, J. & Moon, I. 2014. Key challenges in the development of an infrastructure for hydrogen production, delivery, storage and use. In. *Advances in Hydrogen Production, Storage and Distribution*: Elsevier. pp. 3-31.

Körner, A., Tam, C., Bennett, S. & Gagné, J. 2015. Technology roadmap-hydrogen and fuel cells. *International Energy Agency (IEA): Paris, France*:1-29.

Krieger, C., Müller, K. & Arlt, W. 2016a. Coupling of a liquid organic hydrogen carrier system with industrial heat. *Chemical Engineering & Technology*, 39(8):1570-1574.

Krieger, C., Müller, K. & Arlt, W. 2016b. Thermodynamic analysis of reversible hydrogenation for heat storage in concentrated solar power plants. *Solar Energy*, 123:40-50.

Kuhwald, C., Türkhan, S. & Kirschning, A. 2022. Inductive heating and flow chemistry–a perfect synergy of emerging enabling technologies. *Beilstein Journal of Organic Chemistry*, 18(1):688-706.

Langmi, H.W., Ren, J., North, B., Mathe, M. & Bessarabov, D. 2014. Hydrogen storage in metal-organic frameworks: a review. *Electrochimica Acta*, 128:368-392.

Lee, G., Jeong, Y., Kim, B.-G., Han, J.S., Jeong, H., Na, H.B. & Jung, J.C. 2015. Hydrogen production by catalytic decalin dehydrogenation over carbon-supported platinum catalyst: effect of catalyst preparation method. *Catalysis Communications*, 67:40-44.

Lee, J., Jang, E.J. & Kwak, J.H. 2019. Effect of number and properties of specific sites on alumina surfaces for Pt-Al2O3 catalysts. *Applied Catalysis A: General*, 569:8-19.

Lee, S., Lee, J., Kim, T., Han, G., Lee, J., Lee, K. & Bae, J. 2021. Pt/CeO2 catalyst synthesized by combustion method for dehydrogenation of perhydro-dibenzyltoluene as liquid organic hydrogen carrier: Effect of pore size and metal dispersion. *International Journal of Hydrogen Energy*, 46(7):5520-5529.

Leinweber, A. & Müller, K. 2018. Hydrogenation of the liquid organic hydrogen carrier compound monobenzyl toluene: Reaction pathway and kinetic effects. *Energy Technology*, 6(3):513-520.

Liang, X., Zhong, H.-J., Ding, H., Yu, B., Ma, X., Liu, X., ... He, J. 2024. Polyvinyl alcohol (PVA)-based hydrogels: Recent progress in fabrication, properties, and multifunctional applications. *Polymers*, 16(19):2755.

Lin, A. & Bagnato, G. 2024. Revolutionising energy storage: The Latest Breakthrough in liquid organic hydrogen carriers. *International Journal of Hydrogen Energy*, 63:315-329.

Maity, S., Kumar, S., Srivastava, M., Kharola, A., Maurya, K., Konathala, S., ... Garg, M. 2015. Characterization of asphaltenic material obtained by treating of vacuum residue with different reactive molecules. *Fuel*, 149:8-14.

Mäki-Arvela, P. & Murzin, D.Y. 2013. Effect of catalyst synthesis parameters on the metal particle size. *Applied Catalysis A: General*, 451:251-281.

Markiewicz, M., Zhang, Y., Bösmann, A., Brückner, N., Thöming, J., Wasserscheid, P. & Stolte, S. 2015. Environmental and health impact assessment of Liquid Organic Hydrogen Carrier (LOHC) systems–challenges and preliminary results. *Energy & Environmental Science*, 8(3):1035-1045.

Matsagar, B.M., Sung, H.-L., Yeh, J.-Y., Chen, C.-T. & Wu, K.C.-W. 2021. One-step hydrogenolysis of 5-hydroxymethylfurfural to 1, 2, 6-hexanetriol using a Pt@ MIL-53-derived Pt@ Al 2 O 3 catalyst and NaBH 4 in aqueous media. *Sustainable Energy & Fuels*, 5(16):4087-4094.

Mehrabadi, B.A., Eskandari, S., Khan, U., White, R.D. & Regalbuto, J.R. 2017. A review of preparation methods for supported metal catalysts. *Advances in catalysis*, 61:1-35.

Microtrac. *Microtrac Belcat II Particle Analyser* https://www.microtrac.com/files/80605/belcat-ii.pdf Date of access: 12 January 2025.

Modisha, P. & Bessarabov, D. 2020. Stress tolerance assessment of dibenzyltoluene-based liquid organic hydrogen carriers. *Sustainable Energy & Fuels*, 4(9):4662-4670.

Modisha, P. & Bessarabov, D. 2023. Aromatic liquid organic hydrogen carriers for hydrogen storage and release. *Current Opinion in Green and Sustainable Chemistry*, 42:100820.

Modisha, P., Gqogqa, P., Garidzirai, R., Ouma, C.N. & Bessarabov, D. 2019. Evaluation of catalyst activity for release of hydrogen from liquid organic hydrogen carriers. *International Journal of Hydrogen Energy*, 44(39):21926-21935.

Modisha, P.M., Jordaan, J.H., Bösmann, A., Wasserscheid, P. & Bessarabov, D. 2018. Analysis of reaction mixtures of perhydro-dibenzyltoluene using two-dimensional gas chromatography and single quadrupole gas chromatography. *International Journal of Hydrogen Energy*, 43(11):5620-5636.

Modisha, P.M., Ouma, C.N., Garidzirai, R., Wasserscheid, P. & Bessarabov, D. 2019. The prospect of hydrogen storage using liquid organic hydrogen carriers. *Energy & Fuels*, 33(4):2778-2796.

Moradi, R. & Groth, K.M. 2019. Hydrogen storage and delivery: Review of the state of the art technologies and risk and reliability analysis. *International Journal of Hydrogen Energy*, 44(23):12254-12269.

Mostafa, M.S., El Naga, A.O.A., Galhoum, A.A., Guibal, E. & Morshedy, A.S. 2019. A new route for the synthesis of self-acidified and granulated mesoporous alumina catalyst with superior Lewis acidity and its application in cumene conversion. *Journal of Materials Science*, 54:5424-5444.

Müller, K. 2019. Technologies for the Storage of Hydrogen Part 1: Hydrogen Storage in the Narrower Sense. *ChemBioEng Reviews*, 6(3):72-80.

Müller, K., Aslam, R., Fischer, A., Stark, K., Wasserscheid, P. & Arlt, W. 2016. Experimental assessment of the degree of hydrogen loading for the dibenzyl toluene based LOHC system. *International Journal of Hydrogen Energy*, 41(47):22097-22103.

Müller, K., Thiele, S. & Wasserscheid, P. 2019. Evaluations of concepts for the integration of fuel cells in liquid organic hydrogen carrier systems. *Energy & Fuels*, 33(10):10324-10330.

Müller, K., Stark, K., Emel'yanenko, V.N., Varfolomeev, M.A., Zaitsau, D.H., Shoifet, E., ... Arlt, W. 2015. Liquid organic hydrogen carriers: thermophysical and thermochemical studies of benzyl-and dibenzyl-toluene derivatives. *Industrial & Engineering Chemistry Research*, 54(32):7967-7976.

Munnik, P., De Jongh, P.E. & De Jong, K.P. 2015. Recent developments in the synthesis of supported catalysts. *Chemical reviews*, 115(14):6687-6718.

Niermann, M., Beckendorff, A., Kaltschmitt, M. & Bonhoff, K. 2019. Liquid Organic Hydrogen Carrier (LOHC)–Assessment based on chemical and economic properties. *International Journal of Hydrogen Energy*, 44(13):6631-6654.

Ninomiya, W., Tanabe, Y., Uehara, Y., Sotowa, K.-I. & Sugiyama, S. 2006. Dehydrogenation of tetralin on Pd/C and Te-Pd/C catalysts in the liquid-film state under distillation conditions. *Catalysis letters*, 110:191-194.

Oh, J., Bathula, H.B., Park, J.H. & Suh, Y.-W. 2019. A sustainable mesoporous palladium-alumina catalyst for efficient hydrogen release from N-heterocyclic liquid organic hydrogen carriers. *Communications chemistry*, 2(1):68.

Peng, Y., Yuan, X., Si, W., Zhu, X. & Zhou, B. 2024. Anchoring mechanism of low-coordination terminal hydroxyls in Pt atomic clusters.

Peters, W., Seidel, A., Herzog, S., Bösmann, A., Schwieger, W. & Wasserscheid, P. 2015. Macrokinetic effects in perhydro-N-ethylcarbazole dehydrogenation and H 2 productivity optimization by using egg-shell catalysts. *Energy & environmental science*, 8(10):3013-3021.

Preuster, P., Papp, C. & Wasserscheid, P. 2017. Liquid organic hydrogen carriers (LOHCs): toward a hydrogen-free hydrogen economy. *Accounts of Chemical Research*, 50(1):74-85.

Preuster, P., Alekseev, A. & Wasserscheid, P. 2017. Hydrogen storage technologies for future energy systems. *Annual Review of Chemical and Biomolecular Engineering*, 8(1):445-471.

Preuster, P., Fang, Q., Peters, R., Deja, R., Blum, L., Stolten, D. & Wasserscheid, P. 2018. Solid oxide fuel cell operating on liquid organic hydrogen carrier-based hydrogen–making full use of heat integration potentials. *International Journal of Hydrogen Energy*, 43(3):1758-1768.

Rao, P.C. & Yoon, M. 2020. Potential liquid-organic hydrogen carrier (LOHC) systems: A review on recent progress. *Energies*, 13(22):6040.

Rao, V., Latha, P., Ashokan, P. & Shridhar, M. 1999. Thermal degradation of poly (N-vinylpyrrolidone)–poly (vinyl alcohol) blends. *Polymer Journal*, 31(10):887-889.

Reddy, V.J., Hariram, N., Maity, R., Ghazali, M.F. & Kumarasamy, S. 2023. Sustainable E-Fuels: Green Hydrogen, Methanol and Ammonia for Carbon-Neutral Transportation. *World Electric Vehicle Journal*, 14(12):349.

Rivard, E., Trudeau, M. & Zaghib, K. 2019. Hydrogen storage for mobility: A review. *Materials*, 12(12):1973.

Romero, D., Oropeza, F., Rigutto, M. & Hensen, E.J. 2022. Influence of polyvinylpyrrolidone as stabilizing agent on Pt nanoparticles in Pt/H-BEA catalyzed hydroconversion of n-hexadecane. *Fuel*, 317:123506.

Roy, A. & Pramanik, S. 2024. A review of the hydrogen fuel path to emission reduction in the surface transport industry. *International Journal of Hydrogen Energy*, 49:792-821.

Rüde, T., Dürr, S., Preuster, P., Wolf, M. & Wasserscheid, P. 2022. Benzyltoluene/perhydro benzyltoluene–pushing the performance limits of pure hydrocarbon liquid organic hydrogen carrier (LOHC) systems. *Sustainable Energy & Fuels*, 6(6):1541-1553.

Sabharwal, M. & Secanell, M. 2022. Understanding the effect of porosity and pore size distribution on low loading catalyst layers. *Electrochimica Acta*, 419:140410.

Sage, V., Patel, J., Hazewinkel, P., Yasin, Q.U.A., Wang, F., Yang, Y., ... Li, C.E. 2024. Recent progress and techno-economic analysis of liquid organic hydrogen carriers for Australian renewable energy export–A critical review. *International Journal of Hydrogen Energy*, 56:1419-1434.

Sakintuna, B., Lamari-Darkrim, F. & Hirscher, M. 2007. Metal hydride materials for solid hydrogen storage: a review. *International Journal of Hydrogen Energy*, 32(9):1121-1140.

Schildhauer, T., Newson, E. & Müller, S. 2001. The equilibrium constant for the methylcyclohexane–toluene system. *Journal of Catalysis*, 198(2):355-358.

Schlapbach, L. & Züttel, A. 2001. Hydrogen-storage materials for mobile applications. *nature*, 414(6861):353-358.

Schörner, M., Solymosi, T., Razcka, T., Nathrath, P., Johner, N.P., Zimmermann, T., ... Schühle, P. 2024. Inductively heatable catalytic materials for the dehydrogenation of the liquid organic hydrogen carrier (LOHC) perhydro dibenzyltoluene. *Catalysis Science & Technology*, 14(16):4450-4457.

Shah, M. 2012. Growth of uniform nanoparticles of platinum by an economical approach at relatively low temperature. *Scientia Iranica*, 19(3):964-966.

Shi, L., Zhou, Y., Qi, S., Smith, K.J., Tan, X., Yan, J. & Yi, C. 2020. Pt catalysts supported on H2 and O2 plasma-treated Al2O3 for hydrogenation and dehydrogenation of the liquid organic hydrogen carrier pair dibenzyltoluene and perhydrodibenzyltoluene. *ACS Catalysis*, 10(18):10661-10671.

Shuang, H., Chen, H., Wu, F., Li, J., Cheng, C., Li, H. & Fu, J. 2020. Catalytic dehydrogenation of hydrogen-rich liquid organic hydrogen carriers by palladium oxide supported on activated carbon. *Fuel*, 275:117896.

Shukla, A.A., Gosavi, P.V., Pande, J.V., Kumar, V.P., Chary, K.V. & Biniwale, R.B. 2010. Efficient hydrogen supply through catalytic dehydrogenation of methylcyclohexane over Pt/metal oxide catalysts. *International Journal of Hydrogen Energy*, 35(9):4020-4026.

Sievi, G., Geburtig, D., Skeledzic, T., Bösmann, A., Preuster, P., Brummel, O., ... Katsounaros, I. 2019. Towards an efficient liquid organic hydrogen carrier fuel cell concept. *Energy & Environmental Science*, 12(7):2305-2314.

Sinfelt, J.H. 1977. Heterogeneous Catalysis: Some Recent Developments: Some properties of metal catalysts and recent advances in alloys and bimetallic systems are discussed. *Science*, 195(4279):641-646.

Sinfelt, J.H. 2000. The turnover frequency of methylcyclohexane dehydrogenation to toluene on a Pt reforming catalyst. *Journal of Molecular Catalysis A: Chemical*, 163(1-2):123-128.

Solymosi, T., Auer, F., Dürr, S., Preuster, P. & Wasserscheid, P. 2021. Catalytically activated stainless steel plates for the dehydrogenation of perhydro dibenzyltoluene. *International Journal of Hydrogen Energy*, 46(70):34797-34806.

Sotoodeh, F., Huber, B.J. & Smith, K.J. 2012. Dehydrogenation kinetics and catalysis of organic heteroaromatics for hydrogen storage. *International Journal of Hydrogen Energy*, 37(3):2715-2722.

Southall, E. & Lukashuk, L. 2022. Potential Deployment and Integration of Liquid Organic Hydrogen Carrier Technology within Different Industries: Liquid organic hydrogen carrier technology to support on demand hydrogen supply and energy storage. *Johnson Matthey Technology Review*, 66(3):259-270.

Srinivasan, S.S. & Demirocak, D.E. 2017. Metal hydrides used for hydrogen storage. *Nanostructured Materials for Next-Generation Energy Storage and Conversion: Hydrogen Production, Storage, and Utilization*:225-255.

Staffell, I., Scamman, D., Abad, A.V., Balcombe, P., Dodds, P.E., Ekins, P., ... Ward, K.R. 2019. The role of hydrogen and fuel cells in the global energy system. *Energy & Environmental Science*, 12(2):463-491.

Tabib Zadeh Adibi, P., Pingel, T., Olsson, E., Gronbeck, H. & Langhammer, C. 2016. Pt nanoparticle sintering and redispersion on a heterogeneous nanostructured support. *The Journal of Physical Chemistry C*, 120(27):14918-14925.

Tarleton, E.S. 2014. *Progress in Filtration and Separation*. Academic Press.

Tashie-Lewis, B.C. & Nnabuife, S.G. 2021. Hydrogen production, distribution, storage and power conversion in a hydrogen economy-a technology review. *Chemical Engineering Journal Advances*, 8:100172.

Technologies, V.I. *Induction Heating Equipment* https://www.velinnovative.com/induction-heating-equipment/ Date of access: 02/02/2025.

Teichmann, D., Arlt, W. & Wasserscheid, P. 2012. Liquid Organic Hydrogen Carriers as an efficient

vector for the transport and storage of renewable energy. *International Journal of Hydrogen Energy*, 37(23):18118-18132.

Teichmann, D., Stark, K., Müller, K., Zöttl, G., Wasserscheid, P. & Arlt, W. 2012. Energy storage in residential and commercial buildings via Liquid Organic Hydrogen Carriers (LOHC). *Energy & Environmental Science*, 5(10):9044-9054.

Union, E. 2021. *Catalyst development for improved economic viability of LOHC technology*. https://cordis.europa.eu/programme/id/H2020_FCH-02-1-2020 Date of access: 1 April

Usman, M.R. 2022. Hydrogen storage methods: Review and current status. *Renewable and Sustainable Energy Reviews*, 167:112743.

Volynkin, A., Rønning, M. & Blekkan, E.A. 2015. The role of carbon support for propane dehydrogenation over platinum catalysts. *Topics in Catalysis*, 58:854-865.

Von Wild, J., Friedrich, T., Cooper, A., Toseland, B., Muraro, G., TeGrotenhuis, W., ... Karim, A. 2010. Liquid Organic Hydrogen Carriers (LOHC): An auspicious alternative to conventional hydrogen storage technologies. In. 18th World Hydrogen Energy Conference, Essen, Germany.

Wang, W., Tuci, G., Duong-Viet, C., Liu, Y., Rossin, A., Luconi, L., ... Giambastiani, G. 2019. Induction heating: An enabling technology for the heat management in catalytic processes. *ACS Catalysis*, 9(9):7921-7935.

Wu, L., Li, Y., Fu, Z. & Su, B.-L. 2020. Hierarchically structured porous materials: Synthesis strategies and applications in energy storage. *National Science Review*, 7(11):1667-1701.

Wu, Y., Li, Y., Yu, X., Ma, X., Boebinger, M., Weber, J. & Wu, Z. 2024. Insights into size effects of Pt/Al 2 O 3 catalysts on hydrogen production from methylcyclohexane dehydrogenation. *Catalysis Science & Technology*, 14(7):1791-1801.

Wunsch, A., Mohr, M. & Pfeifer, P. 2018. Intensified LOHC-dehydrogenation using multi-stage microstructures and Pd-based membranes. *Membranes*, 8(4):112.

Xie, T., Hare, B.J., Meza-Morales, P.J., Sievers, C. & Getman, R.B. 2020. Identification of the active sites in the dehydrogenation of methanol on Pt/Al2O3 catalysts. *The Journal of Physical Chemistry C*, 124(35):19015-19023.

Yan, J., Wang, W., Miao, L., Wu, K., Chen, G., Huang, Y. & Yang, Y. 2018. Dehydrogenation of methylcyclohexane over PtSn supported on MgAl mixed metal oxides derived from layered double hydroxides. *International Journal of Hydrogen Energy*, 43(19):9343-9352.

Yang, W., Zhu, Y., Li, J., Chen, Z., Nosheen, F., Zhang, Q. & Zhang, Z. 2021. Understanding the dehydrogenation mechanism over iron nanoparticles catalysts based on density functional theory. *Chinese Chemical Letters*, 32(1):286-290.

Zahra, F.T., Zhang, Y., Ajayi, A.O., Quick, Q. & Mu, R. 2024. Optimization of electrospinning parameters for lower molecular weight polymers: A case study on polyvinylpyrrolidone. *Polymers*, 16(9):1217.

Zhang, F., Zhao, P., Niu, M. & Maddy, J. 2016. The survey of key technologies in hydrogen energy storage. *International Journal of Hydrogen Energy*, 41(33):14535-14552.

Zhang, Z., Hicks, R.W., Pauly, T.R. & Pinnavaia, T.J. 2002. Mesostructured forms of γ-Al2O3. *Journal of the American Chemical Society*, 124(8):1592-1593.

Zhao, S., Zhang, J., Weng, D. & Wu, X. 2003. A method to form well-adhered γ-Al2O3 layers on FeCrAl metallic supports. *Surface and Coatings Technology*, 167(1):97-105.

Zhu, Q.-L. & Xu, Q. 2015. Liquid organic and inorganic chemical hydrides for high-capacity hydrogen storage. *Energy & Environmental Science*, 8(2):478-512.

Zou, J., Fan, C., Jiang, Y., Liu, X., Zhou, W., Xu, H. & Huang, L. 2021. A preliminary study on assessing the Brunauer-Emmett-Teller analysis for disordered carbonaceous materials. *Microporous and Mesoporous Materials*, 327:111411.

Züttel, A. 2003. Materials for hydrogen storage. *Materials today*, 6(9):24-33.

Züttel, A. 2004. Hydrogen storage methods. *Naturwissenschaften*, 91:157-172.